INFORMATION TO USERS

This manuscript has been reproduced from the microfilm master. UMI films the text directly from the original or copy submitted. Thus, some thesis and dissertation copies are in typewriter face, while others may be from any type of computer printer.

The quality of this reproduction is dependent upon the quality of the copy submitted. Broken or indistinct print, colored or poor quality illustrations and photographs, print bleedthrough, substandard margins, and improper alignment can adversely affect reproduction.

In the unlikely event that the author did not send UMI a complete manuscript and there are missing pages, these will be noted. Also, if unauthorized copyright material had to be removed, a note will indicate the deletion.

Oversize materials (e.g., maps, drawings, charts) are reproduced by sectioning the original, beginning at the upper left-hand corner and continuing from left to right in equal sections with small overlaps.

Photographs included in the original manuscript have been reproduced xerographically in this copy. Higher quality 6" x 9" black and white photographic prints are available for any photographs or illustrations appearing in this copy for an additional charge. Contact UMI directly to order.

Bell & Howell Information and Learning
300 North Zeeb Road, Ann Arbor, MI 48106-1346 USA
800-521-0600

UMI®

Structural-optical relationships in first-year sea ice

Bonnie Light

A dissertation submitted in partial fulfillment of the
requirements for the degree of

Doctor of Philosophy

University of Washington

2000

Program Authorized to Offer Degree: Department of Atmospheric Sciences

In presenting this dissertation in partial fulfillment of the requirements for the Doctoral degree at the University of Washington, I agree that the Library shall make its copies freely available for inspection. I further agree that extensive copying of the dissertation is allowable only for scholarly purposes, consistent with "fair use" as prescribed in the U.S. Copyright Law. Requests for copying or reproduction of this dissertation may be referred to Bell and Howell Information and Learning, 300 North Zeeb Road, Ann Arbor, MI 48106-1346, to whom the author has granted "the right to reproduce and sell (a) copies of the manuscript in microform and/or (b) printed copies of the manuscript made from microform."

Signature Bonnie Knight

Date 2 June 2006

University of Washington
Graduate School

This is to certify that I have examined this copy of a doctoral dissertation by

Bonnie Light

and have found that it is complete and satisfactory in all respects,
and that any and all revisions required by the final
examining committee have been made.

Chair of Supervisory Committee:

Gary A. Maykut
Gary A. Maykut

Reading Committee:

Gary A. Maykut
Gary A. Maykut

Thomas C. Grenfell
Thomas C. Grenfell

Stephen G. Warren
Stephen G. Warren

Date: 23 May 2000

University of Washington

Abstract

Structural-optical relationships in first-year sea ice

Bonnie Light

Chairperson of the Supervisory Committee:
Professor Gary A. Maykut
Department of Atmospheric Sciences

The optical properties of sea ice are governed by the distribution of brine and gas inclusions, and precipitated salt crystals within the ice. Laboratory experiments designed to understand structural-optical relationships and their dependence on temperature in first-year sea ice were carried out. Detailed observations of the microstructure of isothermal samples of natural sea ice were obtained for temperatures between –33 and –2 °C. Changes in apparent optical properties of cylindrical samples cut from the same ice core were monitored simultaneously. A cylindrical Monte Carlo radiative transfer model was developed to infer inherent optical properties from the radiance data. Experimental results were used to develop and test a structural-optical model necessary for detailed radiative transfer modeling in sea ice.

Microstructure observations were initially carried out at –15 °C to obtain inclusion size distributions. Brine pocket dimensions were found to range from 0.01 mm to 10 mm, with number densities averaging about 30 mm^{-3}. Observed vapor bubbles had radii less than 0.2 mm and number densities approximately 1 mm^{-3}. Both these estimates are an order of magnitude larger than number densities previously reported.

Results indicate that structural-optical relationships in sea ice can be described by three regimes. At temperatures below –23 °C, optical properties change dramatically, and are most affected by the precipitation of hydrohalite. At temperatures between –23 and –8 °C, they remain fairly constant where effects from changes in the mass of precipitated mirabilite crystals are offset by changes in the size of brine inclusions. At temperatures between –8 and –2 °C, only small changes in the optical properties of the ice were observed, despite large observed increases in the cross-sectional area of the

inclusions. This was discovered to be related to a significant increase in bulk asymmetry parameter resulting from a decrease in the refractive index of brine. We expect this general pattern will be found in most types of sea ice, regardless of the exact distribution of inclusions. These results suggest that it is possible to develop simple parameterizations of radiative transfer in sea ice appropriate for incorporation into large-scale climate models and GCMs.

TABLE OF CONTENTS

List of Figures iv

List of Tables vi

Chapter One: Introduction 1

Chapter Two: Background 4
Sea Ice Microstructure 5
Brine Inclusions 7
Gas Inclusions 9
Precipitated Salts 10
Optical Modeling 11
Radiative Transfer Modeling in Sea Ice 11
Inherent Optical Properties 12
Absorption 13
Scattering 14
Structural-Optical Treatment 17

Chapter Three: Experimental Approach 21
Ice Samples 22
Laboratory Setup 23
Structural Measurements 23
Optical Measurements 25

Chapter Four: Microstructure of First-Year Sea Ice 26
Sample Preparation 26
Laboratory Setup 27
Observations at –15 °C 28
Brine Inclusions 31
Vapor Bubbles 38
Mirabilite Crystals 39
Temperature-Dependent Changes 40
Cooling Sequence 42
Warming Sequence 44
Modeling Inclusion Enlargement and Merging 50
Summary 52

Chapter Five: Modeling Radiative Transfer in a Cylindrical Domain 55
Approach 55
Solution of the Adjoint Problem 57
Implementation 61
Photon Release 62

Distance Between Collisions 63
Photon Interactions 64
Photon Counting 65
Refractive Domain 68
Convergence Criterion 69
Tests of the Model 70
Radiance Detector 70
Optical Depth and Asymmetry Parameter 71
Refractive Domain 72
Non-conservative Scattering 77
Horizontally Finite Domain 81
Similarity Parameter 83
Summary 86

Chapter Six: Laboratory Observations of Sea Ice Optical Properties 89
Experiment Design 89
Sample Size 91
Radiance Probes 92
Calibrations 95
Glass Plate Absorption 95
Alignment of Incident Light Source 96
Radiance Probes 96
Optical Properties of First-Year Ice at –15 °C 98
Temperature-Dependent Results 103
Discussion 108

Chapter Seven: Structural-Optical Model 112
Absorption Coefficient 112
Scattering Coefficient 113
Brine Inclusions 114
Ellipsoids 114
Cylindrical Tubes 115
Vapor Bubbles 116
Precipitated Salt Crystals 116
Initialization at –15 °C 116
Temperature-Dependent Scattering 118
Refinement of Scattering for Salt Regimes 120
Hydrohalite Regime 120
Mirabilite Regime 122
Refinement of Scattering For Warm Regime 122
Anisotropy of Congelation Ice 123
Temperature-Dependent Asymmetry Parameter 126
Merging Brine Pockets 127
Discussion 128

Chapter Eight: Sensitivity Studies and Conclusions 132
First-Year Interior Ice 132
Brine Inclusions 133
Precipitated Salt Crystals 134
Additional Scatterers 135
Asymmetry Parameter 138
High Salinity Ice 139
Field Data 143
Conclusions 144

List of References 147

LIST OF FIGURES

Figure		Page
2.1	Schematic of skeletal layer at ice-ocean interface	6
2.2	Fractional volumes of brine, gas, and precipitated salt in sea ice	8
2.3	Spectral absorption coefficients for pure ice and clear Arctic water	14
2.4	Albedo and transmissivity for a laboratory-grown sea ice sample	19
4.1	Schematic of imaging system for observing ice microstructure	28
4.2	Photograph of vertical thick section of first-year sea ice	29
4.3	Photomosaic of vertical thin section of first-year sea ice	30
4.4	Ten subregions from the mosaic	33
4.5	Examples of small brine pockets	35
4.6	Examples of vapor bubbles within brine pockets	40
4.7	Examples of precipitated mirabilite crystals within brine tubes	41
4.8	Ice microstructure cooling sequence	43
4.9	Ice microstructure warming sequence	45
4.10	First-year congelation microstructure as it warms to near melting	47
4.11	Ice microstructure as it warms and subsequently cools	49
5.1	Schematic of forward and adjoint radiative transfer problems	58
5.2	Radiance distribution for a horizontally-infinite slab	72
5.3	Albedo and transmissivity as functions of optical depth and asymmetry parameter for a refractive slab with conservative scattering	73
5.4	Albedo and transmissivity as functions of optical depth for large asymmetry parameters in a non-refractive slab with conservative scattering	75
5.5	Albedo and transmissivity as functions of optical depth and asymmetry parameter for a refractive slab with conservative scattering	78
5.6	Comparison of modeled spectral albedos and transmissivities for a refractive slab with non-conservative scattering	80
5.7	Energy loss at top, bottom, and side surfaces of a non-refractive cylinder as a function of scattering coefficient	82
5.8	Energy loss at top, bottom, and side surfaces of a refractive cylinder as a function of cylinder radius	84
5.9	Inverse of the similarity parameter as a function of scattering coefficient and asymmetry parameter	85
5.10	Albedo, transmissivity, and side irradiance as a function of cylinder radius and asymmetry parameter for a refractive cylinder	87
6.1	Schematic of the optical experiment in the laboratory coldroom	90
6.2	Predicted diffuse fields and energy losses as a function of sample thickness for an ice cylinder	93
6.3	Schematic of the lens holder on the moveable fiber optic probe	95
6.4	Observed spectral radiances for a laboratory sample at −15 C	99
6.5	Modeled radiances as a function of similarity parameter for a laboratory sample	101
6.6	Comparison of observed and modeled radiances at −15 C	102
6.7	Observed spectral transmitted radiance at a selection of temperatures	104

6.8 Observed radiances at 500 nm as a function of sample temperature..... 105
6.9 Inferred similarity parameters and scattering coefficients for all observed radiances..... 106
6.10 Final inferred similarity parameter and scattering coefficient as a function of temperature..... 109
7.1 Preliminary temperature-dependent scattering coefficients for sea ice..... 119
7.2 Comparison of inferred similarity parameter and preliminary model..... 121
7.3 Comparison of inferred similarity parameter and refined model..... 123
7.4 Similarity parameters for processes affecting scattering in warm sea ice..... 131
8.1 Albedo and transmissivity as a function of precipitated salt crystal size..... 136
8.2 Comparison of observed and modeled inherent optical properties for two laboratory samples..... 140
8.3 Temperature-dependent scattering coefficient for two sea ice samples..... 142

LIST OF TABLES

Number		Page
4.1	Brine inclusion size distribution in first-year sea ice samples	36
4.2	Vapor bubble size distribution in first-year sea ice samples	39
5.1	Values of source function required to model various detectors	59
5.2	Inherent optical properties representative of transition sea ice	77
6.1	Spectral absorption coefficient for glass plate	96
7.1	Scattering properties of observed brine inclusions	114
7.2	Scattering properties of observed vapor bubbles	116
7.3	Total scattering coefficients for model initialization	118
7.4	Temperature-dependent bulk asymmetry parameter for warm ice	127
7.5	Merging factors for brine pockets	128
8.1	Inherent optical properties of first-year interior sea ice	133

ACKNOWLEDGEMENTS

I thank my advisors Dr. Gary Maykut and Dr. Thomas Grenfell for their support and guidance during the course of this work. Their inquiry and insight expanded my thinking and enhanced my understanding. Dr. Maykut's interests in the physics of sea ice permeate this work. He gave freely of his time advising me in the preparation of this manuscript, for which I am very grateful. Dr. Grenfell's knowledge of radiative transfer and commitment to quality laboratory and field investigation were invaluable.

I am also grateful to the other members of my committee for their time and guidance. Dr. Stephen Warren provided indispensable course work in radiative transfer and the physics of snow and ice. Dr. Norbert Untersteiner was a perennial source of encouragement in this endeavor. I thank Dr. Seelye Martin and Dr. R. Hamish Robertson for their service.

I thank Dr. Tony Gow and Dr. Donald Perovich of the Cold Regions Research and Engineering Laboratory for use of their microtome. Steven Domonkos provided much instruction, resourcefulness, and patience in the machine shop.

The members of my family provided enduring support and I thank my husband, Matthew Wyant, for his patience, motivation, keen scientific perspective, and tireless editorial support.

This work was made possible by support from the Office of Naval Research, Arctic Program under Grants N00014-90-J-1075, N00014-94-1-0791, and N00014-97-1-0765.

CHAPTER ONE
INTRODUCTION

Sea ice is generally believed to be a key element in the earth's climate system. Large-scale model simulations indicate that it is not only sensitive to climate change, but that it contributes to such change (Ingram et al., 1989; Manabe et al., 1991; Rind et al., 1995). Sea ice acts as a barrier to the transfer of heat, moisture, and momentum between the polar oceans and the atmosphere. By area, sea ice accounts for nearly two thirds of the Earth's permanent ice cover, but accounts for only about 0.1% of its total volume. Because the ice cover is thin, small changes in the heat balance of the ice pack can result in large and rapid changes in thickness and areal extent. This is particularly true in summer when the ice cover evolves from a highly backscattering, snow-covered surface to a darker surface composed of bare ice, melt ponds, and leads. Changes in the thickness, melt pond coverage, and areal extent of sea ice affect not only the total input of solar energy to the polar regions, but also heating in the upper ocean, biological productivity in both ocean and ice, net radiative fluxes at the surface, and heat and moisture transport into the atmospheric boundary layer. In addition, there is a positive feedback between solar radiation, ice extent, and climate. An increase in ice extent would increase the amount of reflected solar radiation producing a net cooling of the climate. Such a cooling would likely cause a further increase in sea ice extent and further cooling. This so-called ice-albedo feedback process has become an important topic of current experimental and theoretical research (e.g., Ebert and Curry, 1993; Moritz and Perovich, 1996; Holland et al., 1997), but details of the numerous physical processes involved in this feedback and their interactions with the ice, ocean, and atmosphere are not yet completely understood.

Interactions between sea ice and solar radiation are particularly important in this feedback process. When incoming solar radiation is large, energy absorption by ice and water promote rapid changes in the state of the ice cover. These include the melting and removal of snow from the ice surface, surface ice ablation, the formation of melt ponds and leads, and changes in the physical structure of the upper part of the ice. Snow-free ice and ponded ice backscatter much less solar radiation than snow-covered

ice, leaving more energy to be absorbed and transmitted to the upper ocean. Changes in the physical structure of the ice also can have a direct impact on how solar radiation is backscattered, transmitted and absorbed.

Sea ice is composed of numerous inclusions of brine, air, precipitated salt crystals, and impurities embedded within a matrix of pure ice. This structure is complex and the effect the different inclusions have on the optical properties of the ice has not yet been fully quantified. It is known, however, that temperature changes in the ice can produce large changes in the size, number, and distributions of these inclusions which presumably alter the optical properties of the ice.

Numerous observations have been made of ice optical properties as a function of ice type and season. Langleben (1969, 1971) documented changes in total albedos of a melting, first-year sea ice cover. Grenfell and Maykut (1977) reported spectral albedos for melting white ice, blue ice, and meltponds on first-year and multiyear ice. Much work has focused on monitoring the albedos of sea ice as it makes the transition from being snow-covered to bare to melting to ponded (e.g. Grenfell and Perovich, 1984; Perovich, 1994). Substantial data have also been collected on changes in transmissivity and in-ice radiance as the ice begins to melt (e.g., Untersteiner, 1961; Chernigovskiy, 1963; Maykut and Grenfell, 1975; Grenfell and Maykut, 1977; Perovich et al., 1998b).

Modeling studies have been applied to many of these observations using standard radiative transfer methods. These models range in complexity from a simple exponential decay model (Maykut and Untersteiner, 1971), multistream and multilayer treatments (Grenfell and Maykut, 1977; Grenfell, 1983, 1991; Perovich, 1990) to a multistream treatment of radiative transfer in the ocean-ice-air column (Jin et al., 1994). These models not only require information about the incident radiation, but also about the geometry, boundary conditions, and inherent optical properties of the ice. The magnitudes and vertical variation of these optical properties, however, are determined strictly by the ice microstructure. Although we know some of the ways that absorption and scattering in sea ice depend on this microstructure, a full quantitative understanding of structural-optical relationships has yet to emerge.

The objective of this dissertation is to further our quantitative understanding of relationships between the structural and optical properties of sea ice. The work is based on direct laboratory observations of the structural-optical properties of sea ice. By obtaining simultaneous data on the response of both the ice microstructure and its optical properties to changes in temperature, we lay the groundwork for understanding how these properties are related. These relationships are defined and explored through the development of a structural-optical model for sea ice and a radiative transfer model designed specifically for computing the albedo and transmissivity of core samples.

A better understanding of the relationship between the microstructure of the ice and its inherent optical properties is critical for conducting theoretical and experimental studies of radiative transfer in sea ice. Such information is also necessary for the development of improved predictive capabilities that will hopefully lead to a more exact treatment of the heat and mass exchange within the ice-ocean-atmosphere system.

CHAPTER TWO
BACKGROUND

The optical properties of sea ice are highly variable both spatially and temporally. Since areas less than a square kilometer typically include ice types with varying ages and thicknesses, considerable horizontal variability exists in the optical properties of natural pack ice. Thick multiyear white ice has a relatively high albedo and small transmissivity, whereas ponded ice may backscatter much less light and transmit significant amounts of energy to the ocean. Variations in ice thickness, age, and growing conditions promote vertical gradients in salinity and temperature, which in turn cause vertical gradients in optical properties of the ice. Well drained ice above freeboard is typically highly scattering, whereas interior ice generally has lower gas volume and less scattering. Seasonal changes cause substantial temporal changes in the optical properties of sea ice as well. The onset of the melt season produces dramatic changes in the optical properties when the snow melts and the highly reflective surface gives way to areas of bare melting ice, ponded ice, and a substantially thinner summer ice pack.

Field investigators (e.g., Assur, 1958; Grenfell and Maykut, 1977; Lohanick and Grenfell, 1986) have made reference to a variety of visual appearances, noting that cold, growing ice often appears bright white, while melting first-year ice may appear blue, and refreezing ice at the end of the summer melt season again appears white. Bare ice albedos at 500 nm ($\alpha_{500\ nm}$) are observed to span a considerable range. For ponded ice, $\alpha_{500\ nm}$ is as low as 0.15, melting first-year blue ice has $\alpha_{500\ nm}$ about 0.45, and $\alpha_{500\ nm}$ is as high as 0.82 for cold white ice (Grenfell and Maykut, 1977). Corresponding extinction coefficients at 500 nm in interior ice range from 1.2 m^{-1} for multi-year white ice to 0.6 m^{-1} for ice beneath an old melt pond.

The spectral albedo (α_λ), transmissivity (t_λ), and extinction coefficient (K_λ) are called apparent optical properties because they depend on the properties of the incident radiation field, the boundary conditions of the domain (e.g. ice thickness), and the

inherent optical properties of the ice, specifically absorption and scattering. Apparent optical properties are particularly sensitive to the amount of scattering and absorption which are directly related to the internal structure of the ice (Grenfell and Maykut 1977; Perovich and Grenfell, 1982; Light, 1995).

Sea ice is a complex composite of ice, brine, precipitated salts, gas, and biogenic and lithogenic particulate inclusions. Scattering within the ice is controlled primarily by these internal inhomogeneities, all of which are known to exhibit significant variability in space and time. There is no simple correlation between the inherent optical properties and bulk physical properties of the ice because the inherent properties depend not only on the total volume of brine and vapor in the ice, but also on how the individual inclusions of brine and vapor are distributed. Details of the relationship between the optical and physical properties of sea ice are known to be important, but have not been well established. In this chapter, we review what is known about the structural and optical properties of sea ice.

2.1 Sea Ice Microstructure

The initial formation of a sea ice cover is characterized by the compaction of randomly oriented frazil crystals into a granular ice structure. After this initial formation, further growth occurs by accretion on the underside of the ice, the rate depending on how rapidly heat can be conducted from the ice-water interface toward the surface. This ice, known as congelation ice, has fairly uniform crystal structure. The crystals are generally large in size, with lengths greater than 5 cm, and their c-axes are horizontally oriented. Because of the difference in diffusion rates of salt and heat in the water near the growth interface, ice platelets typically grow downward from the interface into the seawater forming a so-called "skeletal layer" (see Fig. 2.1). Within a single crystal, these platelets are generally parallel and have typical spacings of 0.4 mm near the top of the ice sheet, increasing to 1.0 mm near the bottom of thick first-year ice (Weeks and Hamilton, 1962; Nakawo and Sinha, 1984), as their spacing depends on the

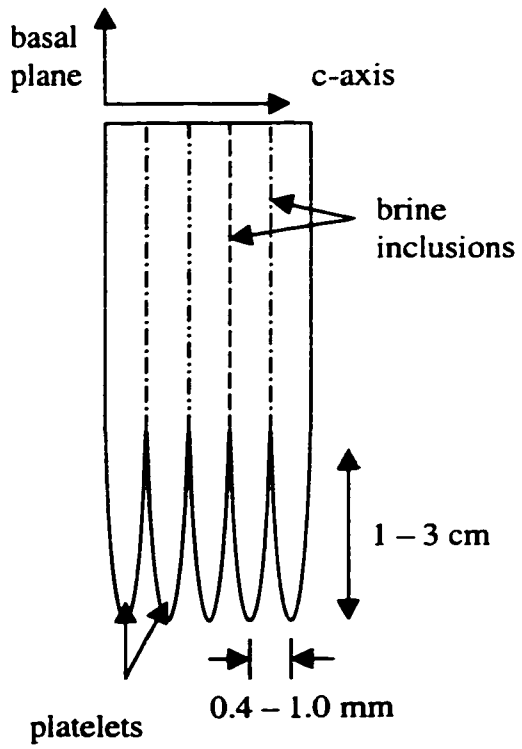

Figure 2.1 Schematic of skeletal layer at ice–ocean interface.

growth rate of the ice (Lofgren and Weeks, 1969). As the platelets lengthen, they grow wider and periodically small ice bridges form between adjacent platelets, trapping pockets of brine. This mechanism, which does not occur in fresh ice, is the source of most of the liquid inclusions found in sea ice.

Initially, the salinity of the liquid brine trapped in the ice is close to that of the seawater from which the ice formed (32 – 35 ppt). As the ice sheet grows thicker, the interior ice becomes more insulated from the warm ocean water and brine inclusions are subjected to progressively lower temperatures, causing the brine to become more concentrated to maintain a freezing-equilibrium salinity. To maintain this equilibrium, pure water from the brine pocket freezes to the surrounding ice lattice reducing the size of the inclusion and causing the brine salinity to increase. As the brine concentrates, it becomes saturated with respect to certain salts which begin to precipitate out of

solution. When the temperature increases, ice begins to melt from the walls of the brine inclusions reducing brine salinity and causing the solid salt crystals to dissolve.

Cox and Weeks (1983) developed parameterizations of bulk changes of brine, gas, and precipitated salt volumes as a function of temperature, density, and salinity for sea ice. Figure 2.2 shows how these fractional volumes depend on temperature for ice with a salinity of 5 $^{o}/_{oo}$ (parts per thousand) and a density of 0.915 Mg m^{-3}. While knowledge of these equilibrium relationships is necessary for understanding how the physical properties of the ice respond to changes in temperature, it is also necessary to know how brine, vapor, and salt crystals are distributed within the ice if we are to understand the relationship between the structure and optical properties of the ice. In particular, we need detailed information about the size, number density, and spatial arrangement of these inclusions.

2.1.1 Brine Inclusions

Photomicrographs of sea ice thin sections clearly show numerous brine inclusions within the ice, and provide a convenient way of estimating inclusion size and number distributions. Analysis of photomicrographs of horizontal thin sections from laboratory-grown saline ice at –20 °C indicated an average brine pocket radius of approximately 80 μm (Light, 1995). Upon computing the brine volume from information about the temperature and salinity of this sample (Cox and Weeks, 1983), the effective brine pocket number density was estimated to be 1.3 per mm^3. Perovich and Gow (1996) carried out a similar analysis using natural ice. Their observations of 20 cm thick, young ice taken from a freezing lead at temperatures between –3 and –9 °C, produced inclusion number densities of 1.4 – 3.1 per mm^3 and mean inclusion radii between 100 and 140 μm. Another specimen taken from first-year, shore-fast ice near Pt. Barrow, Alaska yielded number densities of 1.0 – 4.5 per mm^3 and radii 80 – 130 μm. The smallest brine pockets observed in these studies had 25 μm radii. We believe this to be the limit of the observational resolution, not the lower limit on brine inclusion size. While observations taken from horizontal thin sections such as these are useful,

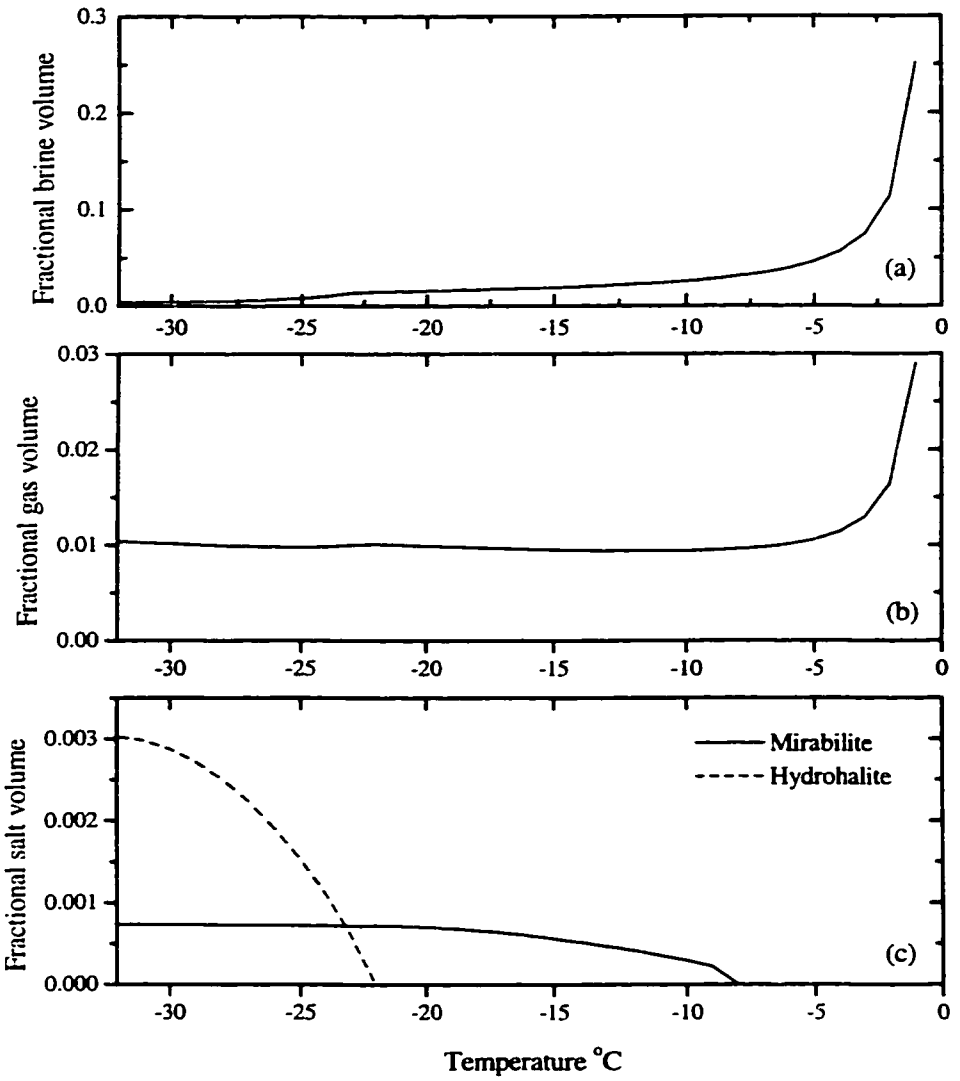

Figure 2.2 Fractional volumes of (a) brine, (b) gas, and (c) precipitated salts in sea ice with salinity 5 $^{o}/_{oo}$ and density 0.915 Mg m^{-3} as predicted by Cox and Weeks (1983).

vertical thin sections provide additional views of the ice microstructure.

In a vertical thin section, many brine inclusions are spherical, ellipsoidal, or tubular, yet most are elongated and tend to be oriented vertically (Weeks and Assur, 1967; Lake and Lewis, 1970). In this study we will refer to the numerous spherical and ellipsoidal inclusions found in the layers between platelets as brine pockets and to the larger tubular features that extend vertically within the ice as brine tubes. Brine tubes have reported concentrations in the horizontal plane of 2 - 10 per 100 cm^2 (Wakatsuchi and Saito,

1985). These tubes, or channels, correspond directly to areas of high bulk salinity in the ice (Cottier et al., 1999), and thus are likely to harbor a large fraction of the brine in sea ice. Because observations made on horizontal thin sections only provide information about the cross-sectional area of inclusions, it is difficult to tell spherical pockets from brine tubes. Observations made using horizontal thin sections are difficult to generalize in terms of the size and number distributions of brine inclusions for the purposes of modeling their optical properties.

We are also interested in how brine inclusions change with temperature, particularly as the ice warms. Because sea ice is always close to its salinity determined freezing point, the fractional brine volume (v_b) decreases as the ice cools and increases as the ice warms. When v_b rises above 5% (a temperature of about –5 °C for a salinity of 5 $^{o}/_{oo}$), sea ice is observed to undergo a distinct transition in its fluid transport properties. For brine volumes larger than 5%, brine carrying heat and nutrients can move freely through the ice, whereas for smaller v_b brine transport is largely limited to tubes and cracks (Golden et al., 1998). As the ice warms, individual brine inclusions begin to merge and coalesce and this process is critical not only for the permeability of sea ice, but also affects the optical properties as the ice begins to melt. The phase relation parameterizations of Cox and Weeks (1983) specify how v_b changes with temperature, but they do not convey information about how the number distribution of brine inclusions changes in response to inclusion enlarging and merging.

2.1.2 Gas Inclusions

The bulk density of sea ice typically ranges between 0.88 – 0.92 Mg m^{-3} (Perovich et al., 1998b). Values less than that of pure ice (0.917 Mg m^{-3}) indicate the presence of significant amounts of gas within the ice. Bubbles are entrained in sea ice at the growth interface when air dissolved in sea water comes out of solution as the water freezes. Air can also be included in the upper portions of melting sea ice due to meltwater drainage and internal melting. In addition, vapor bubbles are expected to form in brine pockets as they warm and lower density ice melts into higher density liquid. The presence of

vapor bubbles within Tyndall figures in pure ice has been documented (Nakaya, 1956) and this same phenomenon could produce vapor bubbles in saline ice.

Few data have been reported on the size and number distributions of gas bubbles in sea ice. Grenfell (1983) measured bubble size distributions in ice from a freezing lead and also compiled data from a similar study done by Gavrilo and Gaitskhoki (1970). His analysis showed that for both data sets the size distribution can be well represented by a power law. The radii of the smallest and largest bubbles observed were 0.1 and 2 mm respectively. This result is for ice from a freezing lead, which we expect to have a lot of bubbles, yet the observed number density was 0.1 per mm^3, approximately ten to fifty times smaller than the observed number density for brine inclusions in first-year ice.

2.1.3 Precipitated Salts

As brine concentrates during cooling, it becomes saturated with respect to certain salts which begin to precipitate out of solution. The precipitation of significant quantities of salt begins at –8.2 °C and continues until the ice is completely solidified, at approximately –50 °C.

The total mass of precipitated salt is a unique function of temperature and ice salinity (Nelson and Thompson, 1954; Richardson, 1976). The two most abundant salts are mirabilite ($Na_2SO_4 \cdot 10H_20$) which begins to precipitate at –8.2 °C and hydrohalite ($NaCl \cdot 2H_2O$) which begins to precipitate at –22.9 °C. These two cryohydrates form monoclinic crystals whose size can be described by the length of the *b*-axis. The only information on in situ salt crystal sizes is that inferred from optical data. By matching observed and modeled apparent optical properties for laboratory grown sea ice, Light (1995) estimated effective crystal lengths of 9 μm and 8.5 μm for the *b*-axes of mirabilite and hydrohalite, respectively.

At temperatures below –25 °C, the scattering in sea ice is completely dominated by these salts. At higher temperatures, the presence of these salts plays an important role in determining the magnitude and temperature dependence of the scattering (Weeks and

Ackley, 1982; Light, 1995). We have no direct observations of the sizes or precipitation patterns of these salt crystals. Optically, it is important whether the crystals cluster within inclusions, remain suspended in the brine, or nucleate and grow on inclusion walls.

2.2 Optical Modeling

The connection between inherent and apparent optical properties for any medium is made by solving the equation of radiative transfer. Inherent optical properties (IOPs) are those that depend upon the physical properties of the medium only, and therefore are independent of the incident light field. The spectral absorption coefficient ($\kappa[\lambda]$), scattering coefficient ($\sigma[\lambda]$), and the scattering phase function ($p[\theta]$) are IOPs. We now examine previous approaches that have been used to predict apparent optical properties (AOPs) for sea ice, and discuss how IOPs for sea ice can be estimated.

2.2.1 Radiative Transfer Modeling in Sea Ice

Radiative transfer models have been applied to a wide range of problems involving sea ice. Maykut and Untersteiner (1971) modeled the absorption of solar radiation in sea ice using a wavelength-integrated Beer's Law. Grenfell (1983, 1991) modeled backscattered, transmitted, and internal irradiances for sea ice with varying properties using 4- and 16-stream discrete ordinates radiative transfer models. In a somewhat different approach, Trodahl et al. (1987, 1989) and Mobley et al. (1998) used Monte Carlo radiative transfer models to analyze beam-spread measurements in sea ice. Bio-optical interactions have been investigated in sea ice (Arrigo et al., 1991), the transmission of visible and ultraviolet light through sea ice has been examined (Perovich 1990, 1993), and the radiative interactions between the atmosphere, ice, and ocean have been assessed by Jin et al. (1994). These models range widely in computational complexity and apply a variety of solution schemes to solve the radiative transfer equation.

We would like to use radiative transfer models to predict α_λ, t_λ, and K_λ from information about the bulk physical properties of sea ice. Getting to this point, however, is complicated by the fact that all radiative transfer models require information about $\kappa(\lambda)$, $\sigma(\lambda)$, and $p(\theta)$ specific to the ice being modeled. While the IOPs are related to the history, age, bulk salinity, density, and temperature of the ice, they depend on the actual size and number distributions of brine pockets, vapor bubbles, precipitated salts, and included particulates. Despite the fact that the optical properties of the ice depend on its physical properties, sea ice exhibits strong multiple scattering and the IOPs generally cannot easily be measured directly. An abundance of good radiative transfer models exist, all of which require IOPs, but none of which are capable of generating IOPs without a treatment to derive these IOPs directly from the structural properties of the ice. In this section, we describe how detailed information about ice microstructure may be used to formulate estimates of the absorption and scattering properties needed by radiative transfer models.

2.2.2 Inherent Optical Properties

Grenfell (1983, 1991) developed a model to explore relationships between the physical and IOPs of sea ice. In this model, the medium was treated as an ensemble of distinct types of inhomogeneities embedded in a pure ice lattice that absorbs, but does not scatter radiation. Each inclusion was assumed to remain distinct, interactions between scatterers were not considered, and individual inclusions were assumed to scatter independently such that no coherent phase relationships exist between the light that is scattered by the various inclusions. The derived absorption and scattering coefficients depend explicitly on the number and size distribution of brine inclusions and gas bubbles. Estimates of $\kappa(\lambda)$, $\sigma(\lambda)$, and $p(\theta)$ are computed and then these values are input to a 4-stream radiative transfer model. Using this model, Grenfell studied the effects of changes in microstructure on the optical properties of a one-dimensional, horizontally infinite slab with vertical layering. The basic methods of computing $\kappa(\lambda)$,

$\sigma(\lambda)$, and $p(\theta)$ developed by Grenfell (1983, 1991) will serve as a foundation for similar efforts to be carried out in the current study.

Absorption

Since sea ice is a composite of pure ice (subscript i), brine (subscript b), gas (subscript g), precipitated salt crystals (subscript s), and particulates (subscript p), the bulk absorption coefficient can be described as the volume-weighted sum of absorption coefficients for all constituents in the ice,

$$\kappa(\lambda) = \kappa_i(\lambda)\, v_i + \kappa_b(\lambda)\, v_b + \kappa_g(\lambda)\, v_g + \kappa_s(\lambda)\, v_s + \kappa_p(\lambda)\, v_p, \qquad (2.1)$$

where v represents the fractional volume for each constituent. When describing bulk media or particulate material with small optical depth, $\kappa(\lambda)$ can be determined directly from the imaginary part of the refractive index, n', and the wavelength, λ,

$$\kappa(\lambda) = 4\pi n' / \lambda. \qquad (2.2)$$

The absorption coefficient of pure ice is small at visible wavelengths, with a minimum value in the blue part of the spectrum at 470 nm (Fig. 2.3). The value of $\kappa_i(\lambda)$ increases over 3 orders of magnitude as the wavelength increases into the red and near infrared regions of the spectrum (Grenfell and Perovich, 1981).

For brine it is appropriate to use a spectral absorption coefficient $\kappa_b(\lambda)$ representative of natural arctic waters rather than coefficients for highly purified laboratory water (e.g., Pope and Fry, 1997). In Fig. 2.3, values of $\kappa_b(\lambda)$ for wavelengths less than 800 nm were estimated using spectral data from Smith and Baker (1981). These values were scaled to correspond with attenuation measurements at 490 nm made by Smith (1973) beneath Ice Island T-3 in the central Beaufort Sea. Data from Irvine and Pollack (1968) were used for $\kappa_b(\lambda)$ at wavelengths longer than 800 nm.

Absorption induced by air or vapor is negligible in comparison to that of brine or pure ice and we will assume that $\kappa_g(\lambda) = 0$. We have little information about $\kappa_s(\lambda)$, but we believe it is small relative to $\kappa_i(\lambda)$. The value of $\kappa_p(\lambda)$ depends on local particulate compositions. We expect that $\kappa_p(\lambda)$ is large compared to $\kappa_i(\lambda)$, but the particulate nature of the material must also be considered. Because we can predict the fractional

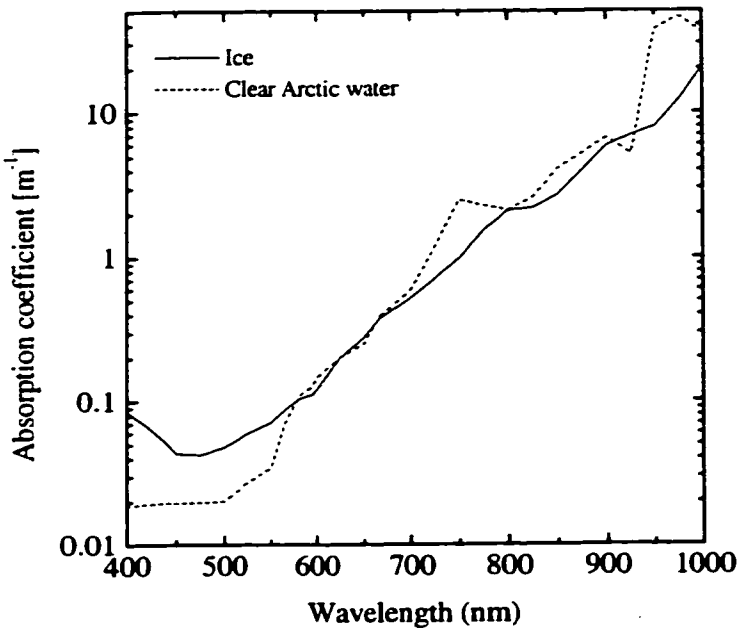

Figure 2.3. Spectral absorption coefficients for pure ice (κ_i) and clear Arctic water (κ_b) based on data from Grenfell and Perovich (1981), Smith (1973), Smith and Baker (1981), and Irvine and Pollack (1968).

volumes and know the individual $\kappa(\lambda)$ values for the major constituents in sea ice, prediction of the bulk $\kappa(\lambda)$ is straightforward when the ice contains little or no particulate material.

Scattering

Because scattering occurs wherever there is a discontinuity in the real part of the refractive index (n), inclusions of brine, vapor, precipitated salt crystals, and particulates will all contribute to the scattering observed in sea ice. The total σ is defined as the sum of scattering coefficients for each constituent in the ice,

$$\sigma = \sigma_b + \sigma_g + \sigma_s + \sigma_p. \tag{2.3}$$

Since the inclusions are generally much larger than the wavelength, σ is taken to be independent of the wavelength. Scattering from the ice lattice itself is neglected and each type of inhomogeneity is assumed to consist of discrete spheres with radius r,

number density $N(r)$, phase function $p(\theta)$, and scattering efficiency $Q(r)$. Inclusions are assumed to be distributed uniformly throughout the sample. For inclusion type j

$$\sigma_j = \int_{r_{min}}^{r_{max}} Q_j(r)\pi r^2 N_j(r)dr . \tag{2.4}$$

For scattering by brine inclusions, Grenfell's treatment did not have access to quantitative data on the distribution of sizes and shapes of brine inclusions. For a population of monodisperse equivalent spheres, the scattering coefficient can be written as

$$\sigma_b = Q(r_{sp})\pi r_{sp}^2 N_b(r_{sp}). \tag{2.5}$$

The equivalent spherical radius, r_{sp}, relates to the population of uniform spherical brine inclusions with the same scattering properties as the full distribution. $Q(r)$ is a function not only of the inclusion size, but also the wavelength and the refractive index difference between the scatterer and its environment. $Q(r)$ displays a series of maxima and minima, but tends to the limit of 2 as $r >> \lambda$.

In general, we expect σ_b to have the largest value for the major constituents at temperatures above –23 °C. Light (1995) predicted σ_b to range from 0.10 to 0.53 mm^{-1} and σ_g to have a value of 0.05 mm^{-1} for ice with a salinity of 15‰. At lower temperatures, hydrohalite was found to be the dominant scatterer, and σ_s was estimated to be 1.4 mm^{-1} at –30 °C. Light et al. (1998) found that the scattering coefficient for lithogenic particulates was small compared to the scattering by brine and vapor inclusions, and that it was more important to know the spectral absorption coefficient for particulates than the details of their scattering properties.

The phase function $p(\theta)$ describes the angular redistribution of light during an individual scattering event. The most direct way of estimating $p(\theta)$ for brine pockets, vapor bubbles, precipitated salts, and particulate inclusions is to apply Mie theory (e.g., Wiscombe, 1979) to equivalent spherical inclusions. These computations require knowledge of n relative to n_i for each constituent. For ice, n_i values do not vary strongly with temperature and have been well established over the visible spectrum. At 500 nm, for example, $n_i = 1.313$. Because of large temperature-dependent changes that occur in

the composition of brine in sea ice, n_b(500 nm) increases from approximately 1.340 to 1.395 as the temperature decreases from –2 to –30 °C (Maykut and Light, 1995). We take n_g to be unity at all wavelengths and all temperatures. Generally accepted average values of n_s for mirabilite and hydrohalite are 1.396 and 1.43, respectively. The values of n_p for particulates vary widely, but Light et al. (1998) took $n_p = 1.54$ to be representative at all wavelengths.

A convenient way to compare phase functions is to compare their asymmetry parameters, g, where

$$g = \int_{1}^{-1} \mu \, p(\mu) \, d\mu \,, \tag{2.6}$$

where $\mu = \cos \theta$. In general, the refractive index contrast for brine in ice is small, resulting in strongly forward-peaked phase functions and large g. Because n_b increases with decreasing temperature, the refractive index contrast for brine in ice also increases as the ice cools. The Mie-computed asymmetry parameter for brine inclusions in ice varies from 0.995 to 0.982 as temperature decreases from –4 to –28 °C. The index contrast for vapor in ice is larger than that for brine in ice, producing a less strongly forward-peaked phase function and smaller g. For vapor bubbles in ice, $g \sim 0.856$. For precipitated salts, Light (1995) used $g = 0.97 - 0.99$. Because the relative refractive indices for all constituents show only small variation with wavelength, $p(\theta)$ is taken to be wavelength independent for all scatterers.

Because the solutions to Mie theory cannot generally be analytically expressed, Henyey and Greenstein (1941) developed an analytical function to approximate strongly-forward Mie phase functions. The Henyey-Greenstein phase function is given by:

$$p_{HG}(\theta) = \frac{1 - g^2}{(1 + g^2 - 2g\cos\theta)^{3/2}} \,. \tag{2.7}$$

p_{HG} is frequently used in radiative transfer modeling. The bulk $p(\theta)$ appropriate for sea ice is the scattering-coefficient weighted sum of the $p(\theta)$ values for each constituent,

$$p(\theta) = \frac{p(\theta)_b \sigma_b + p(\theta)_g \sigma_g + p(\theta)_s \sigma_s + p(\theta)_p \sigma_p}{\sigma}. \qquad (2.8)$$

This expression is also appropriate for defining the bulk value of g. Knowledge of g is important to a successful structural-optical model. The scattering in sea ice is generally forward, for which g is close to unity. For this reason, small variations in g have a large effect on the AOPs of the ice.

To estimate bulk scattering coefficients and asymmetry parameters for sea ice, Mobley et al. (1998) used optical beamspread measurements in first year ice near Point Barrow, Alaska. Their inferred values for σ ranged from 0.20 to 0.25 mm^{-1} and g values ranged from 0.95 to 0.98. These values of g are considerably more forward-peaked than previous estimates.

2.2.3 Structural-Optical Treatment

Light (1995) used the above formulation to develop and test a structural-optical model for sea ice in the precipitated salt regime ($T < -8.2$ °C). This model predicts how the relative volumes of brine pockets, vapor bubbles, and precipitated salts change with temperature by using the phase relation parameterizations of Cox and Weeks (1983). From information about the initial ice microstructure, along with assumptions about the salt crystal precipitation pattern and effective crystal size, the model calculates the effect of temperature changes on the absorption and scattering coefficients and phase function of the ice. Once the IOPs are identified, a four-stream radiative transfer model (Grenfell, 1991) is used to compute the AOPs of the ice.

To test and verify this model, data on the optical and structural properties of sea ice were required. Available optical measurements from natural ice (Grenfell and Maykut, 1977; Grenfell and Perovich, 1984) and laboratory grown ice (Perovich, 1979) had all been made in the presence of large vertical temperature and structural gradients. These conditions make identifying specific relationships between structural and optical properties difficult. To remedy this problem, measurements were made of isothermal samples of laboratory-grown sea ice where gradients in structural properties were minimized, thus greatly simplifying the theoretical treatment. In Fig. 2.4, observed and

model predicted albedo and transmissivity of a 10 cm thick, isothermal sample of laboratory-grown sea ice are compared at selected wavelengths. The model appears to do an excellent job of predicting the observed changes in the AOPs throughout the precipitated salt regime.

Despite the apparent success of these predictions, there remain significant problems in the model. The assumption was made that although brine inclusions are generally ellipsoidal they can be treated as equivalent spheres. This permits the use of Mie theory to predict single scattering phase functions for spherical vapor bubbles as well as brine pockets. However, when the Mie predictions were combined with the available observations of inclusion distributions at -8 °C, the structural-optical model predicted considerably less scattering than observed. It was suspected that this is due to the presence of vapor bubbles forming within the brine pockets at higher temperatures. While this phenomenon has not been explicitly documented for sea ice, its role in the optical properties of the ice has been discussed by Grenfell (1983). No attempt was made to account for scattering by such compound inclusions in this model. It is also possible that the equivalent sphere assumption becomes less accurate as the ice becomes warmer and the brine pockets become more elongated. Lacking information on scattering by compound inclusions and on the validity of the equivalent sphere treatment, the phase function for the brine pockets was tuned to obtain agreement with observations. The phase function needed was part way between that for a brine pocket and that for an air bubble.

In addition to these problems, this study did not consider the prediction of optical properties for sea ice at temperatures above –8 °C. This is an important region not only because temperatures are higher than -8 °C during most of the spring and summer when incoming shortwave radiation is greatest, but also because the lower portion of the ice sheet is above this temperature throughout the year. At the onset of the melt season, warming is accompanied by significant increases in brine and air volume in first-year sea ice and, according to Light (1995), this translates directly into enhanced scattering cross-sections for brine pockets and vapor bubbles. However, preliminary observations

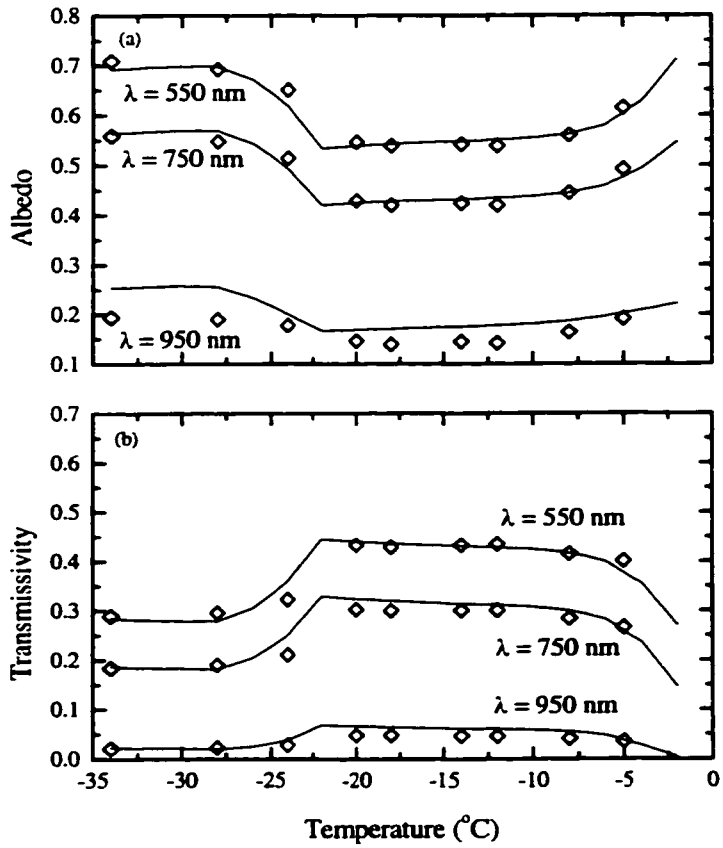

Figure 2.4 Temperature-dependent observations (diamond symbol) and model predictions (lines) of (a) albedo and (b) transmissivity for a 10-cm-thick laboratory-grown sea ice core sample, after Light (1995).

indicate that as the brine and gas volumes continue to increase, the ice structure undergoes a transition where inclusions no longer remain isolated. Instead, they begin to merge and coalesce, forming elongated and connected inclusions. The total effective scattering cross-section of the medium is reduced as the network of inclusions becomes more connected and brine is redistributed in the ice. Grenfell (1983) proposed a theoretical treatment describing the evolution of ice structure at high temperatures, but this treatment has never been tested.

Despite its limitations, the effort of Light (1995) represents a significant step in the evolution of a complete structural-optical treatment for sea ice. To progress further, however, we need more detailed data on the structural dependence of the optical

properties of sea ice. In particular, we would like to have temperature-dependent measurements of brine and vapor inclusion size distributions together with simultaneous optical property data from natural sea ice samples. In the following chapter we describe an experimental plan for acquiring these data.

CHAPTER THREE
EXPERIMENTAL APPROACH

While the models of Grenfell (1983, 1991) and Light (1995) lay a foundation for studying the relationships between the structural and optical properties of sea ice, they have several limitations. Foremost, the model for cold sea ice (Light, 1995) was only able to account for about 50% of the scattering observed in albedo and transmissivity data taken at –8 °C. The discrepancy was attributed to the presence of compound inclusions of vapor bubbles within brine pockets, but this explanation remains untested. Furthermore, details of structural-optical relationships in warm ice (T > -6 °C) have yet to be studied. This is a climatically important temperature regime, as much of the ice pack is at temperatures higher than –6 °C during a significant part of the annual cycle.

Although some imaging studies of the microstructure of sea ice have been carried out (e.g., Eicken, 1993; Perovich and Gow, 1991, 1996), the results of these observations have not explained the relationship between ice structure and its optical properties. We believe existing observations of the microstructure of sea ice to be deficient in several respects: (i) observations were made at too low a magnification to resolve small inclusions ($r < 25$ μm), (ii) structural observations were not necessarily made concurrently with optical measurements (iii) observations were produced almost exclusively from horizontal thin sections which masked important vertical structure within the ice, and (iv) data were taken from laboratory grown sea ice, probably a poor proxy for naturally-formed inclusions (Light, 1995). There are also uncertainties in the albedo and transmissivity data used to validate the Light (1995) model. In particular, measurements were made on a core sample with finite horizontal extent. Lacking a radiative transfer model that accounts for losses at the core walls makes the interpretation of these measurements problematic. Clearly, the lack of structural-optical data has limited progress in understanding and predicting the optical evolution of sea ice.

The primary goal of the present study is to acquire a detailed data set and use it to further our quantitative understanding of structural-optical relationships in sea ice. Results from this work will support efforts to predict the optical properties of sea ice

from observed physical properties. Structural-optical data collected in this study provide insights into how the microstructural and optical properties of first-year sea ice change with temperature, particularly for $T > -8$ °C. Natural, isothermal samples of sea ice were used to obtain information about the size and number distributions of inclusions, the interactions between inclusions, and the resulting apparent optical properties (AOPs) of the ice. A cylindrical radiative transfer model was used to infer inherent optical properties (IOPs) from the AOP data. With these data and this analysis tool, we developed the foundation needed for improving and extending our structural-optical model to warmer ice. While the questions addressed in this study complement our earlier work in the precipitated salt regime, the current scope is broader and requires substantial experimental and theoretical inquiry.

3.1 Ice Samples

This study focuses on first-year ice, as its crystal structure has been studied extensively (e.g., Weeks and Hamilton, 1962; Weeks and Ackley, 1982) and we believe that understanding the interaction of light with first-year ice is the first step in a general understanding of sea ice structural-optical relationships. Ice cores used in this experiment were extracted from first-year shorefast ice at the EMPOSI field site off Point Barrow, Alaska in May 1994. The ice was 1.65 - 1.75 m thick. Temperatures in the upper 0.5 m of ice were approximately –5.5 °C and increased linearly with depth. Ice salinities resembled typical c-shaped profiles for first-year ice with values ranging from 7 – 9‰ near the upper surface, 4 – 5‰ in the interior, and about 10‰ near the bottom. Brine volumes ranged from 5 – 12%. Gas volumes were about 4% in the upper 10 cm of the ice cover, but less than 1% in the remainder of the ice (see Perovich et al., 1998a).

Cores 10 cm in diameter were removed from the upper meter of the ice and shipped from Barrow to Seattle in crates packed with dry ice. The cores were stored in a laboratory freezer at approximately –20 °C. Our interest is in characterizing congelation ice. This ice has small gas volume, unlike the ice at the surface, and brine inclusions tend to be isolated, unlike ice near the ice-ocean interface. To study such

interior ice, samples were taken exclusively from the lower portions of the cores, corresponding to 60 – 80 cm depth in the ice.

3.2 Laboratory Setup

Since it is impractical to maintain a suitable temperature-controlled environment at a field site, this experiment was designed to be carried out in a laboratory cold room where temperatures between 0 and –30 °C can easily be maintained. Both the structural and optical measurements were made in this cold room. Experiments were first conducted at –15 °C, where the brine volume is small and brine drainage is minimal. To obtain data on the temperature response of the ice, samples were then cooled to –30 °C and subsequently warmed to –2 °C where changes in the physical and optical properties were monitored at 2 – 5 °C intervals.

The success of this experiment relied on our ability to make structural and optical measurements on samples with similar thermal history and ice structure. For this reason, structural and optical samples were taken from adjacent locations on the same ice core, and the structural and optical measurements made nearly simultaneously.

3.2.1 Structural Measurements

Although we cannot directly measure $\kappa(\lambda)$, σ, and $p(\theta)$ in a multiply scattering medium, we can observe physical properties that are directly related, specifically: (i) the size distribution and number density of inclusions, (ii) inclusion shapes, and (iii) the orientation and spatial grouping of inclusions. However, structural properties are extremely sensitive to temperature and different types of inclusions respond differently to specific temperature changes. To separate the effects of different inclusion types on the optical properties, we monitored structural and optical changes over a wide range of temperatures. Structural features of interest include: (i) changes in brine inclusion size, shape, and number (ii) presence, formation, and modification of vapor bubbles, (iii) interactions between vapor bubbles and brine pockets, and (iv) precipitation and dissolution of solid salt crystals. Detailed studies of these properties and their changes with temperature have never been carried out.

Previous attempts to monitor the microstructure of sea ice have almost exclusively relied upon observations of horizontal thin sections (Light, 1995; Perovich and Gow, 1991, 1996; Eicken, 1993). Because brine pockets in first-year ice tend to be vertically oriented, this view neglects fundamental information about the structure of the ice. To obtain a more complete picture of the microstructure, we used thin, translucent slabs cut vertically from the ice for our structural observations. By mounting these thin sections between two pieces of clear glass we were able to keep them vertical while preserving the natural structure of the ice even at quite high temperatures and large porosities. At high temperatures, the loss of brine makes thin section samples extremely fragile, but the sealed glass plates helped keep the structure intact.

We used a black and white charge coupled device video camera equipped with a high magnification zoom lens to image the thin sections in transmitted light. The high magnification lens gave us the ability to focus on details too small to have been resolved in previous studies. In particular, we observed inclusions with diameters as small as 10 μm, interactions between inclusions, and some individual precipitated salt crystals. Our objective, however, was to record features and processes that are key to understanding the optical properties of the ice, not to necessarily resolve the smallest features of the ice microstructure.

Experiments were initially conducted at −15 °C to identify size distributions for brine pockets and gas bubbles in cold ice. We chose to do this characterization at −15 °C because at this temperature brine inclusions are small and remain intact. Because changes in the ice microstructure are sensitive to changes in temperature, we were particularly interested in observing the temperature-dependent evolution of these inclusions. A number of scenes representative of the sample were selected and imaged so that the progress of specific features could be monitored.

Analysis of these images was then used to characterize the structural changes accompanying the optical changes. The observed structure at −15 °C was characterized and used to model the observed AOPs at −15 °C. This served as a foundation for the structural-optical model. As the ice was cooled, data was obtained on the precipitation

patterns of the salt crystals, and interactions between brine pockets and vapor bubbles. These observations were then used to model the optical response to the decreased temperature. As the ice warmed, changes in the ice structure were monitored. We were specifically interested in the dissolution of precipitated salts, formation of vapor bubbles, interactions between brine inclusions and vapor bubbles, and interactions between brine inclusions, particularly brine pocket merging.

3.2.2 Optical Measurements

While a large amount of data on the AOPs of sea ice has been collected, few if any have been acquired for ice with uniform structural properties. Relating AOPs to IOPs is difficult when the ice is spatially inhomogeneous. For this reason, we acquired backscattered and transmitted radiance data from samples that were as structurally uniform as possible. To ensure sample uniformity, we designed the optical experiment for small samples and kept the samples isothermal.

The samples were illumined with collimated visible radiation normally incident on the top surface of the cylindrical domain. Spectral backscattered and transmitted radiance distributions were then measured with a single fiber optic probe coupled to a spectrophotometer. Data were collected at the same temperature intervals as the structural measurements.

To interpret our radiance observations, a radiative transfer model was built specifically for the cylindrical geometry of our core samples. The model was formulated using a backward Monte Carlo method. By not restricting the medium to be plane parallel with infinite horizontal extent, we were able to test assumptions relating to the boundary conditions of the finite diameter core, i.e., the effect of light leakage at the core boundaries. Determination of the optical properties of the samples was made with much less uncertainty than previously possible (e.g., Light, 1995).

The details of the structural measurements from thin sections are described in Chapter 4. Chapter 5 presents the formulation of the Monte Carlo radiative transfer model, and the measurement of AOPs is described in Chapter 6. Discussion of the structural-optical model and general conclusions will be presented in Chapters 7 and 8.

CHAPTER FOUR
MICROSTRUCTURE OF FIRST-YEAR SEA ICE

In the first stage of this study, we used high resolution imagery to document the microstructure of first-year sea ice, and observe how this structure changes with temperature. The primary objective was to obtain quantitative information on (i) the size and number distributions of brine pockets, vapor bubbles, and precipitated salts, and (ii) interactions between various types of inclusions as the sample temperature is changed.

4.1 Sample Preparation

Ice samples were prepared at –15 °C, as brine inclusions tend to be relatively small and isolated at this temperature. The ice was easily sawed, microtomed, and polished without the excessive brine drainage that occurs at higher temperatures. A section approximately 10 cm thick was first cut from the lower part of the core using a bandsaw. This section was then divided into two 5 cm thick sections, one part being reserved for the optical measurements, and the other being used for vertical thin sections and salinity sampling. This latter section was cut unto several square vertical slabs (approximately 0.5 cm thick and 9 cm wide). The slab with the fewest obvious large-scale variations, drainage structures, and structural weaknesses was selected for thin section preparation. The other vertical sections were saved in plastic bags as back-up and for salinity samples. The best slab was frozen to a single glass plate (~3 mm thick) using a few drops of fresh water at the corners of the sample. The top surface of the slab was microtomed until flat. A clean glass plate was then mounted onto this surface, again using fresh water to attach the sample. The first glass plate was then removed and the underlying surface microtomed until the total sample thickness was approximately 2.0 mm. This was the lower limit for thickness because of the fragility of the samples. Finally, a clean glass plate was sealed on top of the freshly microtomed surface by applying clear silicon caulk around the edge of the sample and placing the glass plate on

top of the ice. Once the caulk set, this glass-ice-glass sandwich was mounted in a sample holder. The sample was kept vertical, so that drainage features would respond as similarly as possible to in situ conditions. The left-over slabs were then melted and their salinity measured using a Beckman Solubridge (Model RB-6).

4.2 Laboratory Setup

The components of the imaging system included a light source, video camera, lens, frame grabber, personal computer, and viewing monitor. To reduce the effects of vibrations, components in the cold room were mounted on a 2-meter long heavy optical rail. Figure 4.1 shows a schematic of the laboratory imaging system.

Images were captured with a black and white Panasonic CCD video camera (model WV-BP500) with 682 by 492 pixel resolution. The camera was equipped with a parfocal microscope zoom lens (Leica MonoZoom 7 Optical System) and a 3.0X amplifier. The camera and lens were mounted on a translation stage with a micrometer adjustment. The focus was controlled by adjusting the distance between the camera and the sample. Images obtained by the CCD camera were fed to a black and white high resolution monitor visible through the cold room window. This monitor was used to select and focus images. Images were also fed to a video frame grabber (Scion VG-5) mounted in a MacIntosh Power PC running image processing software (NIH Image version 1.57), where they were captured and saved to disk. The image processing software was used to capture both still and time-lapse images.

Information on crystallography is best obtained from images recorded in polarized light, whereas inclusions of brine and gas are best viewed in transmitted and reflected light that need not be polarized. Since our primary interest in this experiment was to obtain information on the inclusions, we experimented with illuminating the sample with both reflected and transmitted light. Images with acceptably uniform lighting and high contrast were obtained with transmitted light from a diffuse source. To achieve this, an incandescent light source was aimed at a diffusely reflecting Spectralon® panel

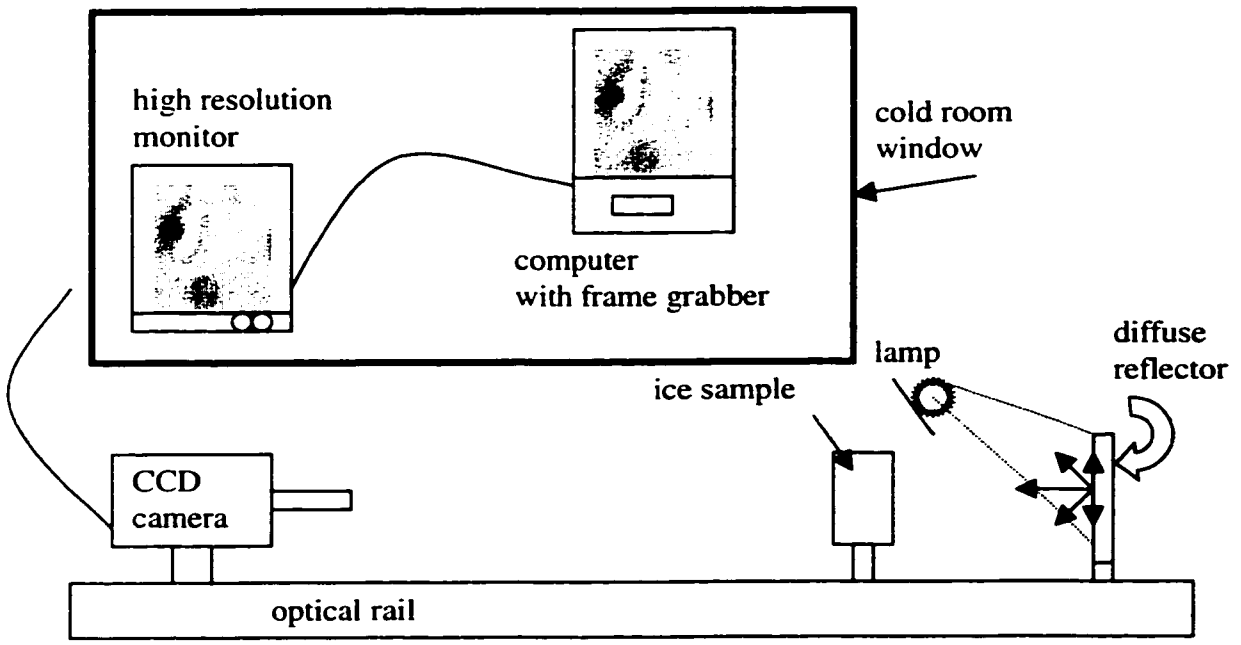

Figure 4.1. Schematic of imaging system for observing ice microstructure. The optical rail, sample, light source, diffusely reflecting target, and CCD camera are in the cold room. The focusing monitor and computer with frame grabber are outside of the cold room.

mounted directly behind the sample. The source was baffled to prevent direct radiation from illuminating the sample.

The sample was mounted on an x-y translation stage, enabling the thin section to be repeatably translated as much as 3 cm laterally and 3 cm vertically. This made it simple to revisit particular fields of view and to monitor multiple scenes during experiments where the temperature was increased or decreased. Image sizes were calibrated using a grid with ruled lines separated by 50 microns. Images of the grid were taken for each magnification and archived.

4.3 Observations at –15 °C

Before attempting to learn how sea ice inclusions change with temperature, we first documented the distributions and characteristics of these inclusions at a particular reference temperature, in this case –15 °C. Figure 4.2 shows a vertical thick section of

our initial first-year ice sample illuminated in transmitted light. The most striking features in this ice are long, vertically-oriented inclusions, and vertically-oriented strings of smaller inclusions. The distribution of inclusions is noticeably inhomogeneous, with areas where the inclusion density is large and areas where the ice appears devoid of inclusions. This initial sample had a salinity of 4.7$^{o}/_{oo}$ and the results of a mass-volume analysis indicated its density was 0.915 Mg m^{-3}.

To obtain a more detailed look at the microstructure, the thick section was microtomed down to 2.04 mm in thickness and the video imaging system was used to create a mosaic image (Fig. 4.3). This mosaic is composed of 30 individual images, each with a field of view 1.9 x 1.4 mm. After registering the 30 images, the dimensions of the composite scene are approximately 4.7 x 12.1 mm. Inclusions of brine and vapor

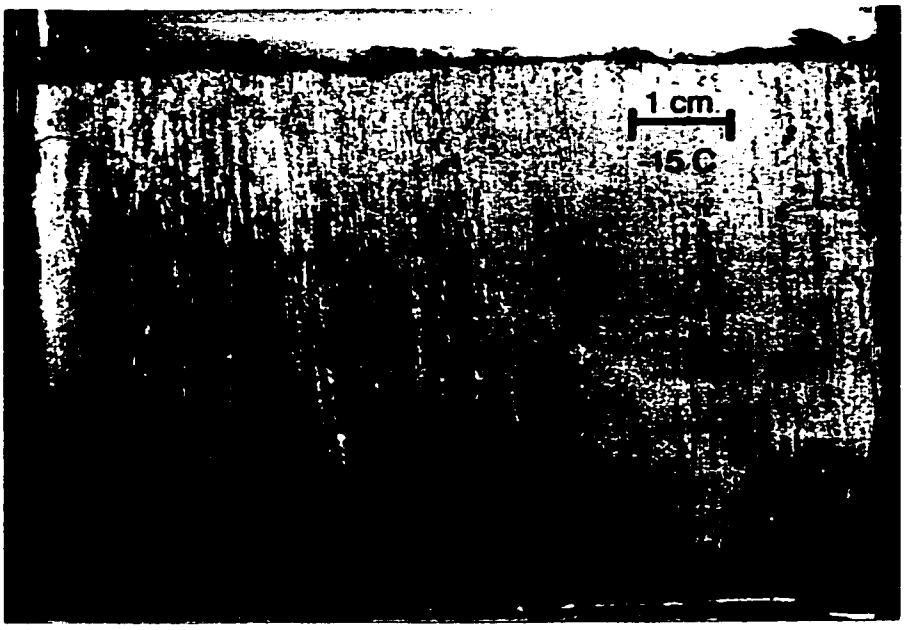

Figure 4.2. Photograph of vertical thick section of first-year sea ice in transmitted light. The inhomogeneity of inclusion densities is striking, as is the extent to which the structure is vertically oriented. The magnification is 1.2.

Figure 4.3. Photomosaic of vertical thin section of first-year ice in transmitted light. Ten boxed regions refer to subregions shown in Fig. 4.4. Overall dimensions of scene are approximately 12.1 x 4.7 mm, and the magnification is 15. Arrows indicate examples of (1) brine tubes, (2) brine pockets, (3) vapor bubbles, (4) drained inclusions, (5) transparent areas, and (6) poorly-defined inclusions.

are visible because light passing through the thin section is refracted and reflected by refractive index boundaries. The edges of inclusions appear dark because of the total internal reflection that occurs at these boundaries. This effect is more pronounced for vapor than for brine inclusions because the refractive index contrast for vapor in ice is larger than for brine in ice. Several types of features stand out: elongated brine tubes (arrow 1), smaller, isolated brine pockets (arrow 2), and vapor bubbles within brine inclusions (arrow 3). Brine features that appear to have excessively high contrast are inclusions that were cut open and drained during sample preparation (arrow 4). Vapor bubbles within brine pockets have similarly high contrast but can usually be discerned by their nearly spherical shape. The horizontal stripes across the image are scratches produced when the sample was cut with the microtome blade. The microtome cut was intentionally made horizontally across the sample, to avoid creating artifacts that could interfere with analyzing the vertically-oriented structure.

As in the lower resolution photograph (Fig 4.2), the ice microstructure is very inhomogeneous and has obvious directionality. Long brine tubes dominate, yet there are many clusters of small brine pockets, frequently found stacked in vertical strings. There are also areas where no inclusions exist in the ice, and the ice appears highly transparent (arrow 5). These areas appear to be as wide as 0.250 mm and have lengths in excess of 5 mm. The size of these areas is of the same order as the size of typical lamellae at the ice growth interface, suggesting that the inclusion strings formed between lamellae.

4.3.1 Brine Inclusions

Characterization of the inclusions began with estimating the number density and sizes of the brine tubes in the mosaic (Fig. 4.3). The sample contained twenty-three brine tubes in a volume of 84.5 mm^3, corresponding to a number density of 0.27 per mm^3. All tubes were oriented vertically or near-vertically in the ice. Tube lengths as long as 10 mm and tube diameters between 60 and 150 μm were observed. The height-to-diameter aspect ratio ranged between 5 and 45. Inclusions with

maximum lengths greater than 500 μm and aspect ratios greater than 5 were classified as brine tubes. Eight of the 23 tubes were observed to contain vapor bubbles. Clearly, a large portion of the total brine visible in the image was contained within these brine tubes.

However, there were also large numbers of smaller, isolated brine pockets which must also contribute to the total light scattering. While large ellipsoidal pockets are easily seen in the mosaic image, the smaller pockets are difficult to resolve. For this reason, the counting was done using ten subregions from the mosaic that were enlarged for viewing. These individual images are shown in Fig. 4.4. The total volume sampled was 48.8 mm^3. The selected scenes were representative of the general appearance of the overall microstructure, with both areas of high inclusion density and clear ice included. Areas with obvious out-of-focus features were avoided. A total of 1616 brine pockets were identified, giving a number density for brine pockets of 32.7 per mm^3. The number densities ranged between 16 and 52 per mm^3 for the ten individual scenes. Pockets were sorted by their longest dimension (l) into seven size bins (see Table 4.1). The smallest pockets resolved at this magnification have $l \sim 10$ μm and the longest have a maximum dimension as large as 500 μm.

Observed brine inclusions had ellipsoidal, spherical, and irregular shapes. The smallest inclusions were approximately spherical (aspect ratio = 1). Aspect ratios tended to increase as inclusion size increased. The smallest pockets usually appeared in clusters or vertical strings, and it was often difficult to tell whether they contained vapor bubbles or not. Examples of these very small pockets are shown in Fig. 4.5. Mid-sized pockets ($l \sim 60$ - 150 μm) frequently appeared in vertical strings, and occasionally included vapor bubbles.

The phase relation parameterizations of Cox and Weeks (1983) were used to predict the fractional brine volume for this ice (salinity = 4.7‰) to be 0.019 at –15 °C. The contributions of brine tubes alone account for 45% of this value. When the contribution

Figure 4.4. Ten subregions from the mosaic in Fig. 4.3 used for counting size distributions of brine pockets and vapor bubbles. Image sizes vary; largest is 1.9 by 1.4 mm. The scale for each image is shown. For (a) and (b), magnification is 56; (c) – (j) have magnification 32.

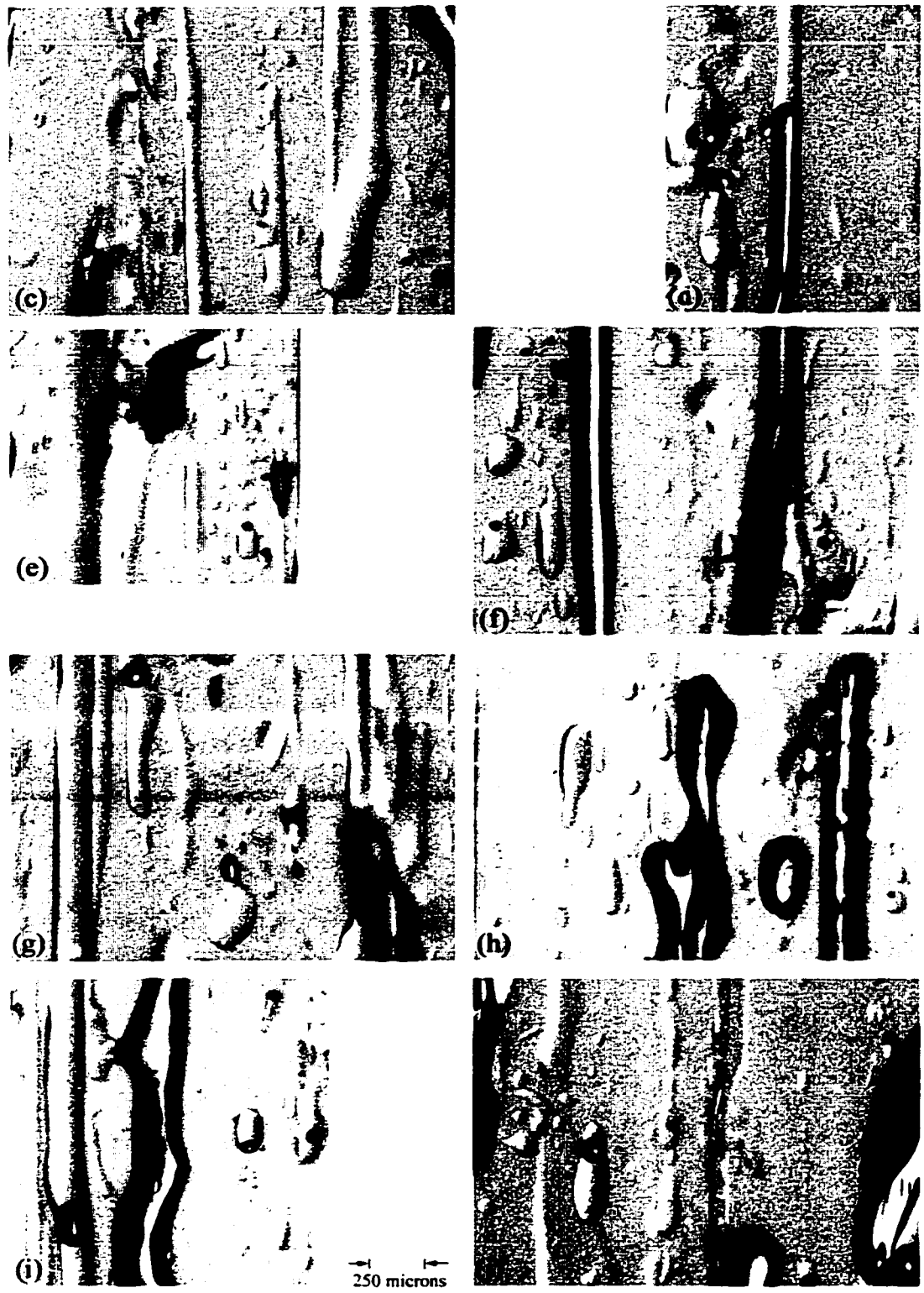

Figure 4.4. Continued

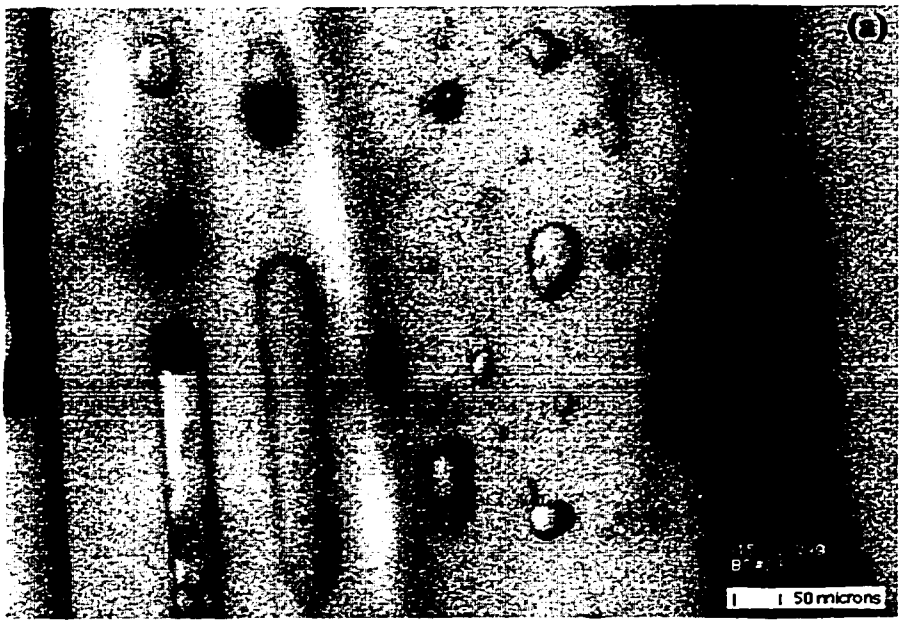

Figure 4.5. Images showing examples of small brine pockets. The pockets visible in (a) are loosely clustered, whereas the pockets visible in (b) are grouped in vertical strings. The smallest pockets visible have diameter ~ 5 μm. The magnification is 110 and 56 for (a) and (b) respectively.

Table 4.1. Size distribution information for brine inclusions in first-year sea ice samples. Brine tubes are given as their own class and brine pockets are divided into seven size classes. The number density, average aspect ratio, and percent of predicted brine volume are computed for each bin size.

Bin number	Maximum dimension, l (μm)	Number counted	Sample volume (mm^3)	Number density (mm^{-3})	Average aspect ratio	Percent of predicted brine volume
1	$l < 30$	1244	48.8	25.47	1.0	0.23
2	$30 < l < 60$	108	48.8	2.21	1.5	0.24
3	$60 < l < 90$	112	48.8	2.29	1.8	0.81
4	$90 < l < 150$	74	48.8	1.52	2.3	1.19
5	$150 < l < 230$	32	48.8	0.66	3.9	0.81
6	$230 < l < 300$	27	48.8	0.55	3.5	2.29
7	$300 < l < 500$	19	84.5	0.22	4.8	1.70
	all tubes	23	84.5	0.27	23.0	44.63
	TOTALS	1639		33.21		51.90

from brine pockets is included, 52% of this predicted value is explained. Where is the other 48% of the brine? Referring to the mosaic image in Fig. 4.3 there are areas that clearly contain brine, yet are not counted because they do not have well defined boundaries and are thus difficult to classify and count (e.g., arrow 6 in Fig. 4.3). These features do, however, contribute to the total brine volume and to the total scattering. But they probably do not explain all of the missing brine. It is more likely, we believe, that the missing brine is contained in a small number of very large brine tubes that were within the sample but were not imaged.

Our estimate of approximately 33 brine inclusions per mm^3 is an order of magnitude larger than previously reported estimates. Light (1995) reported 1.3 inclusions per mm^3 based on photographs of horizontal thin sections from laboratory grown ice. Perovich and Gow (1996) counted inclusions in six horizontal thin sections of first-year ice and found number densities ranging from 1.0 to 4.5 per mm^3. It is likely that this discrepancy is due to the problem of resolving very small brine inclusions. The smallest inclusions reported by Perovich and Gow had diameters of approximately 50 μm. Because the samples they used were horizontal thin sections, they observed only the

horizontal inclusion diameter. The inclusion diameter viewed in a horizontal sample corresponds to l divided by the aspect ratio. An inclusion with diameter 50 μm and aspect ratio 1.8 would have $l = 90$ μm and would be counted in our third smallest (60 μm $< l <$ 90 μm) bin. Perovich and Gow were not able to detect the types of brine inclusions in our first two bins and therefore would be unable to resolve the smallest 83% of the inclusions counted in the present study. If the two smallest bins from our analysis are omitted, the brine pocket number densities are approximately 5 per mm^3, a value closer to what Perovich and Gow reported. Interestingly, we did not observe inclusions with horizontal cross-sectional areas as large as Perovich and Gow report. Their cumulative size distribution shows inclusions with diameters larger than 600 μm. The largest dimension we measured in the horizontal plane was a tube with diameter 230 μm. The largest brine pockets had $l = 500$ μm and aspect ratio 4.8, indicating a diameter of approximately 100 μm. Other work by Cole and Shapiro (1998) reports average inclusion diameters in the horizontal plane of 84 μm. In the present study, the number weighted average diameter for all brine pockets is approximately 20 μm. The average diameter of our largest size bin (excluding brine tubes) is approximately 80 μm, and the average diameter of the observed brine tubes is 100 μm.

Because this study uses observations from vertical thin sections, a different perspective on the microstructure is obtained. Previous studies that have looked exclusively at horizontal thin sections have only observed cross-sections of the inclusions. In particular, this means that brine tubes appeared no different from large ellipsoidal brine pockets. No information about the fundamental, vertically-oriented structure is available from horizontal thin sections. In particular, this makes accounting for the total brine volume difficult when using only horizontal thin sections, as the vertical view reveals the presence of large-aspect tubes that contain a majority of the total brine.

4.3.2 Vapor Bubbles

Entrapment of bubbles within the ice or brine pockets can result from supersaturated air that is released from the water during initial freezing or from biological or chemical gas release in the water below the ice sheet (Grenfell, 1983). Additionally, the formation of vapor bubbles within warming brine pockets is predicted from the conservation of volume. A brine inclusion that warms and enlarges should form a vapor bubble to fill the space created when lower density ice melts into higher density liquid. Such bubbles should continue to enlarge as the ice is warmed. As the ice cools, this process should be reversible and the bubbles should shrink and possibly even disappear. This assumes, of course, that the inclusions are isolated and not interconnected in some way.

The total sample volume shown in Fig. 4.4 contained 59 vapor bubbles, a number density of 1.21 per mm^3. All vapor bubbles were within brine inclusions, and none were observed alone in the ice. The diameter of the observed bubbles ranged from 9 to 133 μm at –15 °C, with a mean of approximately 30 μm. The bubble size distribution is summarized in Table 4.2.

Existing vapor bubble data for ice from a freezing lead (Grenfell, 1983) indicate significantly larger bubbles, with diameters ranging from 0.2 to 4 mm. No bubbles this large are observed in our samples. Grenfell (1983) also reported a number density of 0.1 per mm^3, an order of magnitude smaller than our observations. Similar data from Gavrilo and Gaitskhoki (1970) concur with the observations by Grenfell (1983). It is likely, however, that both of these earlier observations were of bubbles entrained in the ice during its initial formation. Presumably much of the gas dissolved in the water column is released during the initial formation of the ice cover, as would have been the case for ice at the surface of a freezing lead. In the interior ice examined for the present study, the ice grew much more slowly as it was accreted to the base of the existing ice cover. For this reason, we see no bubbles in the ice itself, only bubbles that have formed within brine inclusions due to the density difference between ice and brine.

Table 4.2. Observed size and number of vapor bubbles.

Bin number	Maximum dimension, l (μm)	Number density (mm^{-3})
1	$l < 30$	0.76
2	$30 < l < 60$	0.25
3	$60 < l < 133$	0.20
	TOTAL	1.21

Figure 4.6 shows vapor bubbles within brine inclusions at –5 °C. The number concentration here is approximately 3 per mm^3. This number density is larger than the 1.2 per mm^3 measured in the 10 scenes at –15 °C possibly because of sample inhomogeneity, but more likely because the higher temperature of the sample should have induced the formation of new vapor bubbles. As seen in the image, the position of the vapor bubbles within inclusions varies (arrows 1), suggesting that surface forces are stronger than those due to buoyancy. Vapor bubbles within brine tubes are frequently too large to maintain their spherical shape, as is also seen in the figure (arrow 2).

4.3.3 Mirabilite Crystals

Mirabilite crystals ($Na_2SO_4 \cdot 10H_2O$) were frequently observed in our samples at temperatures lower than –8.2 °C. Figure 4.7 shows examples of mirabilite crystals observed in first-year ice at –15 °C. Most commonly, crystals were observed in piles at the bottom of brine tubes (arrow 1), in clusters strewn throughout the tubes (arrow 2), stuck at narrow pinches in tubes (arrow 3), or resting against vapor bubbles (see Fig 4.8a). When piled at the bottom of a brine tube, the crystals appear to have tunneled downwards, extending the bottom of the tube. Mirabilite crystals were rarely observed within smaller brine pockets, presumably because crystals in the smaller pockets were too small to resolve. The dimensions of the larger crystals can be estimated from the photographs. For example, the largest crystal in Fig. 4.7(b) has a diameter of 140 μm while the smallest measured diameter was 15 μm. These crystals tend to have rounded edges and irregular shape. Light (1995) inferred an effective crystal size of 9 μm for

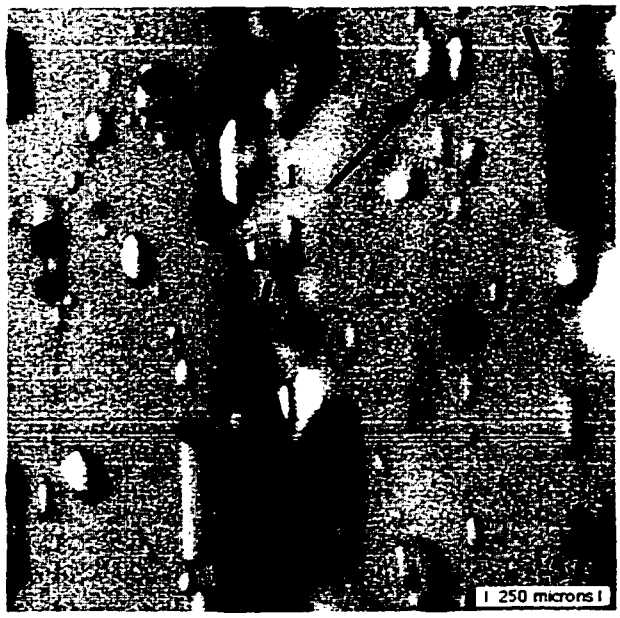

Figure 4.6. Image showing examples of vapor bubbles within brine pockets at –5 °C. Note that the bubble positions in the brine pockets vary. Arrows indicate (1) spherical bubbles within pockets and (2) a non-spherical bubble in a tube. The magnification is 56.

mirabilite. This supports the observation that crystals in most of these pockets are too small to be resolved.

4.4 Temperature-Dependent Changes

Although we can estimate scattering coefficients for first-year sea ice from the observations of the number and size distributions of brine, gas, and salt inclusions at –15 °C, a general model requires information about how the microstructure evolves with temperature. Specifically, we need data on temperature-dependent changes in inclusion sizes and number densities.

Based on the laws of freezing equilibrium, we expect certain physical changes to occur when the temperature of the ice is changed. When cooled, brine pockets and vapor bubbles shrink, mirabilite begins to precipitate at –8.2 °C while hydrohalite

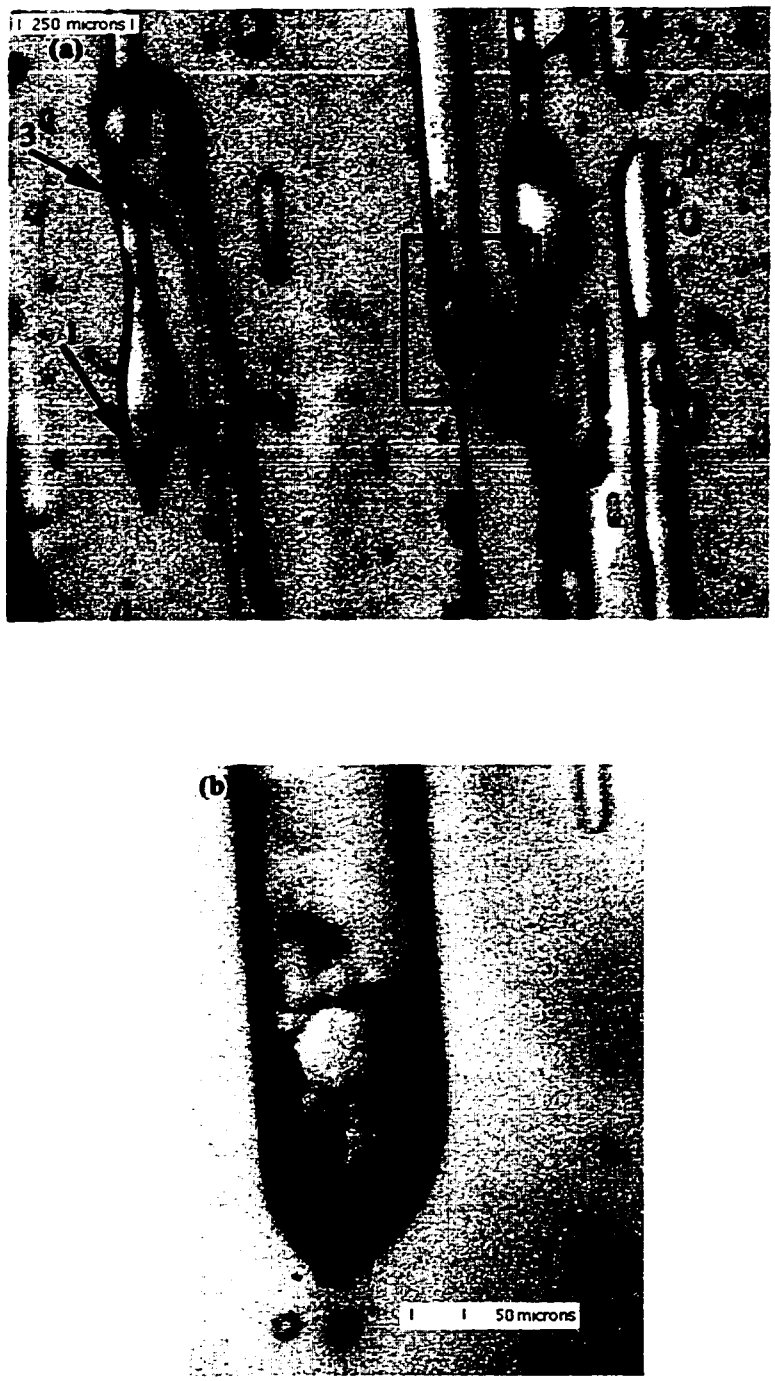

Figure 4.7. Image showing examples of precipitated mirabilite crystals within brine tubes. Image (a) shows a scene 1.9 by 1.4 mm, (b) is magnified image of boxed area. The arrows in (a) show crystals (1) gathered at the base of a tube, (2) strewn throughout a tube, and (3) stuck in a narrow part of a tube. The largest and smallest crystals identified in (b) have diameters 140 and 15 μm, respectively. The magnifications are 56 and 205 for (a) and (b) respectively.

($NaCl \cdot 2H_2O$) begins to precipitate at –22.9 °C. When warmed, brine pockets and vapor bubbles enlarge, and all precipitated salts gradually dissolve. Interactions between these inclusions are expected to play an important role in how the inherent optical properties of the ice respond to changes in the temperature. To investigate these changes, a series of images were recorded as the temperature of the ice was changed. While the size of brine and vapor inclusions in thin sections adjusts to changes in temperature very rapidly (order of minutes), we do not know how quickly the salt precipitation and dissolution occurs. Preliminary tests (D. Erickson, personal communication, 1992) suggested that precipitation and dissolution do not happen instantaneously, but require a period of time (order of hours) to come to equilibrium. For this reason, samples were held at each temperature for a minimum of 24 hours before photographs were taken.

4.4.1 Cooling Sequence

Figure 4.8 shows structural changes in a sample of ice with three large brine tubes and numerous brine pockets as it was cooled from (a) –15 to (b) –20 to (c) –25 °C. The three images on the right side of the figure show close-up views of the boxed areas in the images on the left. At –15 °C, two of the tubes contain vapor bubbles (arrows 1 and 2), as do several of the smaller inclusions. The tube in the center of the image contains several large crystals of mirabilite that have settled on the top of a vapor bubble (arrow 3).

Several noticeable changes took place when the sample was cooled to –20 °C. First, each of the tubes, pockets, and vapor bubbles was reduced in size. The vapor bubble in one of the ellipsoidal inclusions between the two tubes on the right vanished completely while the mirabilite crystals increased in size and number. A group of mirabilite crystals also precipitated below the vapor bubble in the center tube (arrow 4). Note that the ice-brine refractive boundaries have become more distinct as the refractive index of

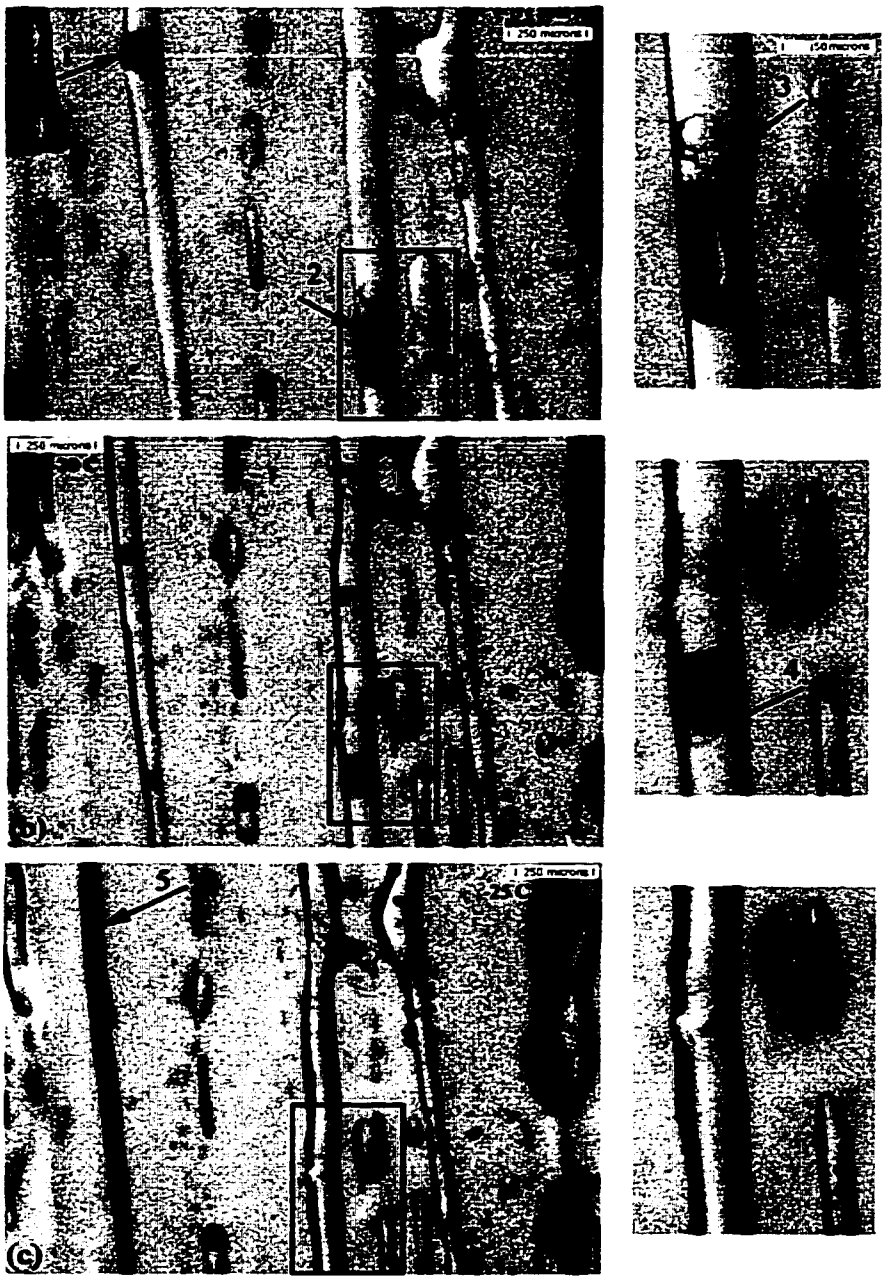

Figure 4.8. Sequence showing changes in microstructure as the ice is cooled from (a) –15 °C to (b) –20 °C to (c) –25 °C. The images on the right are high magnification views of the boxed areas in the larger images on the left. Brine tubes, pockets, vapor bubbles, and mirabilite crystals are observed to undergo significant evolution as the temperature changes. Arrows indicate (1), (2) vapor bubbles within tubes, and (3), (4) mirabilite crystals. Arrow (5) shows the only tube that has clearly filled with hydrohalite. The magnification is 38 for the images on the left and 76 for the images on the right.

the brine increases from 1.370 at –15 °C to 1.379 at –20 °C. This makes the outlines of brine inclusions more distinct and the outlines of the mirabilite crystals (n = 1.396) less distinct.

At –25 °C, brine inclusions and vapor bubbles have continued to shrink and some vapor bubbles have disappeared altogether. The brine tube on the left of Fig. 4.8 (c) appears entirely opaque (arrow 5). This is almost certainly due to the formation of hydrohalite crystals. Laboratory experiments (Maykut and Light, 1995) suggest that hydrohalite and ice frequently form a closely knit crystalline compound. Unlike mirabilite, which appears to always remain separate from the ice, hydrohalite becomes intimately associated with the ice lattice. This apparently results in brine inclusions that are filled with an ice-hydrohalite slush. The formation of this slush was only occasionally observed in tubes and was never observed to occur in smaller, isolated brine pockets. The mirabilite crystals at –25 °C are about the same size as they were at –20 °C, as few additional sulfate ions remain in solution to precipitate at temperatures below –20 °C. The refractive index of the brine has further increased giving even more definition to the brine inclusions in ice and even less contrast to the mirabilite crystals in brine. Brine inclusions were occasionally observed to become more angular as the ice was cooled through the hydrohalite regime, suggesting the possibility that precipitating hydrohalite crystals nucleate on the walls of the inclusions and are incorporated into the ice.

4.4.2 Warming Sequence

The sequence of four images in Fig 4.9 shows the response of a group of brine pockets as the temperature increased from (a) –13 to (b) –8 to (c) –4 °C, and then decreased to (d) –13 °C. Initially the four large inclusions were separate, having an average aspect ratio of 1.7, and sizes varying between 100 and 200 μm in length (bins 4

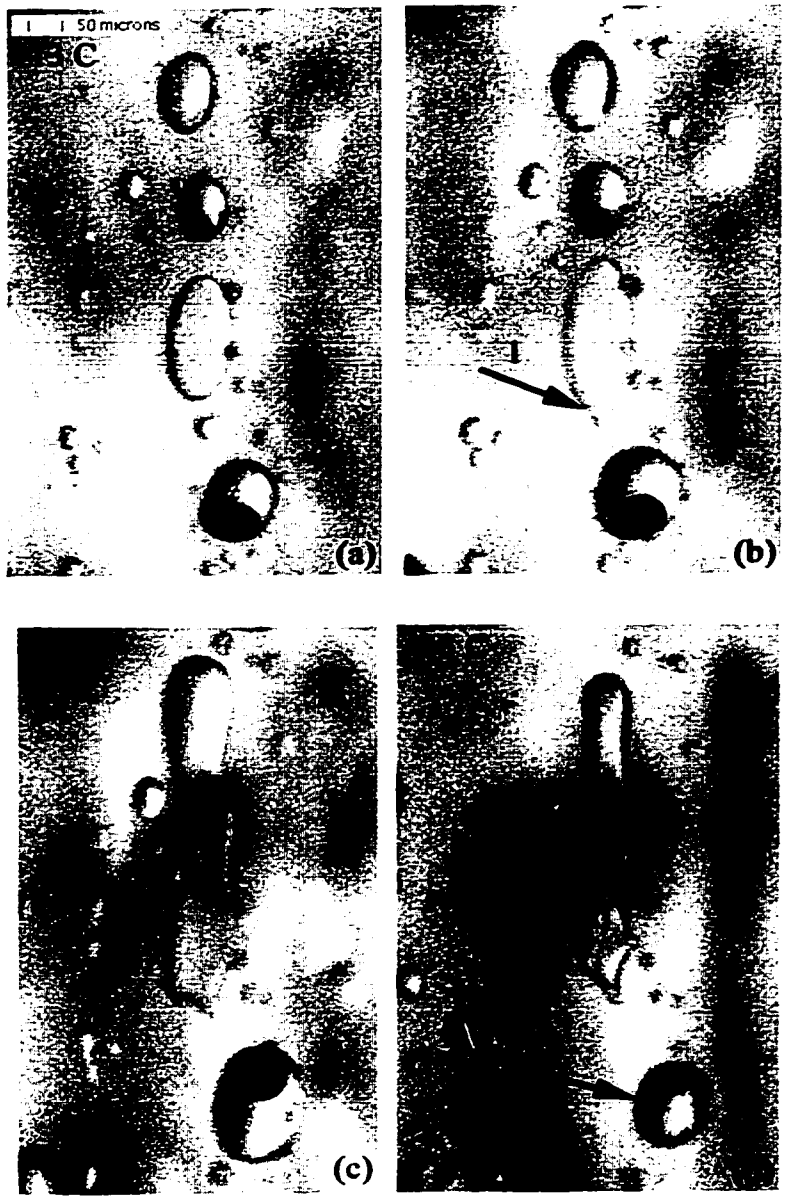

Figure 4.9. Warming sequence showing changes in ice structure at (a) –13 °C, (b) –8 °C, and (c) –4 °C. Note enlargement and merging of the 3 brine pockets in the center of the image. The sample was then cooled to (d) –13 °C. Arrows indicate (1) merged inclusions, and (2) an isolated pocket with reversible changes. Hysteresis is evident as the large inclusion in (d) remains merged after it has again cooled. The magnification is 80.

and 5 in our size distribution). Two of the inclusions contained vapor bubbles. As the temperature increased from –13 to –8 °C, both the brine and vapor inclusions increased in size. No new vapor bubbles formed. The third inclusion from the top merged with a small inclusion below it, producing a single inclusion of irregular shape (arrow 1). When the sample was warmed to – 4 °C, three of the four inclusions merged to form a single inclusion of aspect ratio 6. In this particular scene, the vertical anisotropy of the structure became more pronounced as it warmed. As these inclusions enlarged, their total surface area and scattering cross-section increased. However, this increase is somewhat offset by the reduction in surface area and scattering cross sections that occurred when the inclusions merged.

When the sample was again cooled to –13 °C, the vapor bubble in the newly merged inclusion disappeared, while the merged inclusion remained intact. No mirabilite crystals were visible in either image at –13 °C. The pocket at the bottom of the image (arrow 2) underwent changes that are likely reversible, whereas the other three underwent changes that do not appear to be immediately reversible. Grenfell (1983) suggests that inclusions of large aspect ratio should divide up into smaller inclusions when cooled, but this did not happen during the four days in which these observations were made. We observed many other such merged features that also did not break up into smaller inclusions when cooled. These observations do not rule out the possibility that irregular, high aspect ratio inclusions may evolve into multiple pockets, but such evolution would be controlled by diffusive processes in the pocket and the time constant would be greater than a few days. In fact, Cole and Shapiro (1998) suggest that high-aspect ratio brine inclusions require an entire annual cycle to evolve into smaller, more spherical inclusions.

The image in Fig. 4.10 shows an example of structural changes that occur in first-year ice during warming. Note that this image has relatively low magnification (total volume = 9.7 mm^3), so it shows many more inclusions than were visible in the cooling sequence (Fig. 4.8). Images are shown for –15, –5 and –2 °C. At –15 °C the inclusions

Figure 4.10. Sequence of images showing first-year congelation microstructure as it warms to near melting. The images were taken at (a) –15, (b) –5, and (c) –2 °C. All inclusions enlarge and shapes evolve to being more plump, rounded. Image width is 3.5 mm and the magnification is 24.

are distinct and separated, but as the sample warms, inclusions of both brine and vapor increase in size, become plump and rounded, and many begin to merge. The effect of the warming on this scene is that inclusions of brine and vapor grow larger, yet decrease in number. As the temperature increased from –15 to –5 °C the brine pocket and vapor bubble number densities decreased from 51 per mm^3 to 46 per mm^3 and 5.4 per mm^3 to 4.7 per mm^3 respectively (reduced to 90% and 87% respectively). As the temperature increased from –5 to –2 °C these values further decreased to 35 per mm^3 (69% of the value at –15 °C) and 2.7 per mm^3 (50% of the value at –15 °C) for brine pockets and vapor bubbles respectively. The number densities in this scene are considerably larger than they would be for a scene with larger area that includes clear areas where few inclusions exist. We believe the processes that occur in this scene are typical of warm sea ice and may be key to understanding structural-optical relationships in sea ice.

The images in Fig. 4.11 show structural changes in a sample of first-year ice that is warmed from –14 to –3 °C, then cooled to –30 °C, and finally warmed again to –5 °C. The bottom of a single tube is clearly visible (arrow 1) in this scene, along with several smaller brine inclusions. At –14 °C, precipitated mirabilite crystals can be seen at the bottom of the tube (arrow 2). At –9 °C the crystals are smaller, the tube is wider, and the brine pocket in the upper left corner (arrow 3) has increased in size. At –3 °C, the tube has increased further in diameter and all of the mirabilite has dissolved. A vapor bubble has formed within the pocket in the upper left hand corner (arrow 4). Also, the pocket near the center of the image (arrow 5) has merged with a smaller pocket containing a vapor bubble. When the sample is cooled back to –14 °C, there is no evidence of mirabilite precipitation. The vapor bubble in the pocket on the left has also disappeared (arrow 6). At –30 °C there is still no observable mirabilite or hydrohalite in the image. The brine tube forms a vapor bubble (arrow 7) as the temperature increases to –5 °C. Unfortunately it is not possible to tell whether a vapor bubble reformed in the pocket on the left (arrow 8). As in other images, the majority of precipitated salt

Figure 4. 11. Sequence of six images showing microstructure as it warmed from –14 to –9 to –3 °C, subsequently cooled to –14 and –30 °C, and finally warmed to –5 °C. Arrows indicate (1) the bottom of a large tube containing (2) mirabilite crystals, (3) an isolated brine pocket, (4), a newly formed vapor bubble, (5) merging, (6) a brine pocket with disappearing vapor bubble, (7) a vapor bubble that has formed in a tube, and (8) a pocket that may not have formed a bubble when warmed. The brine tube on the right is observed to dissolve its precipitated mirabilite crystals, enlarge, then shrink again without reprecipitating crystals. This is an example of the hysteresis that is observed to occur in sea ice. The magnification is 56.

crystals are too small to resolve. The larger crystals have likely coarsened over time, but represent a small fraction of the total number of crystals actually present.

4.4.3 Modeling Inclusion Enlargement and Merging

To formulate a realistic temperature-dependent structural-optical model, we need data on how inclusions enlarge and merge. Enlarging rates determine how the scattering cross-section for each class of inclusion changes with temperature, and merging rates determine how the inclusion number densities change with temperature. To estimate these rates for brine pockets, we will first assume freezing equilibrium, so isolated brine pockets increase in volume at the same rate as the bulk brine volume. We will also assume that as a pocket increases in size it maintains its original aspect ratio. To estimate the enlarging rate for vapor bubbles, we will assume that bubbles existing at −15 °C enlarge as the temperature increases, but that no new vapor bubbles form. Although the rate of enlargement for a vapor bubble depends on the size of the brine inclusion housing the bubble, we will assume that vapor bubbles and brine pockets enlarge independently.

We tested these assumptions by analyzing several inclusions as they warmed from −15 to −5 °C. On average, the volume of the brine pockets increased at approximately the rate specified by the freezing equilibrium relations. The average aspect ratio of the pockets increased slightly from 2.5 to 2.8 over the 10 °C temperature change. This suggests that pockets grow taller faster than they grow wider. Since it was not possible to find a brine tube that did not merge with neighboring smaller brine inclusions, it was not feasible to estimate the rate of brine tube enlargement due to warming alone.

In this scene, the bubbles that existed at −15 °C grew in size as the temperature increased, but no new vapor bubbles formed between −15 and −5 °C. This observation is counter-intuitive to what we expected. One possible explanation is that the brine inclusions are not isolated, but are interconnected by a network of very small cracks in the ice. If this were the case, it is possible that as a brine inclusion warms it draws brine

out of the cracks to fill the expanding volume. Given the large uncertainty in estimating small volumes from two dimensional images, it is unclear whether the bubbles grew at the rate predicted by the freezing equilibrium relations, but our estimates suggest that they grew slightly faster than predicted. If brine inclusions are actually interconnected, then it is possible that existing vapor bubbles grow in response to the net volume created by more than one brine inclusion.

The merging of brine inclusions depends strongly on the local geometry. Tightly packed inclusions began to merge at moderate temperatures (< -8 °C), but more widely-spaced inclusions did not begin to merge until the sample was almost completely melted. Three separate scenes were analyzed for inclusion number density decreases between –15, –10, and –5 °C. One scene contained mostly clustered pockets, another contained more widely spaced inclusions, and the third contained a brine tube and numerous small pockets near the tube perimeter. These scenes were selected because they spanned the range of observed number densities. We did not, however, attempt to record the actual number densities or how the size distributions in these three scenes evolved. Rather, we were interested in getting an idea of the minimum and maximum merging rates appropriate for interior first-year sea ice. We express these merging rates as the percentage of inclusions observed at –15 °C that remain at any given temperature. When the temperature was increased from –15 to –10 °C, between 71% and 100% of the inclusions remained unmerged in the tightly packed and widely spaced samples, respectively. When the temperature was then increased to –5 °C, 50 - 76% of the original inclusions remained unmerged in the same two scenes. At –2 °C, the scene with the highest number density retained 69% of its inclusions. These values are extremes, but they will serve as guidance in developing merging rates in the structural-optical model. We did not estimate the rates with which bubbles merged, but rather assumed that since only about an average of 4% of the inclusions contained vapor bubbles, that on average bubble number densities do not significantly decrease. In the

few cases where two inclusions with vapor bubbles did merge, the bubbles were observed to merge quickly once the parent inclusions merged.

4.5 Summary

In this chapter we have presented observations of sea ice microstructure in vertical thin section samples using a high resolution imaging system. With this imaging system, we clearly resolved brine tubes, brine pockets, vapor bubbles, and precipitated salt crystals in the samples. The use of vertical sections provides a new view of the ice microstructure. In contrast to information gathered from horizontal samples, we see a striking vertical alignment of the microstructure, and can distinguish between elongated tubes and ellipsoidal pockets of brine. By viewing vertical sections, we have also observed considerable inhomogeneity in the ice structure. There are large areas free of inclusions, and areas where the inclusions are tightly clustered. These spatial inhomogeneities affect how inclusions interact as the ice warms. Furthermore, this higher resolution view has revealed valuable information about the numerous small-scale inclusions which we expect to be important in formulating a general structural-optical model.

We first collected data necessary to initialize our model by recording number densities and size distributions for brine inclusions and vapor bubbles at –15 °C. We observed average brine inclusion number densities approximately 7 – 10 times larger than had been previously documented. Because we were able to distinguish between tubes and pockets in these observations, we found that a majority of the total brine volume resides in tubes. Despite these improved inclusion number density estimates, we were only able to account for 52% of the predicted brine volume. We suspect that the inhomogeneity of the microstructure creates areas with large brine volume that remain unsampled, as they are optically denser and would be difficult to image. Furthermore, we have identified a variety of inclusion shapes. Few natural brine inclusions are spherical, and we have only limited resources with which to treat scattering for a population of vertically aligned tubes. While a majority of the total

brine resides in the brine tubes, we expect the brine pockets to play an important role in light scattering, as they have larger surface area per unit volume than the tubes.

Number densities and size distributions for vapor bubbles were also documented. The observed number density was an order of magnitude larger than previously documented, yet, only approximately 4% of brine inclusions contained vapor bubbles in our observations at –15 °C. The observed bubbles were also approximately an order of magnitude smaller than those previously reported. Earlier measurements were taken on ice from a freezing lead, which should have fundamentally different gas inclusions. We are not aware of any other measurements of vapor bubbles in interior ice.

We observed occasional precipitated salt crystals within brine inclusions, however, most of the salt mass predicted by phase relations was not visible. This observation is consistent with the small effective crystal sizes (< 10 μm) inferred by Light (1995). If these estimates are realistic, then only a fraction of the crystals present should be large enough to be visible with this imaging system. As the ice cooled into the hydrohalite regime, occasional brine tubes were observed to form an optically-thick slush. We believe this slush is a network of ice and precipitated hydrohalite and may only occur in inclusions large enough to support convective processes. Also, our observations suggest that in smaller inclusions, hydrohalite crystals remain small and nucleate along inclusion walls.

As the ice warmed, we verified that inclusions of brine increased in size roughly as predicted by phase equilibrium. We examined several scenes that exhibited a range of brine pocket merging rates as the ice warmed. In these scenes, between 50% and 76% of the brine inclusions initially present at –15 °C remained at –5 °C. Due to sample inhomogeneity, however, we believe the standard deviations of these merging rates to be very large.

While existing vapor bubbles were commonly observed to vanish when cooled, new vapor bubbles were infrequently observed to form during warming. This observation suggests that we do not yet completely understand the processes that occur as the ice

warms. It is possible that as a brine inclusion enlarges, the work required to overcome the surface energy associated with the creation of a vapor bubble is large enough that the bubble does not immediately nucleate. It is also possible that neighboring brine inclusions may be in hydraulic contact through a network of small cracks in the ice. If these cracks formed as a result of the growing pressure within brine inclusions during cooling, they would likely nucleate at the surface of individual inclusions (Picu et al., 1994). Because such a network would permit brine to flow between inclusions, several inclusions could share a single vapor bubble. As the inclusions grow in size, a single bubble could assume the excess volume created by the entire neighborhood of brine inclusions. Light scattering from such cracks could also play an important role in understanding the optical properties of the ice.

Finally, we observed obvious temperature-dependent changes in the optical contrast of brine inclusions in ice. As the temperature lowered, brine inclusions became more distinct and their boundaries had increasing contrast and definition. As the ice warmed, inclusion boundaries became less distinct. This is a direct result of the temperature-dependent refractive index of brine in equilibrium with ice (Maykut and Light, 1995) and is expected to affect scattering by brine inclusions.

CHAPTER FIVE
MODELING RADIATIVE TRANSFER IN A CYLINDRICAL DOMAIN

To study structural-optical relationships in sea ice, we need to be able to derive inherent optical properties (IOPs) of the ice from observations of its apparent optical properties (AOPs). This requires a suitable radiative transfer model. This radiative transfer model must simulate the domain geometry, boundary conditions, and incident light field appropriate for the observational conditions. Because our laboratory observations are carried out using cylindrical core samples, and not horizontally infinite slabs, we need a radiative transfer model valid for a cylindrical domain.

Available radiative transfer models exploiting techniques such as invariant imbedding (Mobley, 1989), the discrete ordinates method (Grenfell, 1983, 1991; Jin et al., 1994), and the finite element method (Bulgarelli et al., 1999) are limited to plane-parallel geometries with horizontally infinite domains. Earlier observational work (Light, 1995) used core samples wrapped in reflective Mylar in an attempt to simulate an infinite horizontal domain. Analysis of the optical properties of these horizontally-finite samples using a one-dimensional horizontally-infinite model proved difficult because the Mylar was not a perfect reflector and the transmission through the side walls was found to be significant and difficult to quantify. For this reason, we have developed a radiative transfer model specifically for the purpose of analyzing radiometric observations from three-dimensional, multiply scattering domains with azimuthal symmetry.

5.1 Approach

Monte Carlo radiative transfer models are well-suited for describing complex geometries and have been used successfully for a variety of non plane-parallel geometries and non-standard illumination cases in sea ice and ocean water. Trodahl et al. (1987, 1989) developed a Monte Carlo model for analyzing beamspread measurements made within sea ice. Mobley (1996) formulated a Monte Carlo model to

simulate the radiation field around a spherical point source in the ocean. While other Monte Carlo models have been built for specific domains (e.g., Plass and Kattawar, 1972; Gordon and Brown, 1973; and Morel and Gentili, 1991), none are designed to treat radiative transfer specifically within a cylindrical domain.

Solution to the radiative transfer equation using Monte Carlo techniques is accomplished by calculating the paths of a large number of photons. In the simplest models, photons are emitted from the incident source and enter the top of the model domain. They travel distances calculated by the probabilities of scattering and absorption between interactions with the medium. Both scattering and absorption processes are discretized, and photons encounter scattering or absorption events based on the relative magnitudes of their probabilities. If an interaction is determined to be a scattering event, a scattering angle is calculated by sampling the phase function and the direction of the emergent photon trajectory is changed accordingly. The trajectory is continued until the photon exits the domain, is absorbed, or is incident upon a simulated detector, at which time the next photon is introduced into the domain. Basic radiometric quantities are computed from information about the number of photons incident on the domain and the sum of all photons reaching a detector. Since photons are released at the location of the incident illumination, this type of model is known as a forward model.

When few of the incident photons reach the detector, forward models can become very inefficient. To solve this problem, backward Monte Carlo methods have been developed (Collins et al., 1972; Adams and Kattawar, 1978; Gordon, 1985). Backward models are based on principles of reciprocity and require solution to the adjoint, or time-reversal, problem. In the adjoint problem, photons are generated at the detector and their trajectories traced back to the original source. Photons are tallied as they leave the domain heading upwards and every photon generated contributes to the solution.

5.2 Solution of the Adjoint Problem

The backward Monte Carlo method solves the adjoint problem through use of a reciprocity relation. In this section we construct a reciprocity relation for an upward-looking irradiance detector below a non-refractive domain and show how it can be evaluated by following the trajectories of numerous photons. We will follow the notation and guidance of Gordon (1985) and Mobley (1994) in this derivation.

Problems such as radiative transfer and neutron diffusion are governed by the transport equation:

$$(\xi \cdot \nabla)L(\boldsymbol{r},\xi) + k(\boldsymbol{r})L(\boldsymbol{r},\xi) = \int_{\Omega'} \beta(\boldsymbol{r},\xi' \rightarrow \xi)L(\boldsymbol{r},\xi')d\Omega(\xi') + Q(\boldsymbol{r},\xi), \qquad (5.1)$$

where the radiance $L(\boldsymbol{r}, \xi)$ is specified at vector location $\boldsymbol{r}$ in the direction of unit vector ξ. The integral is evaluated over solid angle, Ω. The volume scattering function $\beta(\boldsymbol{r}, \xi' \rightarrow \xi)$ describes the fraction of scattering from the direction ξ' into the direction ξ at location $\boldsymbol{r}$, and $\sigma(\boldsymbol{r}) \equiv \int_{\Omega} \beta(\boldsymbol{r},\xi' \rightarrow \xi)d\Omega(\xi')$. The beam attenuation coefficient, $k(\boldsymbol{r})$, is the sum of the absorption coefficient, $\kappa(\boldsymbol{r})$, and scattering coefficient, $\sigma(\boldsymbol{r})$. $Q(\boldsymbol{r}, \xi)$ is the intensity (power per unit solid angle) per unit volume of all sources at $\boldsymbol{r}$ in the direction ξ. It can be shown (Case and Zweifel, 1967) that for a closed convex volume V bounded by a surface S, with single scattering albedo $\varpi_o \equiv \sigma(\boldsymbol{r})/k(\boldsymbol{r}) < 1$, Eqn 5.1 possesses unique solutions given the sources within V, the radiance incident on S from the outside, and the IOPs of the domain.

For a domain with volume V and surface S, Fig 5.1 (a) illustrates the forward problem and Fig. 5.1 (b) shows the corresponding adjoint problem. In this illustration, S encloses the entire volume, and incident radiation is constrained to fall on the top surface of S. Points lying on this top surface are denoted by $\boldsymbol{r} = \boldsymbol{r}_o$, points at the location of the detector by $\boldsymbol{r} = \boldsymbol{r}_d$. The radiance incident on S is $L_1(\boldsymbol{r}_o, \xi)$, and is defined for $\xi \cdot \boldsymbol{u} < 0$, where $\boldsymbol{u}$ is the outward normal of S.

In the forward problem, $L_1(\boldsymbol{r}, \xi)$ is the solution of Eqn. 5.1 for source $Q_1(\boldsymbol{r}, \xi) = 0$ and incident radiance $L_1(\boldsymbol{r}_o, \xi)$. In the adjoint problem (Fig. 5.1b), $L_2(\boldsymbol{r}, \xi)$ is the

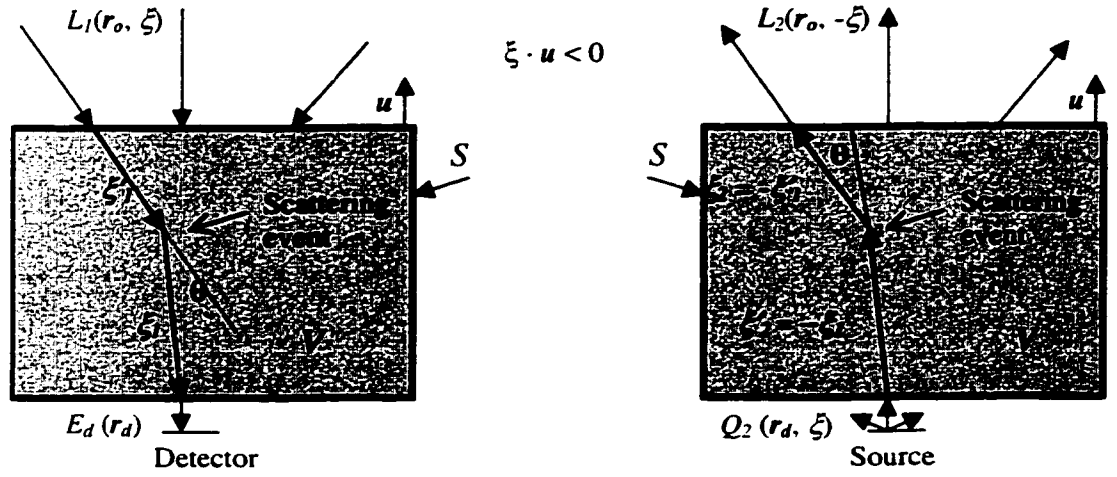

Figure 5.1. Schematic of (a) forward and (b) adjoint radiative transfer problems used to formulate the backward Monte Carlo model (adapted from Mobley, 1994). The domain is specified by volume V and surface S. The unit vector normal to the top surface of S is $\boldsymbol{u}$, and $\boldsymbol{\xi}$ is a unit vector in the direction of a photon trajectory. The vector locations at the surface and at the bottom are denoted by $\boldsymbol{r}_o$ and $\boldsymbol{r}_d$, respectively. Radiances are denoted by L, downwelling irradiance by E_d, and sources by $Q(\boldsymbol{r}, \boldsymbol{\xi})$. Scattering angle is denoted θ.

solution for source $Q_2(\boldsymbol{r}, \boldsymbol{\xi})$ and incident radiance $L_2(\boldsymbol{r}_o, \boldsymbol{\xi})$. If the volume scattering function is time reversal invariant, i.e., if $\beta(\boldsymbol{r}, \boldsymbol{\xi}' \rightarrow \boldsymbol{\xi}) = \beta(\boldsymbol{r}, -\boldsymbol{\xi} \rightarrow -\boldsymbol{\xi}')$, the following reciprocity relationship holds (Case, 1957):

$$\int_{\xi \cdot u < 0} d\Omega \int_S dS |\xi \cdot u| \left[L_1(\boldsymbol{r}_o, \xi) L_2(\boldsymbol{r}_o, -\xi) - L_2(\boldsymbol{r}_o, \xi) L_1(\boldsymbol{r}_o, -\xi) \right]$$

$$= \int_{4\pi} d\Omega \int_V dV \left[L_1(\boldsymbol{r}, -\xi) Q_2(\boldsymbol{r}, \xi) - L_2(\boldsymbol{r}, \xi) Q_1(\boldsymbol{r}, -\xi) \right] \qquad (5.2)$$

where $\boldsymbol{\xi} \cdot \boldsymbol{u} < 0$ on the integral indicates that the Ω integration is to be carried out only for downwelling directions and $L_1(\boldsymbol{r}_o, -\boldsymbol{\xi})$ and $L_2(\boldsymbol{r}_o, -\boldsymbol{\xi})$ are the radiances leaving the domain in the forward and adjoint problems, respectively. This equation relates the forward (subscript 1) and adjoint (subscript 2) radiative transfer problems associated with a domain for a particular set of IOPs and boundary conditions.

To illustrate how Eqn. 5.2 is solved, we next compute the downwelling irradiance at the detector, $E_d(r_d)$, where

$$E_d(r_d) = \int_{\xi \cdot u < 0} L_1(r_d, \xi)\, |\xi \cdot u|\, d\Omega, \tag{5.3}$$

and the detector normal is in the direction of u. If the incident downwelling radiance is a constant, L_o, weighted by an angular dependence, $C(\xi)$, and there are no internal sources in the original problem, then $L_1(r_o, \xi) = L_o\, C(\xi)$ and $Q_1(r, -\xi) = 0$.

To solve the adjoint problem, we must choose a function for $Q_2(r, \xi)$ that will produce the desired integral on the right hand side of Eqn. 5.2. To extract the downwelling irradiance, $E_d(r_d)$, we design a function for Q that broadcasts photons in the pattern that our detector would detect photons. Thus, we choose $Q_2(r, \xi)$ to be

$$\begin{array}{ll} (\xi \cdot u)\, J_o\, \delta(r - r_d) & \text{for } \xi \cdot u > 0 \\ 0 & \text{for } \xi \cdot u \le 0 \end{array} \tag{5.4}$$

where J_o is a positive constant equal to the number of photons released at the detector. In this discussion, we make reference only to a downwelling irradiance detector, however detectors to monitor upwelling irradiance, scalar irradiance, and radiance are also available, and Table 5.1 gives the form of $Q_2(r, \xi)$ required to simulate these other detectors.

Table 5.1. Values of $Q_2(r, \xi)$ required to model different types of detectors in Eqn. 5.2, after Gordon (1985).

Detector	Quantity measured at detector	$Q_2(r, \xi)$
downwelling irradiance	$E_d(r_d) = \int_{\xi \cdot u < 0} L_1(r_d, \xi)\, \lvert\xi \cdot u\rvert\, d\Omega$	$(\xi \cdot u)\, J_o\, \delta(r - r_d)$ for $\xi \cdot u > 0$ 0 for $\xi \cdot u \le 0$
upwelling irradiance	$E_u(r_d) = \int_{\xi \cdot u > 0} L_1(r_d, \xi) \lvert\xi \cdot u\rvert\, d\Omega$	0 for $\xi \cdot u \ge 0$ $\lvert\xi \cdot u\rvert\, J_o\, \delta(r - r_d)$ for $\xi \cdot u < 0$
scalar irradiance	$E_o(r_d) = \int_{\Omega} L_1(r_d, \xi) d\Omega$	$J_o\, \delta(r - r_d)$ for all $\xi \cdot u$
radiance in direction ξ'	$L(r_d, \xi')$	$J_o\, \delta(r - r_d)\, \delta(\xi - \xi')$

As no radiance is incident on S in the adjoint problem, $L_2(\boldsymbol{r}_o, \boldsymbol{\xi}) = 0$, and Eqn. 5.2 reduces to

$$L_o \int_S dS \int_{\boldsymbol{\xi}\cdot\boldsymbol{u}<0} d\Omega \,|\boldsymbol{\xi}\cdot\boldsymbol{u}|\, C(\boldsymbol{\xi})\, L_2(\boldsymbol{r}_o, -\boldsymbol{\xi}) = J_o E_d(\boldsymbol{r}_d)\,. \tag{5.5}$$

Since $L_2(\boldsymbol{r}_o, -\boldsymbol{\xi})$ is the radiance leaving S in the adjoint problem, counting photons as they leave the domain will give us something very close to the desired $L_2(\boldsymbol{r}_o, -\boldsymbol{\xi})$. It is useful to define a quantity similar in form to the total upwelling irradiance at the surface of the adjoint problem. We thus define $E_{u2}(\boldsymbol{r}_o)$ as,

$$E_{u2}(\boldsymbol{r}_o) \equiv \int_{\boldsymbol{\xi}\cdot\boldsymbol{u}<0} d\Omega(\boldsymbol{\xi})\,|\boldsymbol{\xi}\cdot\boldsymbol{u}|\, C(\boldsymbol{\xi}) L_2(\boldsymbol{r}_o, -\boldsymbol{\xi})\,.$$

$E_{u2}(\boldsymbol{r}_o)$ is similar in form to the adjoint upwelling irradiance just above the surface, but it also contains the weighting factor $C(\boldsymbol{\xi})$. The quantity $E_{u2}(\boldsymbol{r}_o)$ is easily computed by tallying the photons that leave the top of the domain and weighting them by $|\boldsymbol{\xi}\cdot\boldsymbol{u}|$ and $C(\boldsymbol{\xi})$. Equation 5.5 becomes

$$L_o \int_S dS\; E_{u2}(\boldsymbol{r}_o) = J_o E_d(\boldsymbol{r}_d)\,. \tag{5.6}$$

Equation 5.6 relates the desired quantity $E_d(\boldsymbol{r}_d)$ in the forward problem to known or computable quantities in the adjoint problem. If $C(\boldsymbol{\xi}) = 1$, as it does for isotropic radiation, then the downwelling irradiance at the surface is given by

$$E_d(\boldsymbol{r}_o) = \int_\Omega L_1(\boldsymbol{r}_o, \boldsymbol{\xi}) = \int_\Omega L_o C(\boldsymbol{\xi})\, d\Omega = \pi L_o\,.$$

From Eqn. 5.4, the total power P_2 emitted by the adjoint source is

$$P_2 = \int_{4\pi} d\Omega(\boldsymbol{\xi}) \int_V dV\; Q_2(\boldsymbol{r}, \boldsymbol{\xi}) = \pi J_o\,, \tag{5.7}$$

and Eqn. 5.6 becomes

$$\frac{E_d(\boldsymbol{r}_d)}{E_d(\boldsymbol{r}_o)} = \frac{1}{P_2} \int_S dS\; E_{u2}(\boldsymbol{r}_o)\,. \tag{5.8}$$

The ratio of the irradiance at the detector to the irradiance incident on the domain surface in the forward problem (left hand side of Eqn. 5.8) is proportional to the ratio of

the power leaving the source (the integral in 5.8) to the power emitted by an embedded source in the adjoint problem (P_2). This is the desired result for diffuse incident illumination, and enables us to compute the irradiance at the location of the detector simply by computing the power associated with photons leaving the top surface of the domain (2π times the number of photons incident on the top surface of S) and comparing it to the power associated with photons leaving the adjoint source (πJ_o, where J_o is the number of photons released from the detector). If the incident irradiance is not isotropic, then the value used to compute the power leaving the top surface of S must also be multiplied by $C(\xi)$.

5.3. Implementation

The code for this model was written in FORTRAN 90 using Digital Equipment Corp. Visual Fortran version 6.0 and was run on a personal computer. The model domain is defined by specifying the height and radius of the cylindrical sample. Vertical variations in optical properties are modeled using horizontal layers, each with specified thickness and constant optical properties. The refractive index (n), $\kappa(\lambda)$, σ, and phase function ($p[\theta]$), must be specified for each layer. The model can treat material with phase functions described by either a Henyey-Greenstein analytic function (Henyey and Greenstein, 1941), or by tabulated points calculated from Mie scattering theory or other detailed formulations. The phase function is assumed to have azimuthal symmetry, an appropriate assumption for spherical and vertically oriented cylindrical scatterers.

Radiation incident on the upper surface of the model cylinder can be either collimated or diffuse. Because of the complexities associated with computing non-normal spectral reflections inside a cylinder with multiple refractive layers and because the model was designed to simulate the laboratory observations, the collimated radiation is assumed to be normally incident on the top of the cylinder.

The detector may be chosen to record either radiance or irradiance. It can be located anywhere in or on the domain and it can view any direction. In the case of a radiance

the direction of the detector axis. The half angle of the acceptance cone can vary between 0 (detects radiance only along the viewing axis) and $\pi/2$ radians (detects radiance from the entire hemisphere).

5.3.1 Photon Release

Photons are released at the detector. It is convenient to think of each photon as representing a packet of photons. The number of photons in the packet (or the intensity of the associated beam) is characterized throughout each packet trajectory by a statistical weight (W). Initially, each packet is assigned a W of unity. By appropriately scaling W, the actual number of photons surviving in the packet can be modified to reflect the portion of the packet that is not absorbed. The initial position (radius [ρ], height [z], and azimuth [ϕ]) of each packet is assigned to that of the detector. The direction of the packet trajectory is defined by a polar angle (θ) and azimuth angle (χ). The detector hemisphere is divided into a user-specified number of bins with equal solid-angle. θ and χ are initialized with the central polar and azimuth angles of the detector bin from which the packet is released. For irradiance detectors, all bins in the hemisphere are active and equal numbers of photons are released from each. If a radiance detector is implemented, then only bins within the angular acceptance angle of the viewing direction are active.

Because the domain is permitted to have multiple refractive layers, photon trajectories and statistical weights obey Snell's law whenever they interact with a refractive boundary. As photon statistical weights represent radiances along the direction ξ, W for photon packets crossing a boundary with relative refractive index (m) must be modified to conserve energy:

$$W' = W \frac{1}{m^2} \cdot t(\xi, m)$$

where $t(\xi, m)$ is the Fresnel transmission coefficient at the boundary (Wyatt, 1978; Mobley, 1994).

5.3.2 Distance Between Collisions

The distance (d) a photon travels in direction ξ before it undergoes a scattering or absorption event is determined by σ and $\kappa(\lambda)$ for the layer. The radiance associated with this photon decreases with distance as

$$L(r) = L(0)\, e^{-\tau},$$

where the optical path length (τ) at any wavelength is given by the product of k ($k = \kappa + \sigma$) and the geometric path length (d),

$$\tau = k\, d. \tag{5.9}$$

d and τ are defined along the path, and in general are not parallel to the surface normal. This decrease in radiance can be explained in terms of the fate of individual photons. If $p(\tau)$ is the probability of any particular photon surviving absorption and scattering out of the beam between optical path lengths τ and $\tau + d\tau$, then

$$p(\tau)\, d\tau \equiv \frac{L(r)}{L(0)} d\tau = e^{-\tau}\, d\tau.$$

The probability that the photon survives between $\tau' = 0$ and $\tau' = \tau$ is given by the cumulative distribution function $P(\tau)$:

$$P(\tau) \equiv \int_0^{\tau} p(\tau')d\tau' = 1 - e^{-\tau}.$$

To sample the probability distribution, $p(\tau)$, we simply select a random number R, and compare its value with the cumulative distribution, $P(\tau)$. R is uniformly distributed on the interval $0 < R < 1$, and $P(\tau)$ varies between 0 and 1. The method of sampling a probability distribution by comparing a random number to the cumulative distribution function is the fundamental principle of Monte Carlo simulation (Cashwell and Everett, 1959). For determining d, this principle states that the equation $R = P(\tau)$ uniquely determines τ such that τ falls in the interval τ to $\tau + d\tau$ with frequency $p(\tau)\, d\tau$. Thus,

$$R = P(\tau) = 1 - e^{-\tau}.$$

Recalling Eqn. 5.9 and solving for the distance to the collision,

Over many computations of this distance, the average distance $\langle d \rangle$ will be the mean free path and is equal to $1/k$, which corresponds to an optical depth of unity. Since k represents the total probability of all scattering and absorption processes, this calculation gives the distance to the next interaction, regardless of whether it is a scattering or absorption event.

5.3.3 Photon Interactions

Each time the distance to a collision is computed, it is compared with the distance to the nearest boundary along the collision trajectory. The photon is advanced to the location of the nearest interaction, either (i) an internal layer boundary, (ii) an external boundary, or (iii) a scattering or absorption event.

If the interaction is with an internal refractive layer boundary, a random number is drawn and the fundamental principle of Monte Carlo simulation is invoked to determine whether the photon is reflected or refracted. If the photon is reflected, it remains within the same layer and the polar angle of its trajectory becomes $\theta' = \pi - \theta$. The remaining distance to the collision is then computed. If the photon is refracted, it transits to the neighboring layer, where the distance to the collision is adjusted to account for differences in the k values between layers. If the interaction is with the top, bottom, or side wall of the cylinder, the photon is reflected and its trajectory continued. To reflect a photon at a curved side wall, the reflection is calculated relative to the local tangent plane. Photons that experience total internal reflection continue to trace out trajectories within the medium. The user specifies whether photons reflect from side walls using Fresnel's principle, or whether they reflect with a specified constant reflection coefficient. To simulate a horizontally-infinite slab, either the cylinder is assigned a radius much larger than its height or the reflection at the side walls can be set to unity.

If the distance to the collision is less than the distance to a boundary, the photon interaction will be a scattering or absorption event. Losing photons to absorption events is computationally inefficient, as a terminated photon no longer contributes to the solution. To eliminate this inefficiency, all interactions are forced to be scattering

events. This bias is taken into account by multiplying W by ϖ_o each time a collision occurs. This represents the probability that this photon has survived this particular interaction, or the fraction of photons in the packet that survive the interaction. Once a scattering event occurs, the direction of the next trajectory is selected by using the fundamental principle of Monte Carlo simulation to sample the polar and azimuthal angles of the phase function. The photon position (ρ, z, ϕ) remains unchanged, but the trajectory direction (θ, χ) is updated.

5.3.4 Photon Counting

When a photon hits the top boundary of a non-refractive medium, it will leave the domain, contributing its full weight to the integral in Eqn. 5.8. When a photon packet hits the top boundary of a refractive medium, a portion of W will be reflected and a portion will generally be transmitted. The reflected portion remains within the medium and continues to scatter until its weight drops below a prescribed threshold (typically $W = 10^{-6}$), potentially interacting with the top surface multiple times. The transmitted portion contributes to the integral in Eqn. 5.8.

In the case of diffuse incident radiation, all photons exiting the upper surface of the domain contribute to the solution. In the case of collimated or nearly collimated incident irradiance, however, the weighting function for the photons exiting the top surface is essentially a Dirac delta function specifying the direction of the collimated incident radiance. Since most of the photons exiting the surface in the adjoint problem receive a zero weighting, this treatment is very inefficient.

Gordon (1985) overcomes this problem by reformulating Eqn 5.8. If the incident irradiance has constant value L_o in a small range of directions represented by the solid angle $\Delta\Omega$ centered on the direction ξ_o, and is zero outside this range, then Eqn 5.5 becomes

$$L_o \int_S dS |\xi_o \cdot u| L_2(r_o, -\xi_o) \Delta\Omega(\xi_o) = J_o E_d(r_d), \tag{5.10}$$

where the right hand side is derived exactly as before. The incident irradiance is given by

$$E_d(\boldsymbol{r}_o) = |\boldsymbol{\xi}_o \cdot \boldsymbol{u}|\, L_o\, \Delta\Omega(\boldsymbol{\xi}_o)\,,$$

and we define

$$E_{u2}(\boldsymbol{r}_o, -\boldsymbol{\xi}_o) \equiv L_2(\boldsymbol{r}_o, -\boldsymbol{\xi}_o)|\boldsymbol{\xi}_o \cdot \boldsymbol{u}|\Delta\Omega(\boldsymbol{\xi}_o)$$

to be the upward irradiance at S resulting from photons in the solid angle $\Delta\Omega(\boldsymbol{\xi}_o)$. When these definitions are substituted into Eqn. 5.10, the equation analogous to Eqn. 5.8 becomes

$$\frac{E_d(\boldsymbol{r}_d)}{E_d(\boldsymbol{r}_o)} = \frac{\pi}{P_2|\boldsymbol{\xi}_o \cdot \boldsymbol{u}|\Delta\Omega'(\boldsymbol{\xi}_o')} \int_S \mathrm{E}_{u2}(\boldsymbol{r}_o, -\boldsymbol{\xi}_o)dS\,, \tag{5.11}$$

where P_2 is defined as in Eqn. 5.7 for the diffuse case. To compute the downwelling irradiance at the detector relative to the incident downwelling irradiance, $E_d(\boldsymbol{r}_d)/E_d(\boldsymbol{r}_o)$, we need only evaluate the integral in Eqn. 5.11. This integral is the total power exiting the surface in $\Delta\Omega(\boldsymbol{\xi}_o)$ due to the source $Q_2(\boldsymbol{r}, \boldsymbol{\xi})$. To evaluate this integral, the contribution from photons that do not scatter within the medium is counted separately from the contribution of photons that do scatter.

The non-scattering contribution is simply the fraction of the incident beam that reaches the detector unscattered. For a transmissivity detector in a non-refractive domain, this is simply

$$\exp\left[-\int_0^l k(l)dl\right],$$

where l is the path length between the detector and the surface along $\boldsymbol{\xi}_o$. For a refractive domain, multiple reflections off the top, bottom, and internal layer surfaces must be taken into account. These multiple reflections reduce the magnitude of the incident beam reaching the detector. For an albedo detector, the direct contribution is simply the sum of all upwelling multiple Fresnel reflections. In all cases, the contribution from photons that do not scatter is added to the detector bin whose normal is in the direction of $\boldsymbol{\xi}_o$.

The contribution to the integral from photons which do interact with the medium is computed by Monte Carlo simulation using the method of expected values. Photons are emitted from $\boldsymbol{r}_d$ with $W = 1$, and allowed to scatter in the medium. The probability that the jth photon at $\boldsymbol{r}$ traveling in the direction $\boldsymbol{\xi}$, at the time of its ith interaction with the medium would survive the scattering event and exit the domain in the small solid angle $\Delta\Omega(\boldsymbol{\xi}_o)$ is

$$P_{ij} = \varpi_o(\boldsymbol{r})\, p(\boldsymbol{r}, \boldsymbol{\xi} \rightarrow \boldsymbol{\xi}_o')\, \Delta\Omega'(\boldsymbol{\xi}_o')\, exp\left[-\int_0^{l'} k(l')dl' \right] \tag{5.12}$$

where $p(\boldsymbol{r}, \boldsymbol{\xi} \rightarrow \boldsymbol{\xi}'_o)$ is the scattering phase function, β/σ, and l' is the path that would be taken by the photon to the surface. The contribution of the ith photon collision to the irradiance incident on S is the product of the ith photon weight, W_i, and P_{ij} as given in Eqn. 5.12. Summing the weights over all collisions i and many photon trajectories j, the result is $\sum_{ij} W_i P_{ij}$. Finally, combining this with the contributions from noninteracting photons, Eqn. 5.11 becomes

$$\frac{E_d(\boldsymbol{r}_d)}{E_d(\boldsymbol{r}_o)} = \frac{\sum_{ij} W_i P_{ij}}{P_2 \left| \boldsymbol{\xi}_o \cdot \boldsymbol{u} \right| \Delta\Omega'(\boldsymbol{\xi}_o')} + exp\left[-\int_0^{l} k(l)dl \right]. \tag{5.13}$$

As with the diffuse case, any type of detector can be modeled by inserting the suitable source function $Q_2(\boldsymbol{r}, \boldsymbol{\xi})$ into the reciprocity relation of Eqn. 5.2.

Equation 5.13 specifies how photons are counted for the case of collimated incident illumination. A contribution to the sum $\sum_{ij} W_i P_{ij}$ is made at each scattering event. Since $\sum_{ij} W_i P_{ij}$ is directly proportional to $\Delta\Omega'(\boldsymbol{\xi} o')$, $E_d(\boldsymbol{r}_d)/E_d(\boldsymbol{r}_o)$ is independent of $\Delta\Omega'(\boldsymbol{\xi} o')$. P_2 is equal to πJ_o, where J_o is the total number of photons released at the detector. Note also that the final result does not depend on J_o, as the maximum sum of all W_i approaches J_o.

5.3.5 Refractive Domain

For a refractive domain the contribution from photons that do not scatter within the medium is derived in Section 5.3.4. The contribution from photons that scatter must also be adjusted, however. Consider the case of a detector in the ocean with collimated sunlight incident on the refractive sea surface. To adjust Eqn. 5.13 for this single refractive boundary we must account for the fact that the direct beam intensity is reduced by the air-ocean Fresnel transmission coefficient. This means that each time P_{ij} is evaluated, it is reduced by a factor of $t(\xi, m)$.

In the case of a domain with multiple refractive boundaries (e.g., an ice slab in air with top and bottom refractive boundaries), Fresnel transmission and reflection at the upper and lower boundaries cause the incident direct beam to be multiply reflected within the ice. If the top surface is illuminated uniformly, the direct beam has upwelling and downwelling components at the location of all scattering events. The magnitude of these components is determined by the internal and external refractive boundaries, as well as by beam attenuation within the domain. Let $L(r, -\xi_o)$ be the magnitude of the downwelling direct beam at the location of the scattering event and $L(r, \xi_o)$ the magnitude of the upwelling direct beam at the same location. Both quantities include the cumulative effects of multiple reflections and path-dependent beam attenuation and can be calculated using a simple version of the doubling method (e.g., Barkstrom and Querfeld, 1975), as implemented by Grenfell (1991). As a result, P_{ij} in Eqn. (5.12) must also be computed for $p(r, \xi \rightarrow -\xi_o')$. Using $L(r, \xi_o)$ as defined here, we can express Eqn. 5.12 as

$$P_{ij} = \varpi_o(r)\, p(r, \xi \rightarrow \xi_o')\, \Delta\Omega'(\xi_o')\, L(r, -\xi_o)\,.$$

The exponential term in Eqn. (5.12) is now included in the magnitudes of $L(r, -\xi_o)$ and $L(r, \xi_o)$. We now include the contribution for scattering events where the photon scatters into the upwelling direct beam, and Eqn. 5.12 becomes

$$P_{ij} = \varpi_o(r)\, \Delta\Omega'(\xi_o') \cdot \left\{ p(r, \xi \rightarrow \xi_o')\, L(r, -\xi_o) + p(r, \xi \rightarrow -\xi_o')\, L(r, \xi_o) \right\}.$$

Eqn. 5.13 remains unchanged, except that the exponential term representing the noninteracting photons is replaced by $L(\boldsymbol{r}_d, -\xi_o)$ for a transmissivity detector.

5.3.6 Convergence Criterion

Before starting a calculation, it is not possible to know a priori how many photons to follow through the domain. Some cases (e.g., isotropic scattering or small optical depth) require fewer photons to converge upon an estimated solution than others (e.g., strongly forward-peaked scattering or large optical depth). If we release an insufficient number of photons for a given detector, we undersample the phase function or the scattering, resulting in solutions with significant error. Sending extra photons does no harm, but is computationally inefficient.

Because the Monte Carlo calculation is composed of individual, independent, yet identically calculated photon histories determined by the selection of random numbers, multiple solutions for the same detector initiated with different random numbers generate a distribution that is normal about the mean. Each sample of this distribution is obtained by running the model for a specified number of photons (typically one photon per detector bin for an irradiance calculation with 3500 detector bins). A convergence test is performed after 10 samples have been run, and then after each additional sample is added to the distribution. When a sufficient number of samples have been collected such that the convergence criterion is met, the mean value of all samples ($\bar{x}$) is taken as the estimate to the solution. The convergence criterion is met when the width of the distribution of solutions becomes smaller than a user-specified tolerance. The width of the distribution is computed using an interval estimate of the population mean for small sample cases where the population standard deviation is not known (Anderson et al., 1981). Because convergence is tested with as few as 10 samples, standard t-distributions are used to evaluate the width:

$$\textit{width of distribution} = \frac{t_{\alpha/2} \cdot s_{\bar{x}}}{\bar{x}}$$

The t-value is based on a t-distribution with N-1 degrees of freedom where N is the number of samples, α is the user-specified tolerance, and $s_{\bar{x}}$ is the standard deviation of the samples divided by $\sqrt{N}$.

5.4 Tests of the Model

A series of calculations were carried out with the model to test conservation of energy. Because Monte Carlo calculations are done for only one radiometric quantity at one location at one time, we can use multiple computations to determine whether energy is properly conserved in a given domain. The simplest example is the computation of albedo and transmissivity for a conservatively-scattering infinite slab. With no absorption present and no side walls, the sum of albedo and transmissivity should equal unity. The model passes this test to within the tolerance of the albedo and transmissivity computations (< 1%). Other tests were done, including a complete energy balance for a cylindrical domain (see Fig. 5.7).

Predictions from the Monte Carlo model were then compared to those from several existing radiative transfer models. We first tested the plane-parallel, infinite horizontal case because solutions to this problem are well established and widely available. In particular, we utilized results from 4-stream (Grenfell, 1991) and N-stream (Jin et al., 1994) discrete ordinates models (DOM). For these tests, the cylindrical model was used to simulate a horizontally infinite domain by making the cylinder radius very large compared to its height (radius to height ratio > 200). Detectors were positioned at radius = 0. Alternatively, setting the cylinder side wall reflectivity to unity can also be used to simulate a horizontally-infinite case. All tests were conducted using Henyey-Greenstein phase functions with associated asymmetry parameter, g_{HG}.

5.4.1 Radiance Detector

The radiance detector in the Monte Carlo model was initially tested by comparing results with radiances computed from tabulated solutions to Chandresakhar's X and Y functions (Sobouti, 1963). These tables are available for isotropic scattering (g = 0.0)

for normal optical depth $\tau = 0.1$ to 3.0 and $\varpi_o = 0.10$ to 1.00 in non-refractive slabs. Radiances computed with the Monte Carlo model and the tabulated values are shown in Figure 5.2 for $\varpi_o = 1.0$ and $\tau = 1.0$ for viewing angles greater than zenith ($\theta = 0°$) and less than nadir ($\theta = 180°$). The incident light is collimated, but only the diffuse component of the scattered light is shown; the transmitted and reflected direct beams are not included. The Monte Carlo model produced excellent results at all viewing angles.

5.4.2 Optical Depth and Asymmetry Parameter

We next examined backscattered and transmitted irradiances as a function of τ and g for a horizontally-infinite slab with conservative scattering. Figures 5.3 (a) and (b) show albedo and transmissivity calculated with the Monte Carlo model along with 4-stream and 16-stream DOM results for a non-refractive domain. The albedo and transmissivity were tested for optical depths between 1 and 50 and $g_{HG} = 0.00$, 0.50, 0.75, 0.90, and 0.95. All three models predict very similar irradiances over this range of τ and g.

Because scattering in sea ice is known to be strongly forward-peaked, we were particularly interested in model predictions for cases where $g > 0.90$. Figures 5.4 (a) and (b) compare Monte Carlo predictions of albedo and transmissivity as a function of τ and g_{HG} for large g with those of the 4- and 16-stream DOM models. The comparisons for this non-refractive domain are excellent until the transmissivity is computed for small τ with g_{HG} exceeding ~ 0.97 (see Fig. 5.4 [b]). When the phase function is very strongly forward peaked, scattering events occurring at large angles become increasingly rare. When this happens, the distribution of Monte Carlo solutions deviates from a normal distribution and the mean radiance becomes progressively larger than the most probable radiance. Clearly, the transmissivity for $\tau \leq 1$ and $g \geq 0.97$ manifests this problem, as the Monte Carlo results depart from the DOM results. Since Monte Carlo transmissivities exceed 1 in this region they are clearly non-physical and computations in domains with such low scattering and large g values should not be relied upon with the Monte Carlo model.

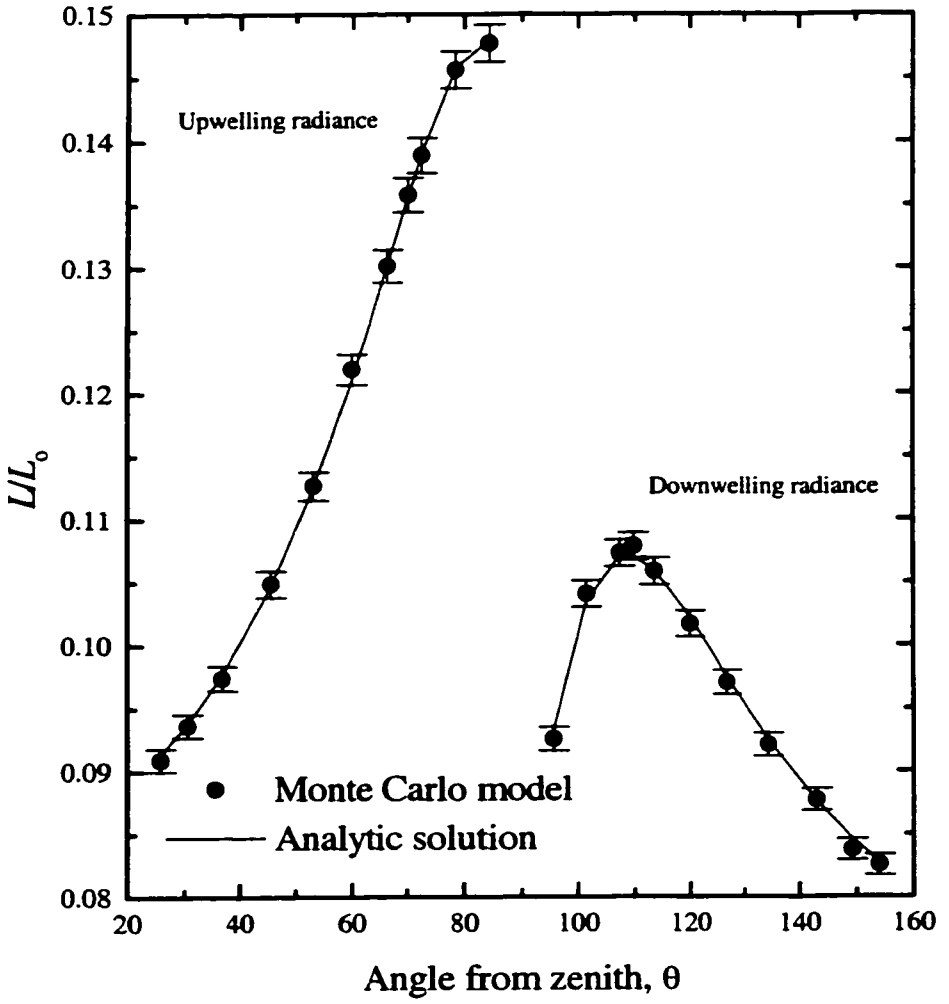

Figure 5.2. Comparison of relative radiance (L / L_o) distribution for Monte Carlo model and tabulated values for Chandresekhar's X and Y values (Sobouti, 1963). The domain is a horizontally infinite slab with optical depth = 1.0 asymmetry parameter = 0.0 and conservative scattering. Monte Carlo model tolerance was set at 1%, as shown by the error bars.

5.4.3 Refractive Domain

The model was then applied to a slab with refractive boundaries. The sensitivity of the albedo and transmissivity of a refractive slab increases with increasing scattering

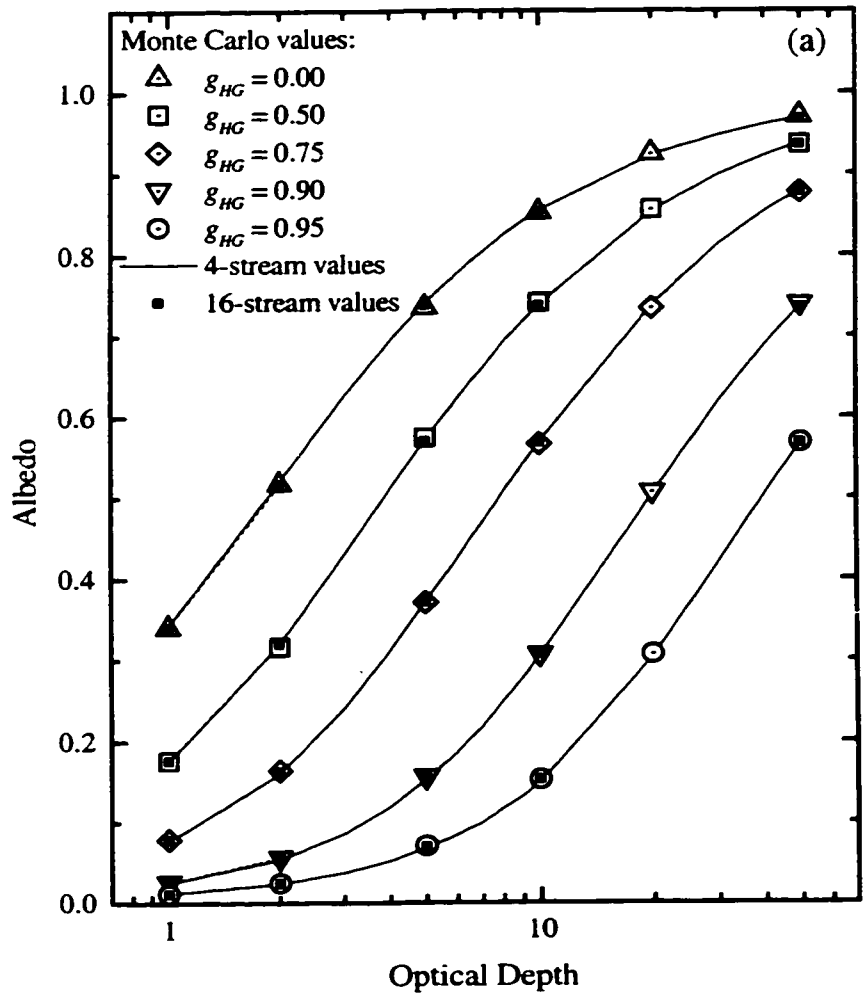

Figure 5.3. Comparison of (a) albedo and (b) transmissivity as a function of Henyey-Greenstein asymmetry parameter (g_{HG}) and optical depth for a non-refractive slab with conservative scattering. The Monte Carlo values are shown with open symbols and have tolerance of 1%. The 4-stream DOM values are shown with solid lines, and 16-stream DOM values are indicated with solid squares.

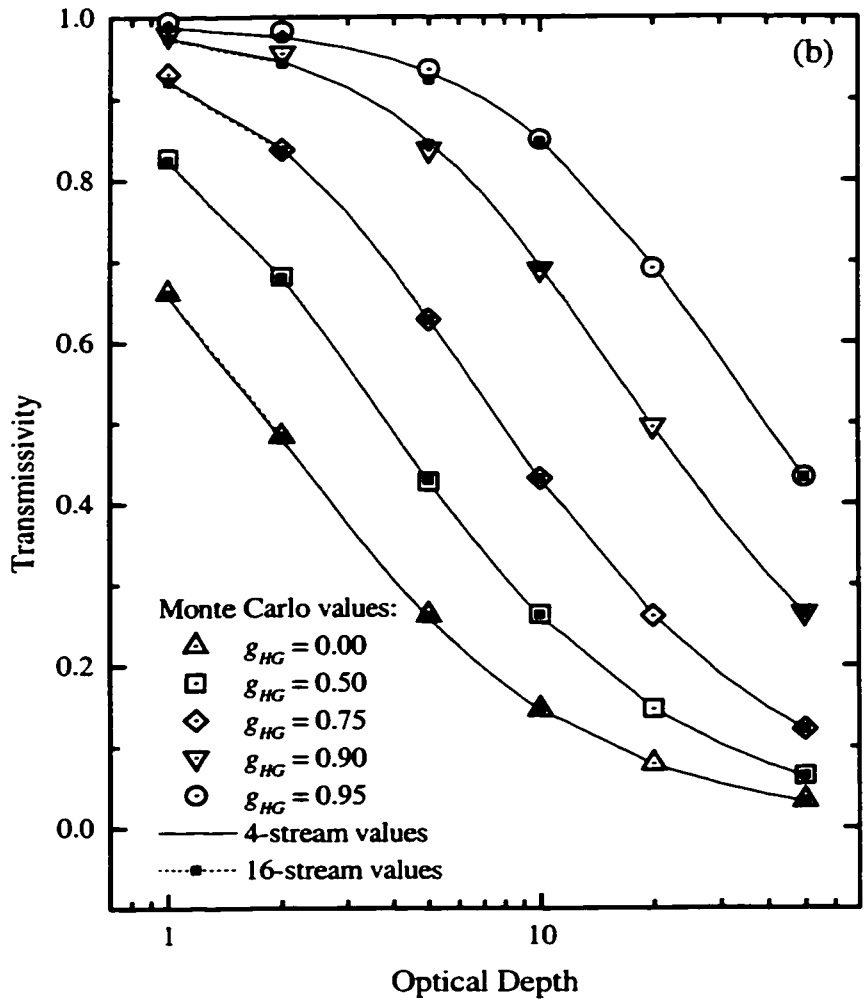

Figure 5.3 continued

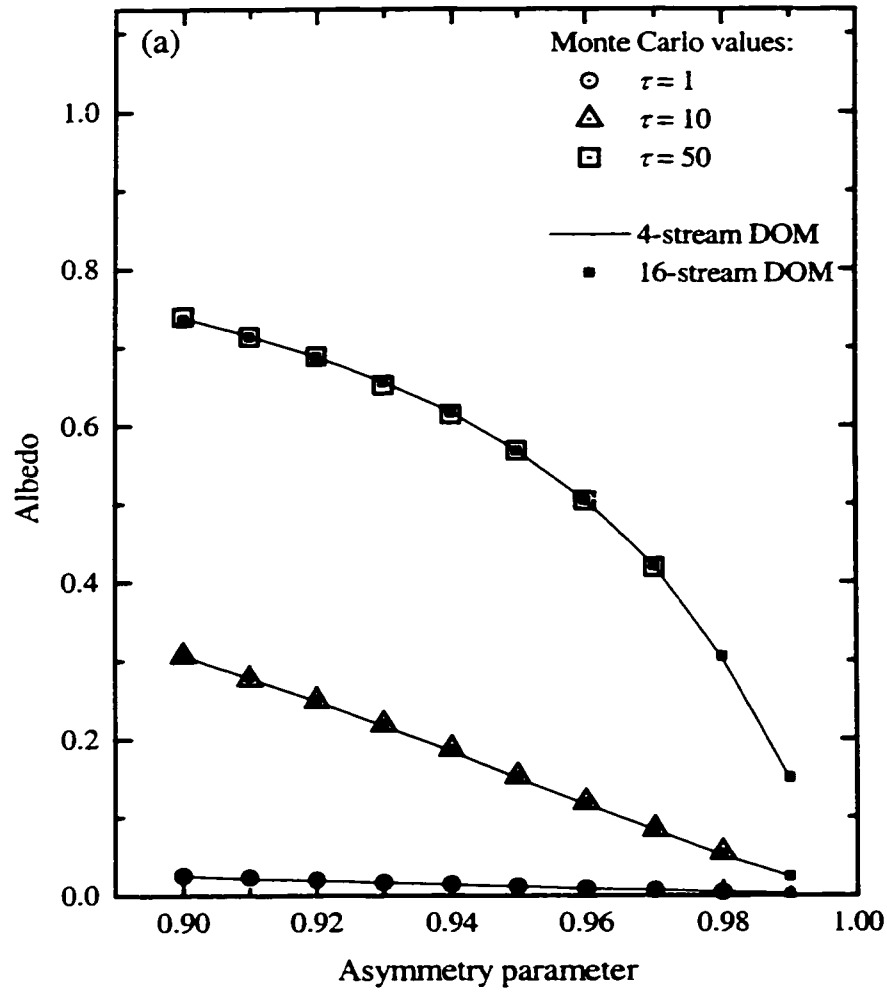

Figure 5.4. Comparison of (a) albedo and (b) transmissivity as a function of optical depth (τ) for large Henyey-Greenstein asymmetry parameter in a non-refractive slab with conservative scattering. The Monte Carlo values are shown with open symbols and have tolerance 1%. The 4-stream DOM values are shown with solid lines, while 16-stream results are indicated by solid squares.

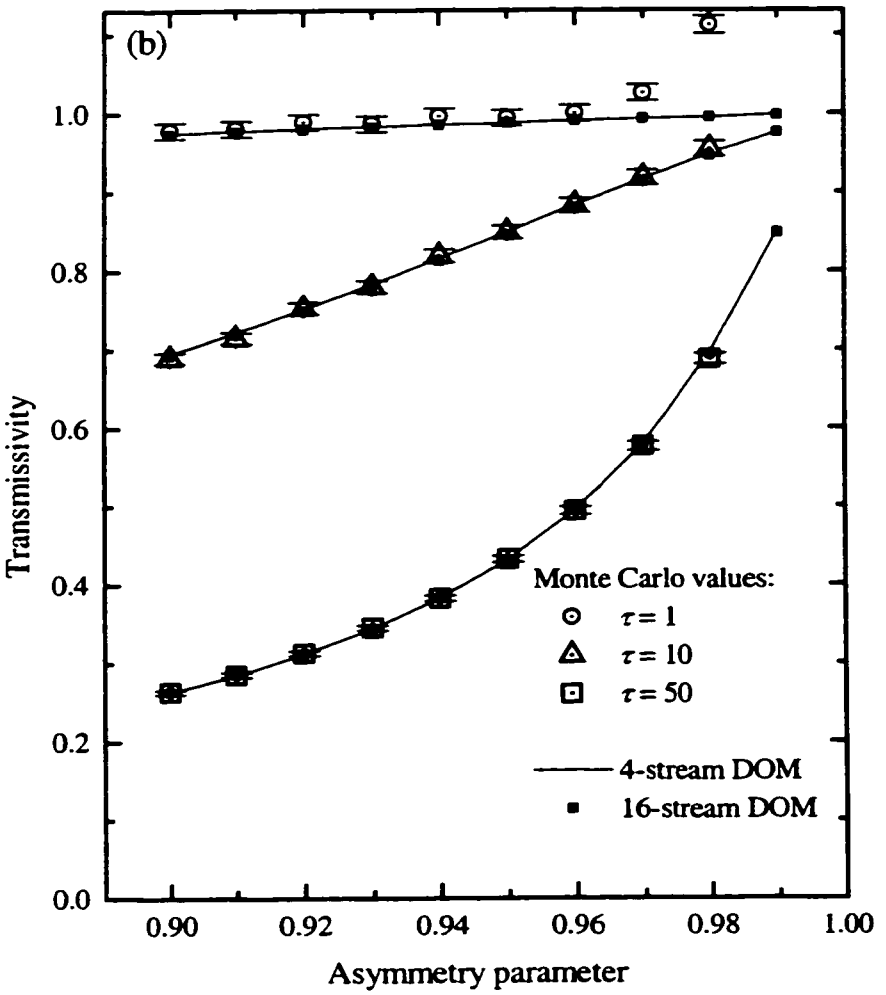

Figure 5.4 continued

because each time a photon is incident on a refractive boundary the likelihood of the photon reflecting rather than refracting is increased. For this reason, photons become less likely to penetrate boundaries when the refractive index of the domain increases. Also, when the sample is refractive, the backscattered field has a directly reflected component. Predictions of albedo and transmissivity as a function of τ and g for a slab with the refractive index of ice at $\lambda = 500$ nm ($m = 1.31$) are shown for the Monte Carlo and the 4-stream DOM models in Figs. 5.5 (a) and (b). Both albedo and transmissivity detectors are external to the refractive slab. The agreement between models is excellent.

5.4.4 Non-conservative scattering

Spectral computations were then carried out with the Monte Carlo model for wavelengths $\lambda = 500 - 1000$ nm for non-conservative scattering in a refractive domain. The slab was assumed to be 15 cm thick and was assigned a scattering coefficient ($\sigma = 0.25$ mm^{-1}) and asymmetry parameter ($g_{HG} = 0.95$) representative of sea ice in the transition zone (Mobley et al., 1998); other optical properties used in the calculations are given in Table 5.2. The incident radiation was assumed to be direct and the refractive index of the ice relative to air to be $m = 1.31$. We adopt the values of $\kappa(\lambda)$ given in Table 5.2 for all further work in sea ice.

Albedo and transmissivity estimates from the Monte Carlo model and the 4-stream model are shown in Fig. 5.6. Clearly, the Monte Carlo model properly treats non-conservative scattering in a refractive domain. Maximum discrepancies are on order of

Table 5.2. Optical properties representative of transition sea ice at six wavelengths used for the Monte Carlo model calculations shown in Figure 5.6. Values of $\kappa(\lambda)$ are from Grenfell and Perovich, 1981.

Wavelength (nm)	κ (mm^{-1})	τ	ϖ_o
500	4.8E-5	37.51	0.9998
600	0.00012	37.52	0.9995
700	0.00052	37.58	0.9979
800	0.0021	37.81	0.9917
900	0.00586	38.38	0.9771
1000	0.02036	40.55	0.9247

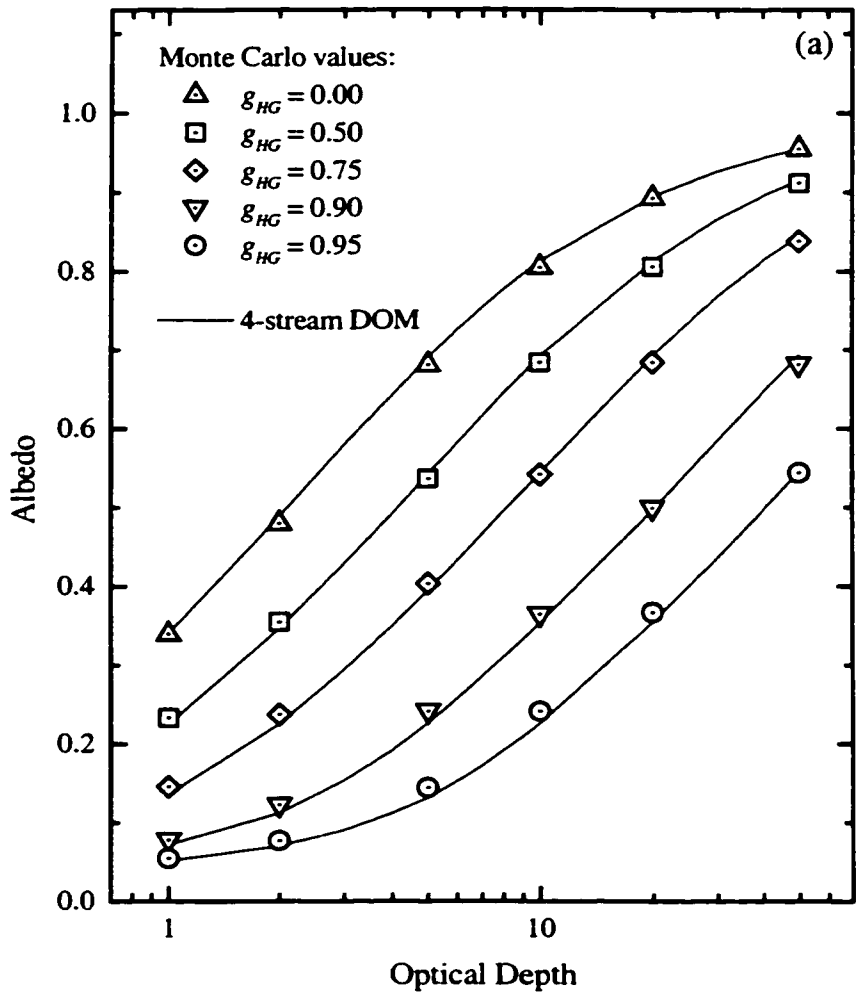

Figure 5.5. Comparison of (a) albedo and (b) transmissivity as a function of optical depth and Henyey-Greenstein asymmetry parameter (g_{HG}) for a refractive ($m = 1.31$) slab with conservative scattering. The Monte Carlo values are shown with open symbols and have tolerance 1%. The 4-stream DOM values are shown with solid lines.

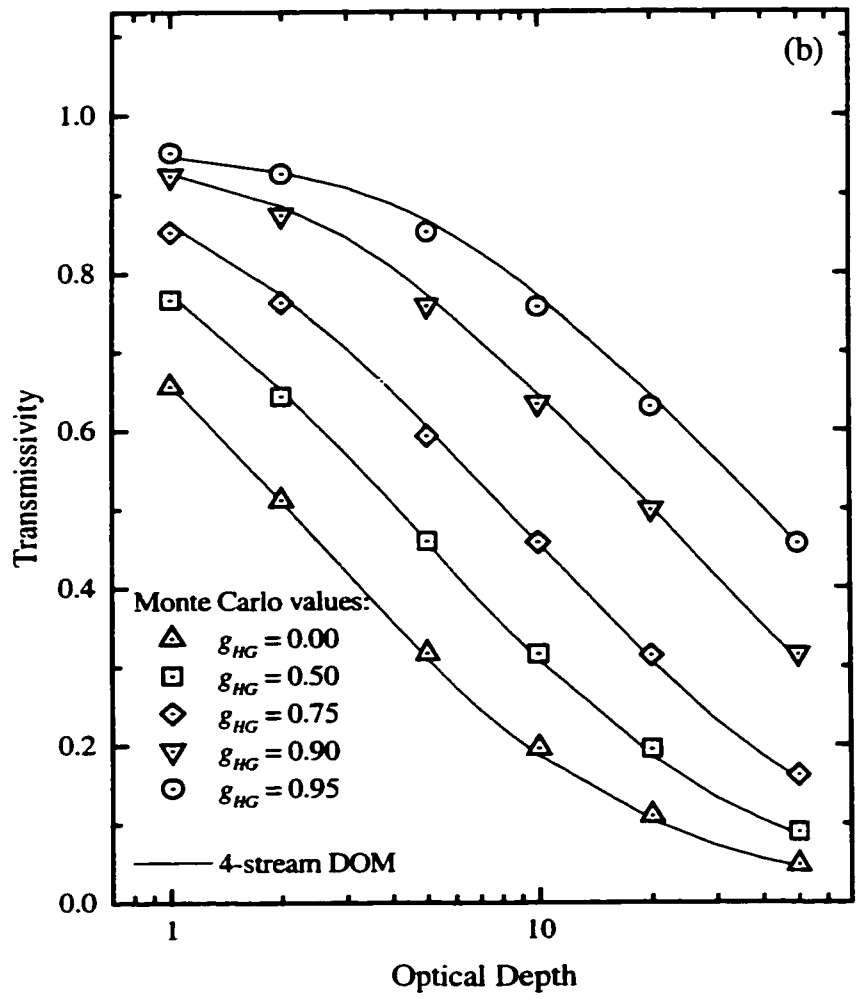

Figure 5.5 continued

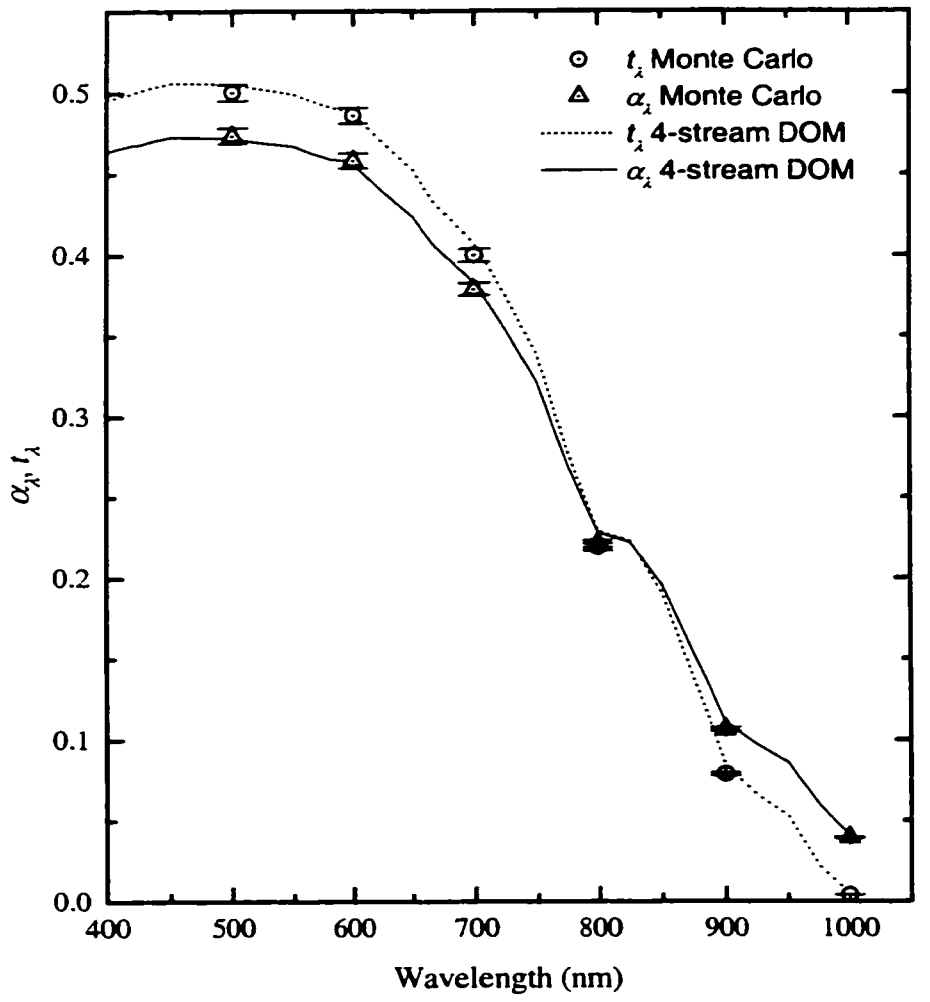

Figure 5.6. Comparison of spectral albedo (α_λ) and transmissivity (t_λ) for Monte Carlo and 4-stream DOM models. The slab is 15 cm thick and its inherent optical properties are given in Table 5.2. Monte Carlo results are shown with open symbols, DOM values with solid lines.

5%. This is no larger than the magnitude of the typical discrepancies in the refractive domain comparison of Fig. 5.5.

5.4.5 Horizontally Finite Domain

We next investigate the effect of a horizontally-finite domain on the partitioning of energy between backscattered, transmitted, and side-welling fluxes. When we used a cylinder with large radius to simulate an infinite slab in the previous sections, photons released from the detector rarely interacted with the side wall. As the cylinder radius decreases, interactions with the side wall become increasingly common. Each time a photon is incident on the side wall, portions of the photon packet may be transmitted through the wall and lost from the domain. The cumulative effect of these interactions is that energy lost from the domain through the side walls leaves less energy to be backscattered and transmitted through the top and bottom surfaces.

Let us first examine energy partitioning for a non-refractive cylinder with radius 5 cm, height (H) 5 cm, and normal, direct-beam incidence. We chose this size cylinder as it corresponds to the core samples used in the optical property observations discussed in Chapter 6. Figure 5.7 shows the amount of energy at 500 nm leaving the top, bottom, and side surfaces relative to the incoming energy, as a function of scattering coefficient. Energy leaving each surface is estimated by numerically integrating irradiances computed along the radius of the cylinder. The energy leaving the side wall is estimated by integrating irradiances computed at five heights along the wall. For these calculations, $g_{HG} = 0.0$. As the scattering coefficient increases, more incident downwelling radiation is redirected, increasing the sidewelling and backscattered fluxes and decreasing the transmitted flux. For large σ, the sidewelling energy is substantial, and approaches the value of the transmitted energy. Clearly, the presence of the side walls cannot be ignored when σ is large.

To further validate the cylindrical Monte Carlo treatment, we attempted to locate a cylindrical radiative transfer model for comparisons. Although we were unable to find a model that would treat a refractive, cylindrical domain, we were able to find one that could describe a non-refractive cylindrical domain. The model TWODANT (Alcouffe

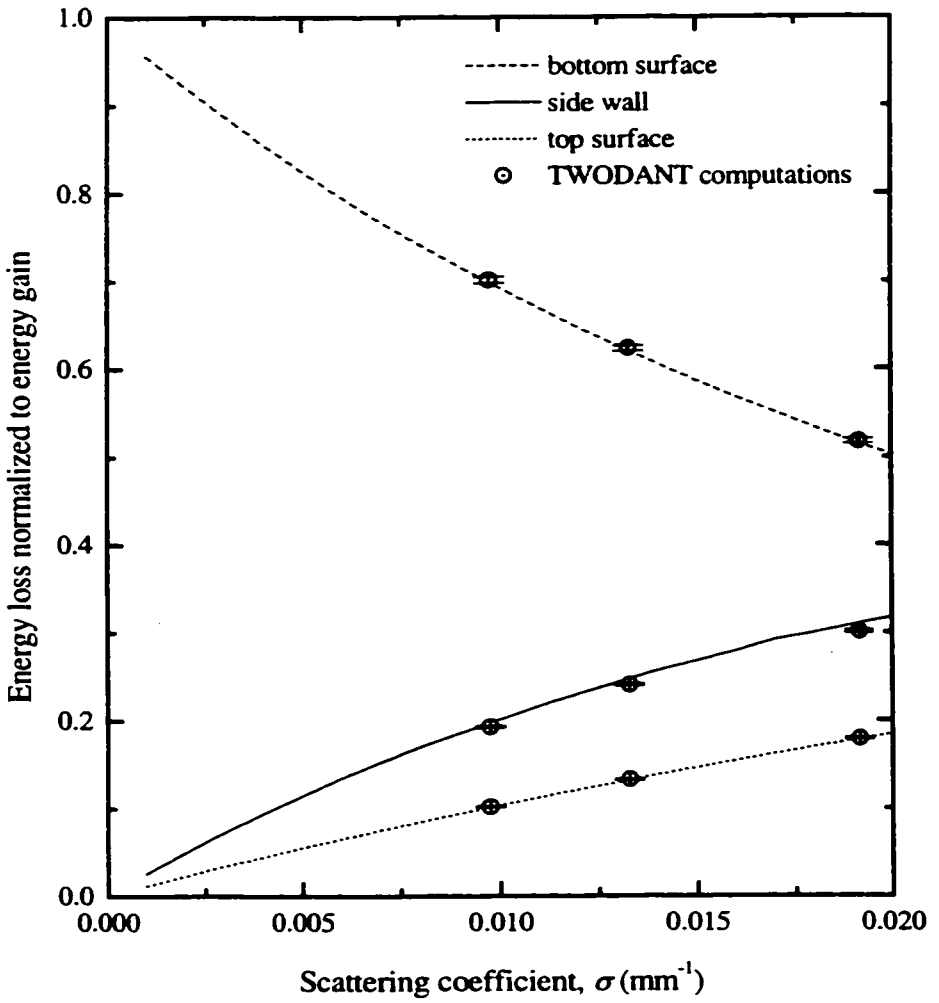

Figure 5.7. Calculations of normalized energy loss out top, bottom, and side surfaces of a non-refractive cylinder as a function of scattering coefficient. The cylinder radius = 5 cm, height = 5 cm , the incident radiation is collimated, the absorption coefficient = 4.8E-5 mm^{-1}, and the scattering is isotropic. Lines show values computed with the Monte Carlo model, open circles show points computed with the model TWODANT (Alcouffe et al., 1997).

et al., 1997) is a 2-D spherical harmonics model designed to solve the transport equation for neutral particles. Results from this model (R. Alcouffee, personal communication, 1999) are also shown in Fig. 5.7. The estimated uncertainty in the TWODANT calculations is 0.5%. The uncertainty in the Monte Carlo calculations is 1%. The agreement between models is excellent.

Figure 5.8 shows how changes in the radius of a cylinder of ice with $H = 5$ cm affect the partitioning of energy. The cylinder radius was varied from 0.7 to 400 cm. Values for σ (0.25 mm^{-1}) and g_{HG} (0.95) were from Mobley et al. (1998). This test indicates that the normalized sidewelling energy from a cylinder of sea ice does not drop below 0.01 until the domain radius reaches 180 cm (height-to-radius ratio of ~36). Clearly, sidewelling energy losses cannot be ignored when trying to infer the AOPs of sea ice cores in the laboratory.

5.5 Similarity parameter

In the theory of radiative transfer, similarity relations permit (with fair accuracy) the reduction of the number of independent variables by one in certain functions. We will exploit a particular similarity parameter, s, that is a convenient way of combining σ/κ and g, and is defined (van de Hulst, 1980) as

$$s = [\, 1 + (\sigma/\kappa)(1-g)]^{-1/2}.$$

Apparent optical properties are similar for domains with different values of σ/κ and g, but with the same s. The value of s varies from 0 to 1, approaching 1 as κ and g become large. Figure 5.9 shows how s^{-1} depends on g and σ. For this figure, κ was held constant at 4.8E-5 mm^{-1}, its value for ice at $\lambda = 500$ nm. The similarity parameter can be represented by a continuous range of (σ, g) pairs. This similarity parameter has been exploited by a number of authors for inferring various IOPs from observations. For example, McCormick and Rinaldi (1989) used it to infer scattering coefficients from in-situ irradiance measurements in seawater. King et al. (1990) also used it to infer single scattering albedos for clouds from airborne in-cloud radiance measurements.

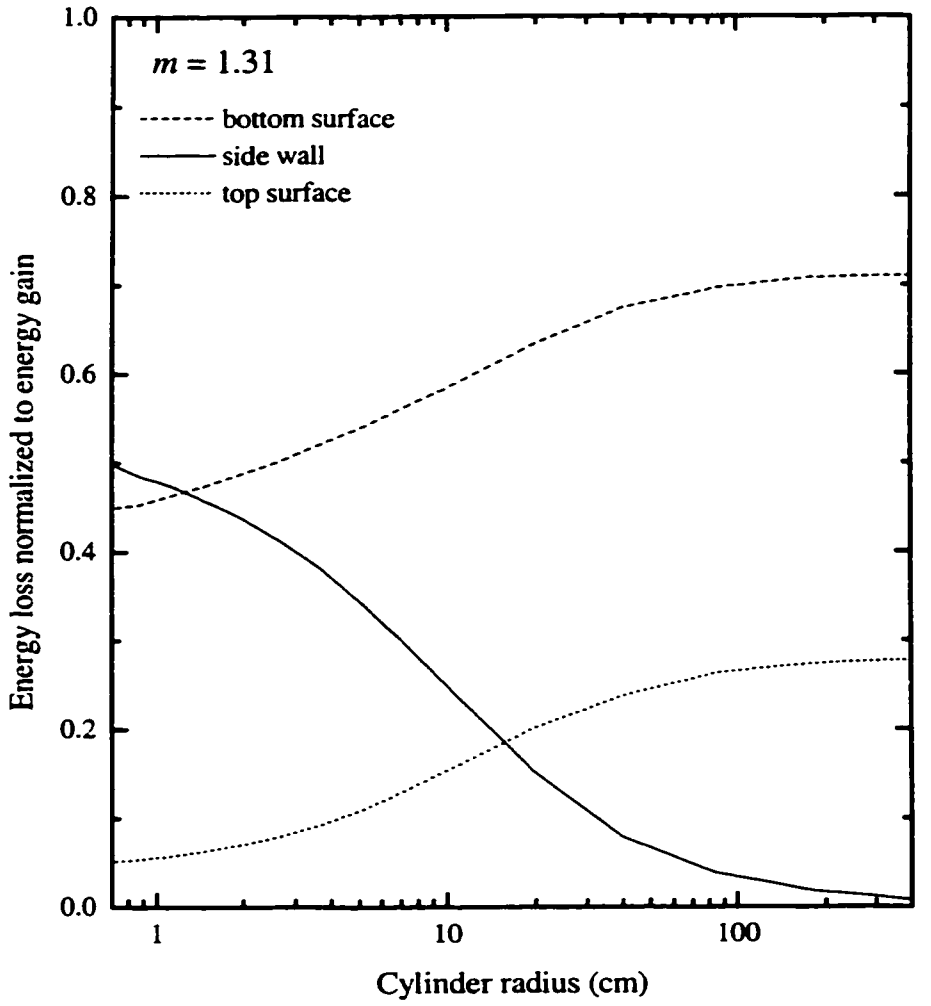

Figure 5.8. Calculations of energy loss integrated over top, bottom, and side surfaces of an ice cylinder as a function of domain radius. Cylinder height is 5 cm, the incident radiation is collimated, the single scattering albedo is 0.9998, the scattering coefficient is 0.25 mm^{-1}, the Henyey-Greenstein asymmetry parameter is 0.95, and the relative refractive index is 1.31. The energy out each surface is normalized by the energy incident on the top surface.

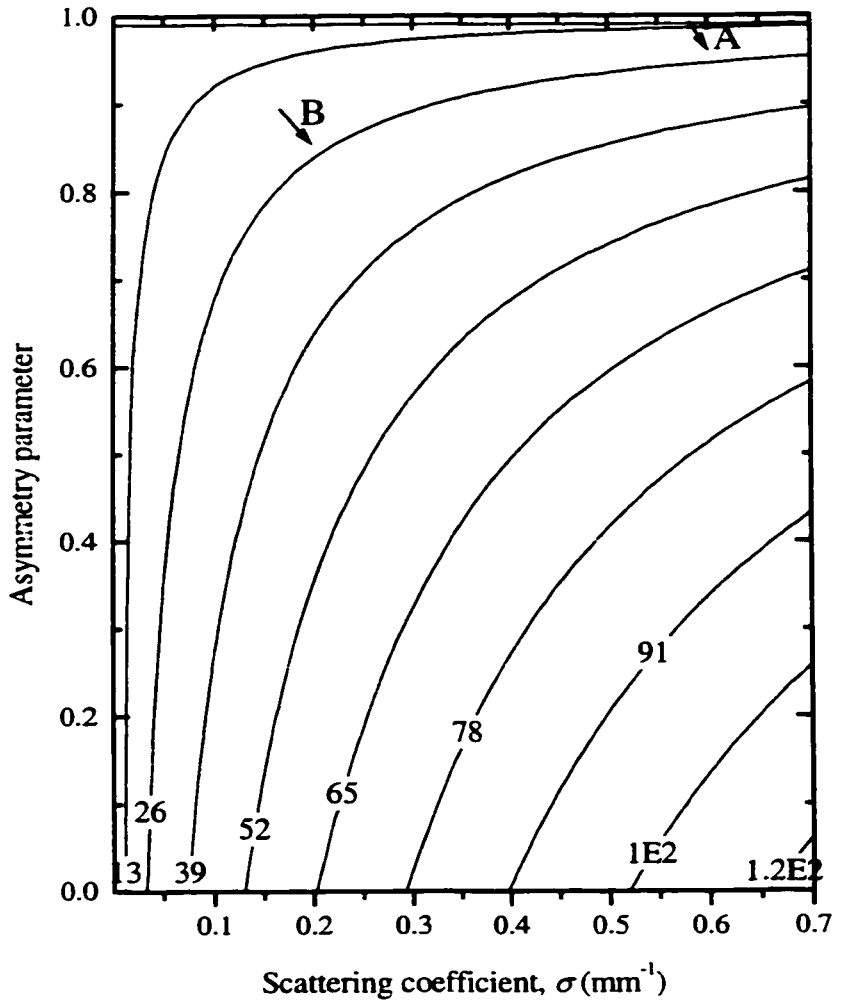

Figure 5.9. Graphical representation of the inverse of the similarity parameter, (s^{-1}), as a function of scattering coefficient and asymmetry parameter. Lines of constant s^{-1} have nearly the same apparent optical properties.

We use s in two ways. First, it is used to reduce the time required for Monte Carlo simulations. Because it is necessary to sample increasing numbers of photons as g increases, computations for sea ice are slow. Since domains with different values of σ and g, but identical s, will have approximately the same AOPs, we can substitute a faster (smaller g) case for situations where g is large. If, for example, our original problem requires running a Monte Carlo simulation for $\sigma = 0.6$ mm^{-1} and $g_{HG} = 0.95$ (denoted by point A in Fig. 5.9), we would calculate a value of s^{-1} of ~ 26. The contour for $s^{-1} = 26$ also intercepts $\sigma = 0.2$ mm^{-1}, $g_{HG} = 0.84$ (denoted by location B in Fig. 5.9), which is a much faster computation.

Since use of the similarity parameter is only approximate, care must be taken when substituting calculations with much smaller g values. Figure 5.10 shows Monte Carlo predictions of albedo, transmissivity, and side irradiance as a function of cylinder radius for a variety of (σ, g) pairs with common s for a cylinder with $H = 5$ cm. The calculations are similar to those in Figure 5.8, except the irradiances are not integrated over the entire surface. The albedo and transmissivity are computed at the center of the top and bottom surfaces, and the side irradiance is computed at $H/2$. The results for $g = 0.90$ are an excellent proxy for $g = 0.95$. This figure demonstrates that s is only an approximation, and is not exact. For computations with $g = 0.80$, the AOPs begin to differ and when $g = 0.0$, the approximation is poor. This figure can be used as a guide for selecting the range of (σ, g) pairs that can be used to reduce computation time.

We also use the similarity parameter as a tool for interpreting AOP observations. If AOPs are not the result of unique (σ, g) pairs, then it is not possible to infer σ and g independently unless we have independent information about one or the other. By using the similarity parameter, we can reduce the independent variable from σ/κ and g to s alone. This will be useful in analyzing the AOP data presented in the following chapter.

5.6 Summary

A Monte Carlo model has been developed to predict radiative transfer in refractive, cylindrical domains. This model is needed to infer IOPs from the AOP data presented

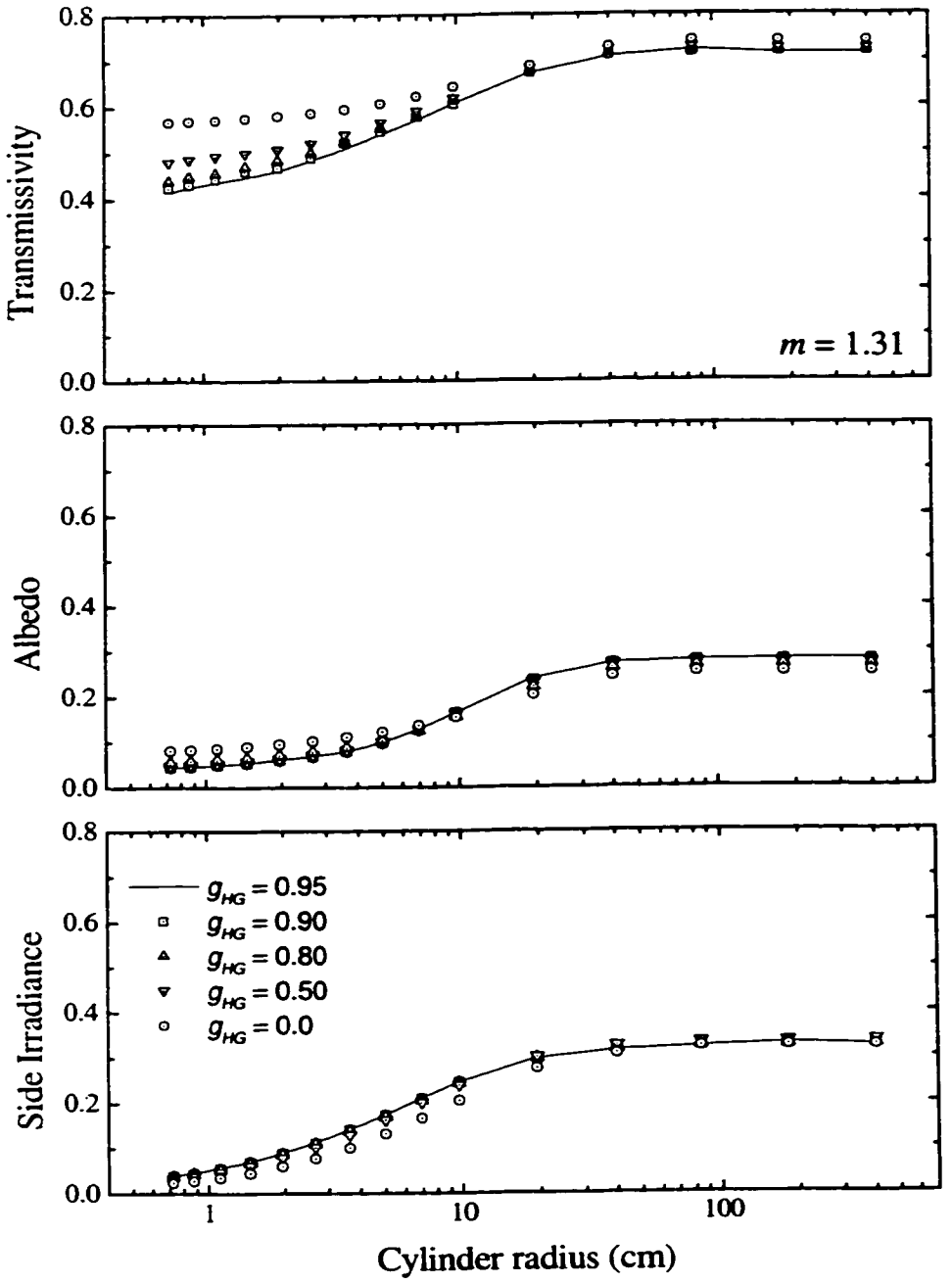

Figure 5.10. Computed albedo, transmissivity, and side irradiance as a function of cylinder radius and asymmetry parameter (g_{HG}). The albedo and transmissivity are computed at the center of the top and bottom surfaces, the side irradiance is computed at the height of 2.5 cm. The cylinder has height 5 cm and relative refractive index m = 1.31. Each curve has asymmetry parameter as indicated, but similarity parameter is constant (s = 0.0618) and absorption coefficient is 4.8E-5 mm^{-1}.

in the next chapter, but has broader application as well. It is applicable to both cylindrical and horizontally-infinite domains with multiple horizontal refractive layers, and even includes the capability to treat domains with multiple concentric refractive shells, as well. For example, we expect that this model will prove useful for analyzing field data where cylindrical bore holes are used to collect optical data about pack ice.

The model handles cases for $0 \leq \varpi_0 \leq 1$ and $\tau \geq 0$. Cases with Henyey-Greenstein phase functions with $|g_{HG}| < 0.98$ are reliably calculated for all domains except when $\tau \leq 2$. The model also accepts user-tabulated phase functions, such as those calculated with Mie theory. Most scattering problems result in azimuthally symmetric phase functions, but this model can be formulated for non-symmetric phase functions as well.

CHAPTER SIX
LABORATORY OBSERVATIONS OF SEA ICE OPTICAL PROPERTIES

This chapter describes laboratory measurements of the apparent optical properties of first-year sea ice taken over a range of temperatures between –33 and –0.5 °C. Inherent optical properties (IOPs) of the ice are then derived from these observations using the radiative transfer model described in Chapter 5. Combining these results with the structural data presented in Chapter 4 provides a basis for examining structural-optical relationships in first-year sea ice.

6.1 Experiment Design

Optical measurements were made on an ice sample taken a few centimeters deeper in the same core used to obtain the thin section as described in Chapter 4. To ensure that the samples for the physical and optical studies experienced similar thermal histories, both sets of observations were run simultaneously in the same cold room laboratory. A cylindrical sample with 5 cm radius and 5 cm height (H) was prepared at –15 °C. The sample was first cut on a bandsaw so that its total thickness was slightly greater than 5 cm. The top and bottom surfaces were then microtomed until the sample thickness was very close to 5 cm and the two surfaces were smooth and approximately parallel. The sample was supported by a 3-mm-thick transparent glass plate and set within a housing to hold the sample and detector probe in fixed positions. A schematic of the experiment setup is shown in Fig. 6.1. The entire housing was mounted on a laboratory bench. Once the sample was placed in the housing, it was not moved for the duration of the experiment.

The sample was illuminated with a collimated light source consisting of a 500 watt incandescent bulb mounted in a hemispherical reflector with a glass faceplate. The lamp was placed approximately 3 meters horizontally from the sample. By placing the light source as far from the sample as possible within the cold room, the sample surface presented a small solid angle to the incident light. This ensured that light reaching the sample was approximately collimated. A mirror set at a 45° angle reflected the light

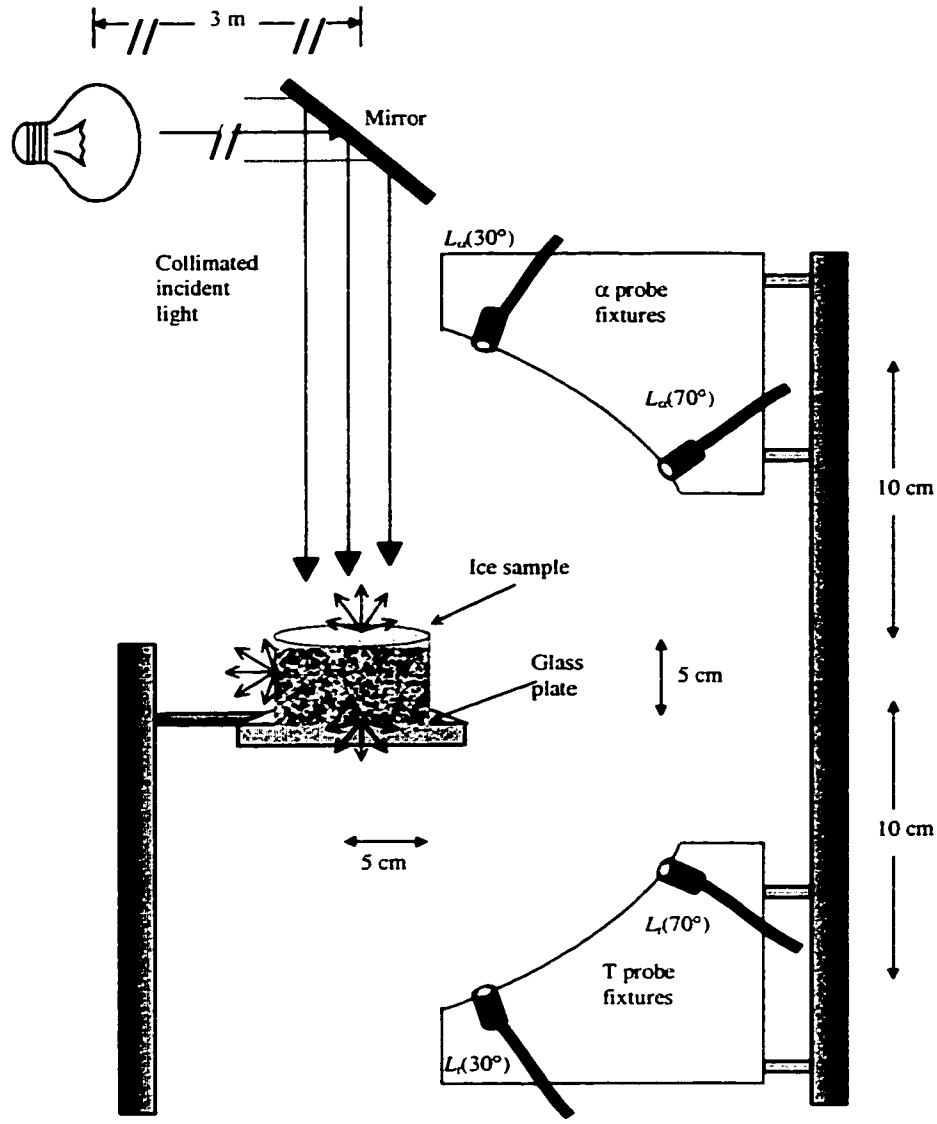

Figure 6.1. Schematic of the optical experiment in the laboratory coldroom.

vertically downward onto the top surface of the sample. Black baffling was used to reduce stray light within the housing and on the sample surfaces.

Measurements of diffuse light backscattered and transmitted by the sample were made using a fiber optic probe which could be positioned at each of the 4-stream, Gaussian quadrature angles (30.6° and 70.1° from zenith and nadir). The probe was

attached to a Spectron Engineering spectrophotometer (Model SE 590), which recorded light at wavelengths between 400 and 1000 nm with approximately 3 nm spectral resolution. A personal computer was used to sample and record the spectrophotometer output. The fiber optic probe was designed to have a narrow field of view so that it could be used to monitor radiance. Unlike a hemispherical cosine collector, the radiance probe could monitor light backscattered from the sample without shading the sample surface from incident light. All optical measurements were relative; no effort to make absolute radiometric calibrations was made.

6.1.1 Sample Size

Ideally, ice samples should be as uniform as possible. Because natural sea ice is subjected to variable growth rates and large temperature variations, it can exhibit large vertical gradients in its structural properties. For this reason, we wanted samples thin enough that, when kept isothermal, they would have approximately uniform vertical properties. At the same time, we needed samples thick enough that sufficient multiple scattering would be present and the apparent optical properties would not be dominated by the effects of sample boundaries.

We used results from the Monte Carlo model to help select the appropriate value of H for our samples. Figure 6.2 (a) shows modeled diffuse components of the backscattered, transmitted, and sidewelling irradiances at $\lambda = 500$ nm as a function of sample thickness, computed for a domain with $\sigma = 0.25$ mm^{-1}, $g_{HG} = 0.95$, and radius 5 cm. As in Chapter 5, we chose IOPs based on work by Mobley et al. (1998). Backscattered and transmitted irradiances were computed at the center of the top and bottom surfaces, while the sidewelling irradiance was computed at $H/2$. Results indicate that the diffuse component of the transmitted irradiance increased as the sample thickness initially increased, then began to decrease when H exceeded 2 cm. This was because this calculation did not include the contribution from the direct beam, which is very large when $H < 2$ cm. From the transmissivity results, we conclude that samples should be thicker than 2 cm, but less than 20 cm where the transmitted irradiance

becomes small and difficult to detect. For measurements of backscattering, the results suggest that H should be at least 5 cm.

Figure 6.2 (b) shows how energy entering the sample with a wavelength of 500 nm is partitioned between energy leaving the sample through the top, bottom, and side surfaces and energy that is absorbed within the sample. This calculation was done by spatially integrating backscattered, transmitted, and sidewelling irradiances over each surface. The amount of energy leaving the bottom and side surfaces is very sensitive to sample thickness. As H increases above 5 cm, the fraction of energy lost through the side walls exceeds 35%. Since the objective is to have as large a signal as possible at the top and bottom surfaces, energy balance considerations require that the sample be as thin as feasible. A sample thickness of 5 cm was finally selected because it best satisfies the above constraints.

Experiments were also carried out to determine whether the effect of side wall losses could be mitigated by placing a highly-reflective collar around the circumference of the sample. No additional sensitivity was achieved in the optical measurements when the sample was placed in the collar. This arrangement also involved the additional complication of needing to model the uncertain optical properties of the collar. For these reasons, we decided not to place such a collar around the sample.

6.1.2 Radiance Probes

Radiances were measured at four angles and are denoted by $L_\alpha(30°)$ and $L_\alpha(70°)$ for the backscattered field at 30° and 70° from normal, and $L_t(30°)$ and $L_t(70°)$ for the transmitted field at 30° and 70°. To avoid intercalibration of multiple probes, we designed the experiment so that a single fiber optic probe could be repeatably positioned into fixed probe holders at the four measurement angles (see Fig. 6.1). A glass bundle fiber optic cable was used to transmit light from the sample to the spectrophotometer. Glass bundles have higher transmittance across a broader wavelength band than plastic fibers and hold up well in a laboratory environment, even at low temperatures.

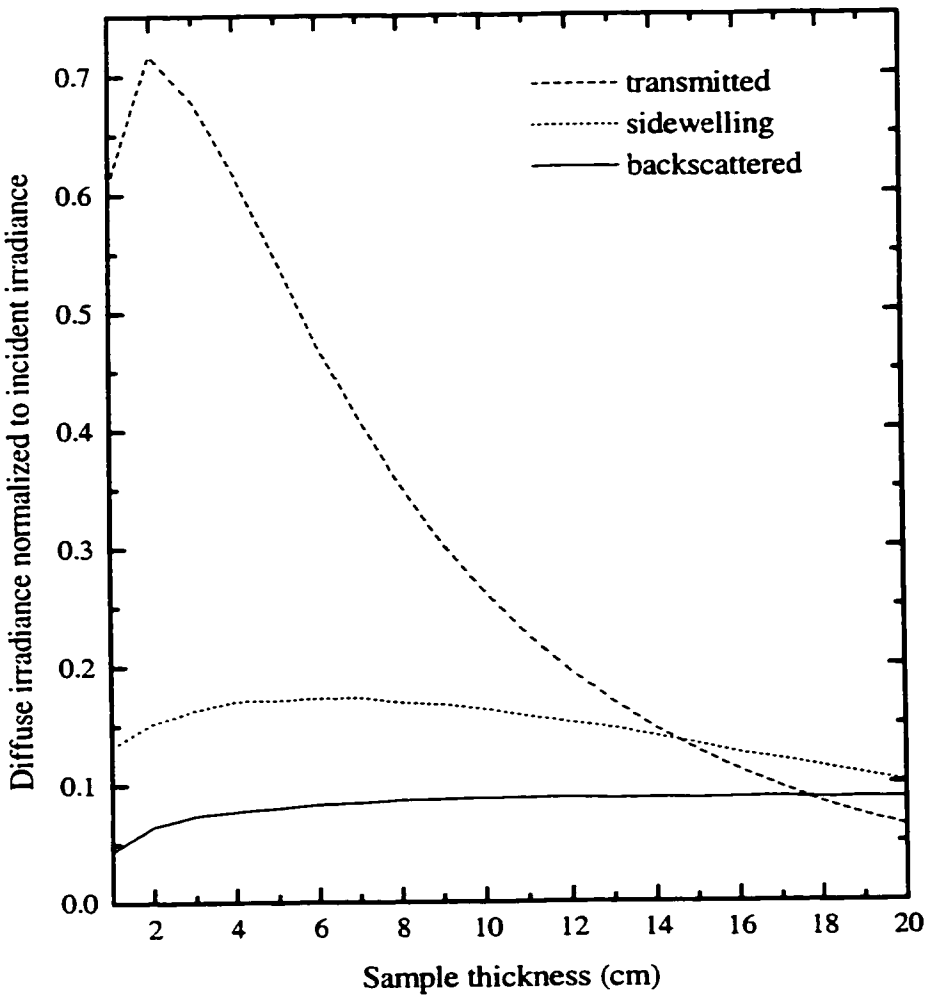

Figure 6.2. Model calculations at 500 nm for a 5-cm-radius cylinder with scattering coefficient = 0.25 mm^{-1} and Henyey-Greenstein asymmetry parameter = 0.95 showing (a) diffuse transmitted, backscattered, and sidewelling fields, and (b) energy losses from sample as a function of sample thickness. Energy losses are integrated over each surface and normalized to energy gain at top surface.

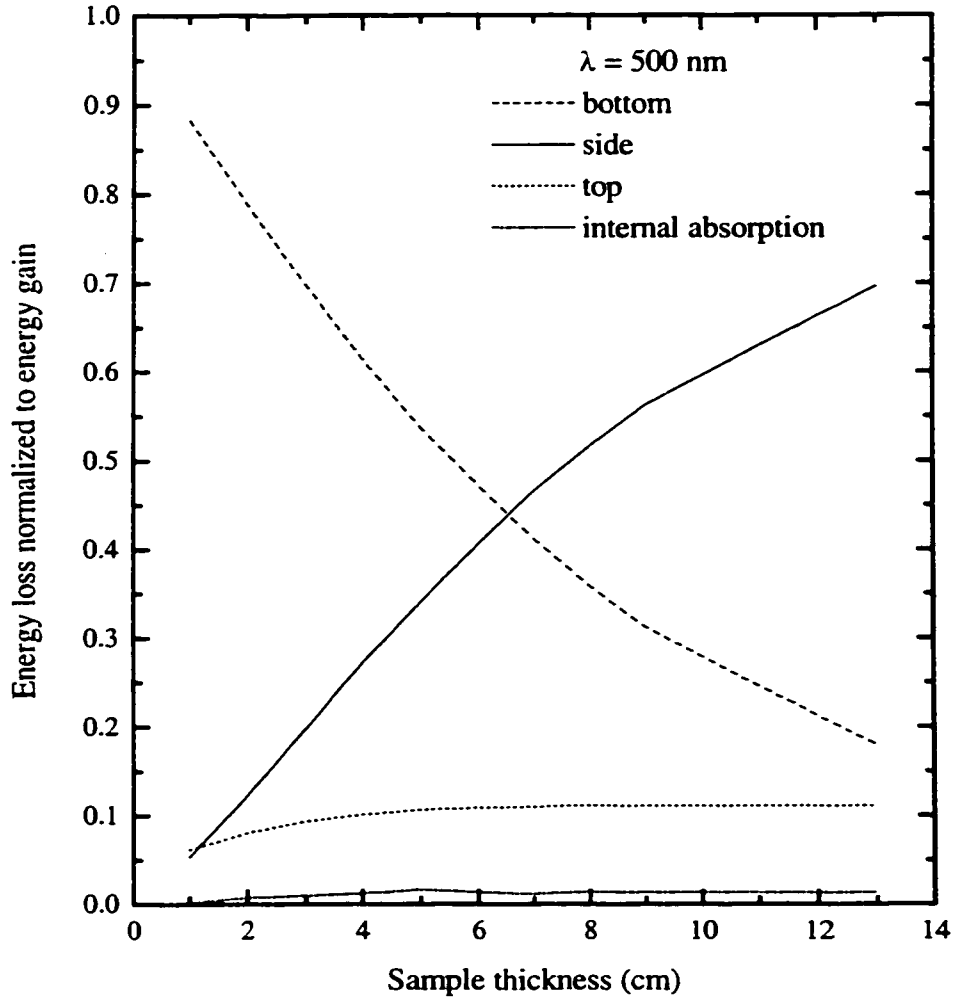

Figure 6.2 continued

Because the glass fiber is a bundle of individual waveguides, its aperature is large. It was also necessary to mount the probe holders at least 10 cm from the sample surface to prevent shading the surface when backscattered radiance measurements were made at 30°. As a result of the large acceptance angle and the minimum sample-to-probe distance, the probe footprint was larger than the sample surface. To remedy this, the end of the radiance probe was fitted with a black plastic tube that held a collimating lens

12 mm in diameter with a 36 mm focal length (Fig. 6.3). The collimating lens reduced the footprint size so that it fit entirely on the sample surface when positioned at 30° and 70°. The probe holders were aligned by placing the probe in each holder and illuminating the opposite end of the fiber. This produced a spot of light on the sample with the same angular extent as the field of view of the probe. Because of certain physical limitations of the housing, it was necessary to adjust the $L_t(70°)$ probe holder to a viewing angle of 67°, so that it deviated approximately 3 degrees from the Gaussian quadrature angle.

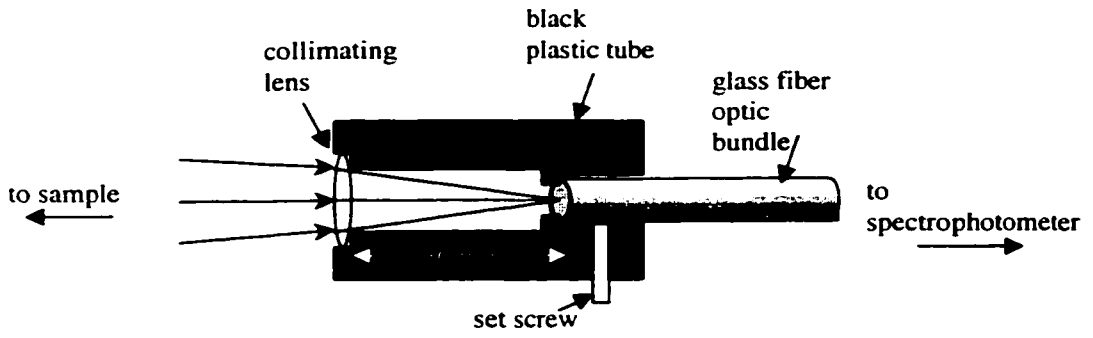

Figure 6.3. Schematic of the lens holder attached to the moveable fiber optic probe.

6.2 Calibrations

Although the experiment was only designed to obtain relative values, several simple calibrations were required.

6.2.1 Glass Plate Absorption

Since the sample rested on a glass plate, light exiting the bottom of the sample suffered a refraction and some additional absorption before reaching the transmission detector. In order to model the optical effects of this glass plate, information was needed on the spectral refractive index and absorption coefficient of the glass ($\kappa_{glass}[\lambda]$). The refractive index of the glass was taken to be 1.5 at all wavelengths (Hecht, 1987). The value of $\kappa_{glass}(\lambda)$ was estimated in the laboratory by making a spectral measurement

of broadband light reflected off a diffuse target with and without the glass plate. The Monte Carlo radiative transfer model was then used to match the measured spectral transmissivity and infer $\kappa_{glass}(\lambda)$ (Table 6.1).

Table 6.1. Spectral absorption coefficients ($\kappa_{glass}[\lambda]$) for glass plate used to support sample.

Wavelength (nm)	$\kappa_{glass}(mm^{-1})$
500	~ 0.0
600	0.0077
700	0.0273
800	0.0441
900	0.0588
1000	0.0750

6.2.2 Alignment of Incident Light Source

It is important that the collimated beam strike the sample normal to the sample surface. Radiance measurements made when test samples were illuminated with an off-axis beam showed considerable discrepancy when compared with model radiances. In a horizontally infinite slab we would not expect small changes in the direct incidence angle to produce large changes in albedo and transmissivity; however, when a sample bounded by side walls is illuminated with off-axis radiation, interactions between the direct beam and these walls must be accounted for. An International Light (IL) 1700 broad band photometer was used to align the incident light source. A cosine collector coupled to the IL detector was placed in the housing at the location of the top surface of the sample, facing straight up. The positions of the mirror and the source were then adjusted to normal incidence, producing maximum signal at the IL detector.

6.2.3 Radiance Probes

Since absolute radiometric measurements were not necessary, observed radiances (L') were normalized to the incident irradiance to obtain relative radiances (L). The probe assembly was calibrated using a broad-band diffusely reflecting target made of Spectralon®, a material with precisely known albedo ($\alpha_{cal} = 0.99$ at visible

wavelengths). The calibration target was placed under the incident beam just above the sample. We first calculated a raw albedo α' by measuring the radiance backscattered from the target $L'_{cal}(30°)$ and $L'_{cal}(70°)$ and then applying a Gaussian quadrature. This value was next corrected using a calibration factor $f = \alpha_{cal}/\alpha'$ which could be determined from the following relationship:

$$\alpha_{cal} = \int_{\Omega} L d\Omega \equiv 2\pi \sum_{i} a_i \mu_i L_i = 2\pi f [0.347 \cdot 0.8611 \cdot L'_{cal}(30°) + 0.652 \cdot 0.340 \cdot L'_{cal}(70°)],$$

where the a_i and μ_i are Gaussian quadrature coefficients and cosines respectively and Ω is the azimuthal coordinate. Noting that the measured $\frac{L'_{cal}(70°)}{L'_{cal}(30°)}$ was found to be 0.796 at all wavelengths for this particular calibration target, we can simplify the above equation to obtain

$$f = \frac{2.104}{2\pi} \frac{\alpha_{cal}}{L'_{cal}(30°)}.$$

If the radiance distributions from the calibration target and the ice sample are diffuse and can be represented with a 2nd order polynomial, it follows that

$$L(\theta) = f L'(\theta)$$

at each of the quadrature angles. This calibration factor includes effects of the probe optics, the experiment geometry, and the incident irradiance normalization.

Another correction was made to account for the difference in distance between the probe and the surfaces of the calibration target and ice sample. The radiance recorded when the calibration target was on top of the sample was 1.04 times the radiance recorded when the target was placed at the location of the sample surface. Since all calibration measurements were made with the target above the sample, the measured value of $L'_{cal}(30°)$ was divided by this factor.

Each time optical measurements were made, the calibration target was initially positioned over the sample and $L'_{cal}(30°)$ recorded. The target was then removed and $L'_{\alpha}(30°)$, $L'_{\alpha}(70°)$, $L'_{t}(30°)$, and $L'_{t}(67°)$ were measured. The probe was also used to measure sidewelling radiance $L'_{s}(90°)$ normal to the core side wall at three hand-held

azimuthal positions. When this sequence of measurements was completed, the target was replaced and a second calibration measurement made to verify the stability of the source during the measurement sequence.

6.3 Optical Properties of First-Year Ice at –15 °C

To corroborate the structural measurements of first-year ice made at –15 °C, the optical properties of the ice were also initially measured at –15 °C. Observed spectral radiances of the cylindrical sample are shown in Fig. 6.4. The largest values were observed for the transmitted radiances $L_t(30°)$ and $L_t(67°)$, while the magnitudes of $L_\alpha(30°)$, $L_\alpha(70°)$, and $L_s(90°)$ were considerably smaller. This is consistent with the calculations of the diffuse irradiance for a 5-cm-thick sample shown in Fig. 6.2 (a). The error bars show the standard deviation of a series of repeated radiance measurements. This variability was largely due to random errors associated with the positioning of the probes within the holders. This test was not sensitive to inaccuracies in the geometry of the apparatus, or to the effects of a non-normal incident irradiance. The largest percentage variability occurred in the measurements for $L_t(67°)$ where the error was estimated to be ± 4%. This is due to the combination of a loose fitting probe holder and the sensitivity of $L_t(67°)$ to viewing angle. The other probe positions had errors less than or equal to 2% at all wavelengths.

Since there are no inverse radiative transfer models for a cylindrical domain, the Monte Carlo model was used to link the observed apparent optical properties to inherent optical properties. As discussed in Chapter 5, it is possible to reduce the two independent IOP variables σ and g to a single variable, s, the similarity parameter. Values of $L_t(30°)$, $L_t(67°)$, $L_\alpha(30°)$, $L_\alpha(70°)$, and $L_s(90°)$ were computed from the Monte Carlo model for 30 values of s between 0.05 and 0.09 at λ = 500, 600, 700, 800, 900, and 1000 nm. For g = 0.95, this corresponds to scattering coefficients between 0.383 and 0.118 mm^{-1}, a range which includes the previously inferred IOPs for sea ice (Mobley et al., 1998; Light, 1995). The objective of these calculations is to infer the

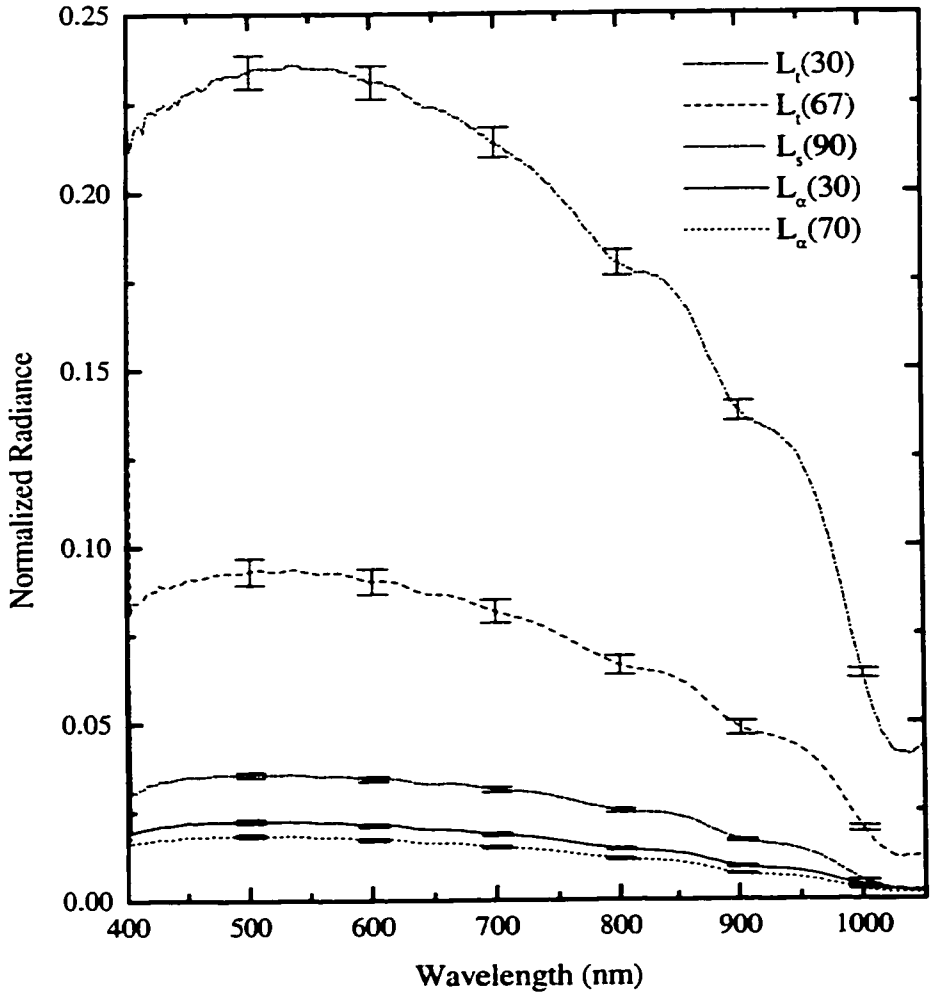

Figure 6.4. Observed transmitted, backscattered, and sidewelling normalized radiances at –15 °C for a cylindrical sample of first-year ice with height and radius of 5 cm. Error bars are shown at wavelengths of 500, 600, 700, 800, 900, and 1000 nm.

value of s whose predicted AOPs best matched those that were observed. Once s is inferred, it will be compared with IOPs derived directly from structural observations.

For the model calculations, the ice sample was represented as a single layer with uniform IOPs. A second layer was used to represent the glass plate. The ice was assumed to be free of absorbing impurities, and to have the spectral absorption coefficient of pure ice. The dependence of modeled radiances on s was parameterized

with third-order polynomials. This smoothed the model output and provided analytical expressions for L as a function of s. High resolution L–s grids were then constructed by evaluating the third-order polynomials for $s = 0.05$ to 0.09 at intervals of $\Delta s = 0.0001$. Figure 6.5 shows modeled radiances and their polynomial fits for (a) $L_t(30°)$, (b) $L_t(67°)$, (c) $L_\alpha(70°)$, (d) $L_\alpha(30°)$, and (e) $L_s(90°)$ at $\lambda = 500$, 600, 700, and 800 nm.

Because the minimum absorption for ice occurs at approximately 470 nm, the results at 500 nm are generally more sensitive to changes in scattering then values computed at other wavelengths. Although model values were also computed at $\lambda = 900$ and 1000 nm, only the four shorter wavelengths were used to infer the IOPs. The radiances are not sensitive to scattering at these longer wavelengths. The sensitivity of radiance to s is greatest for $L_t(30°)$ and $L_t(67°)$. However, both transmitted radiances lose sensitivity for certain values of s, and become non-unique. For $L_t(30°)$ this occurs when $s \geq 0.07$, while for $L_t(67°)$ it occurs when $s < 0.065$. The side and backscattered radiances are generally not as sensitive to changes in s, but they maintain their uniqueness throughout the range of s from 0.05 to 0.09.

As a first step in determining an average value of s for the sample, we inferred individual values from each radiance quantity: $L_t(30°)$, $L_t(67°)$, $L_\alpha(30°)$, $L_\alpha(70°)$, and $L_s(90°)$. This was done by tabulating the square of the percentage difference between computed radiance and observed radiance for each value of s in the high resolution grid. The value of s corresponding to the minimum difference was then selected by searching the grid for the smallest value of ψ

$$\psi_i = \sum_\lambda \left(\frac{L_i(\lambda) - \tilde{L}_i(\lambda)}{L_i(\lambda)} \right)^2 ,$$

where i represents a particular radiance, $L_i(\lambda)$ its observed value at wavelength λ, and $\tilde{L}_i(\lambda)$ the corresponding model value.

Figure 6.6 compares observations and model calculations for $L_t(30°)$, $L_t(67°)$, $L_\alpha(30°)$, $L_\alpha(70°)$, and $L_s(90°)$ using optimized values of s for each radiance. While the spectral agreements are excellent, the results suggest s values between 0.0525 and

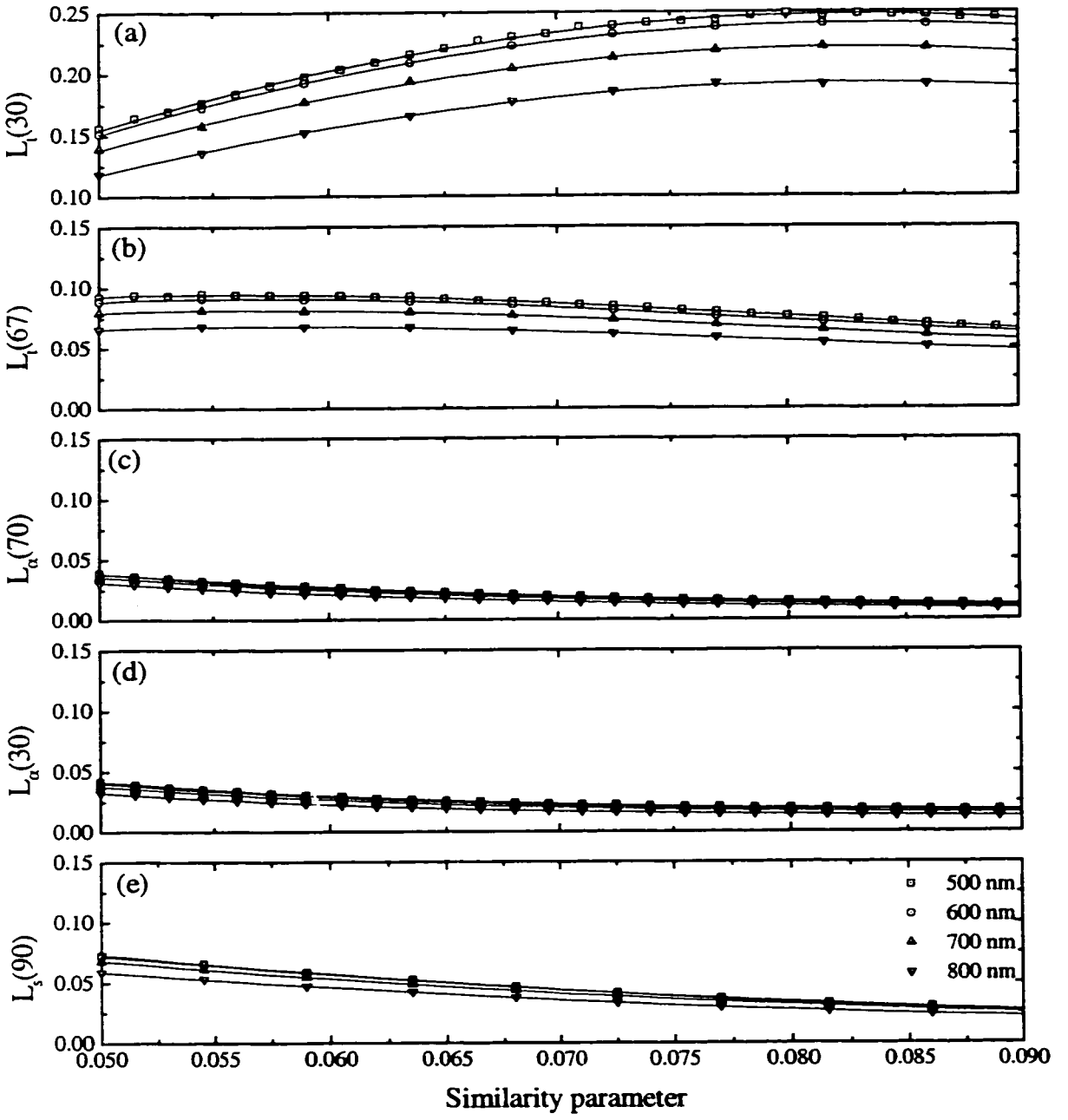

Figure 6.5. Modeled radiances for the sample domain as a function of similarity parameter, s. The panels show (a) $L_t(30°)$, (b) $L_t(67°)$, (c) $L_\alpha(70°)$, (d) $L_\alpha(30°)$, and (e) $L_s(90°)$. Curves represent values at 500, 600, 700, and 800 nm.

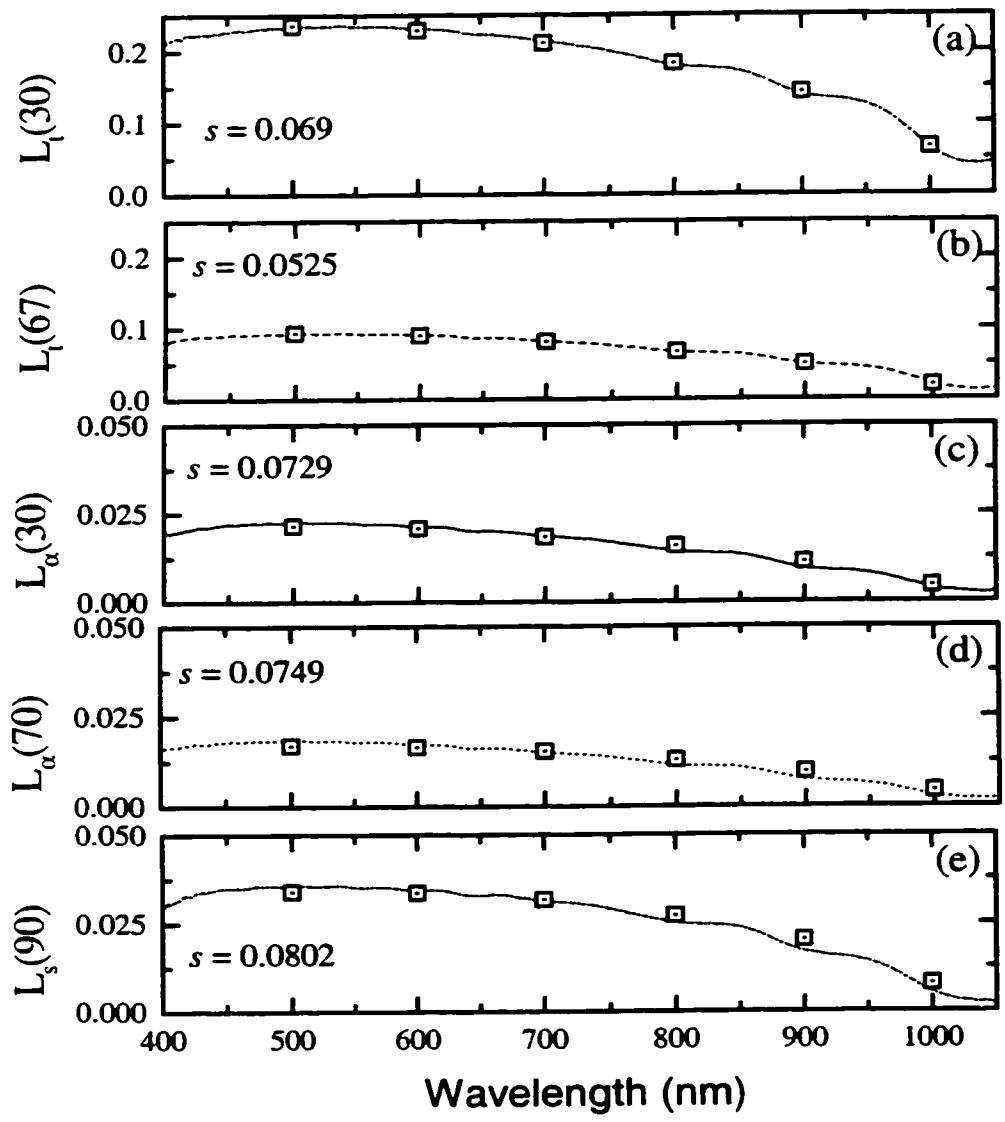

Figure 6.6. Comparison of observed and modeled radiances at –15 °C using optimal values of s: (a) $L_t(30°)$, (b) $L_t(67°)$, (c) $L_\alpha(70°)$, (d) $L_\alpha(30°)$, and (e) $L_s(90°)$.

0.0802, a large spread. To try and understand the reasons for this spread, let us look more closely at the individual radiances. The repeatability measurements indicated the uncertainty in $L_t(67°)$ was larger than for other radiances, yet this test likely did not fully assess the problem with the loose probe holder. The s inferred from the $L_t(67°)$ data is also smaller than 0.065, the lower limit to the sensitive region of $L_t(67°)$. For

these reasons, it does not appear likely that $L_t(67°)$ data can be used to obtain a reliable estimate of s. Likewise, the inference that $s = 0.069$ based on $L_t(30°)$ at –15 °C is questionable for similar reasons. Figure 6.5 suggests that inferences from $L_t(30°)$ should not be used when s is 0.07 or larger. The best values appear to be those derived from $L_\alpha(30°)$ and $L_\alpha(70°)$ which, when averaged, give a value of $s = 0.0739$ at –15 °C.

6.4 Temperature-Dependent Results

An extensive series of measurements were then carried out to examine the effect of temperature on the optical properties of the ice sample. The ice was first cooled from –15 to –33 °C, then progressively warmed to –0.5 °C. During the cooling sequence, AOP measurements were made at –15, –20, –25, and –33 °C. The warming sequence followed with measurements at –21, –15, –11, –7, –5, –4, –2, –1, and –0.5 °C. Measurement procedures and data analysis were the same as those described in the preceeding section. Figure 6.7 shows observed spectral $L_t(30°)$ values at –15, –25, –33, –21, –15, –5 and –1 °C. These spectra, along with those measured at intermediate temperatures, were then used to infer $s(T)$. At low temperatures, the transmissivity was low as a result of the large scattering induced by the presence of precipitated hydrohalite. At higher temperatures, the transmitted radiances were surprisingly constant, suggesting that the IOPs were not changing very much, or that measured values of $L_t(30°)$ were large enough to be insensitive to changes in s (Fig. 6.5 [a]).

Figure 6.8 shows observed values of $L_\alpha(30°)$, $L_\alpha(70°)$, and $L_t(30°)$ at $\lambda = 500$ nm for the entire temperature sequence. For all three radiances it is apparent that at low temperatures the transmissivity decreases, while backscattered radiances increase in response to greater scattering. As the temperature increases between –15 and –7 °C, there is little change in any of the radiances. Above –5 °C, the backscattered radiances indicate a modest, but gradual increase in scattering. Lines and arrows were used to indicate the temporal sequence of measurements in the figure and do not imply continuous measurements.

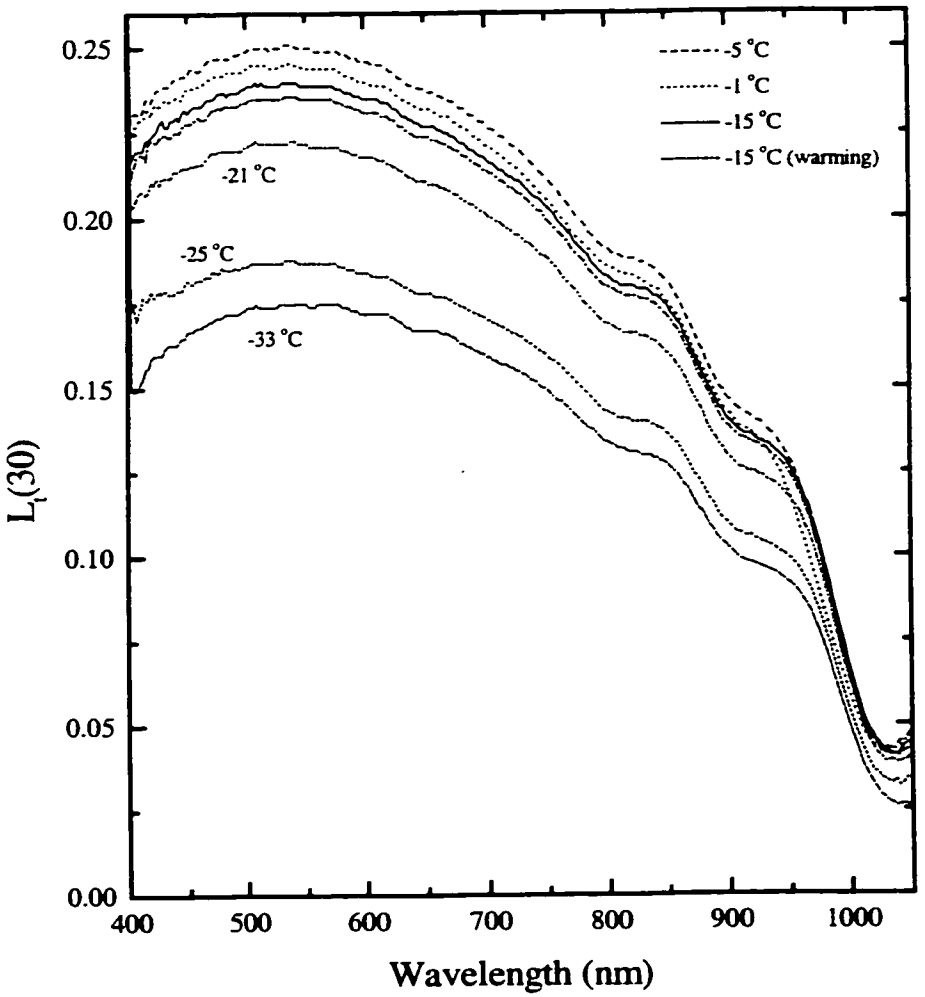

Figure 6.7. Spectral values of $L_t(30°)$. The temperature and inferred s value is indicated for each curve.

Figure 6.9 shows temperature-dependent values of (a) s and (b) σ inferred from $L_\alpha(30°)$, $L_\alpha(70°)$, and $L_t(30°)$. Error bars were computed by propagating the estimated experimental errors through the minimization procedure. The scattering coefficient was computed assuming $g = 0.97$. It was necessary to increase g from 0.95 to 0.97 for reasons to be discussed in detail in Sec. 6.5. All of the inferences show the same trend during the cooling sequence. As hydrohalite precipitates, scattering in the ice increases. The backscattered radiances show this, but not as strongly as the transmitted radiance. In the hydrohalite regime, where the sample optical depth is large, backscattered radiances are composed primarily of energy that has not penetrated very deeply into the

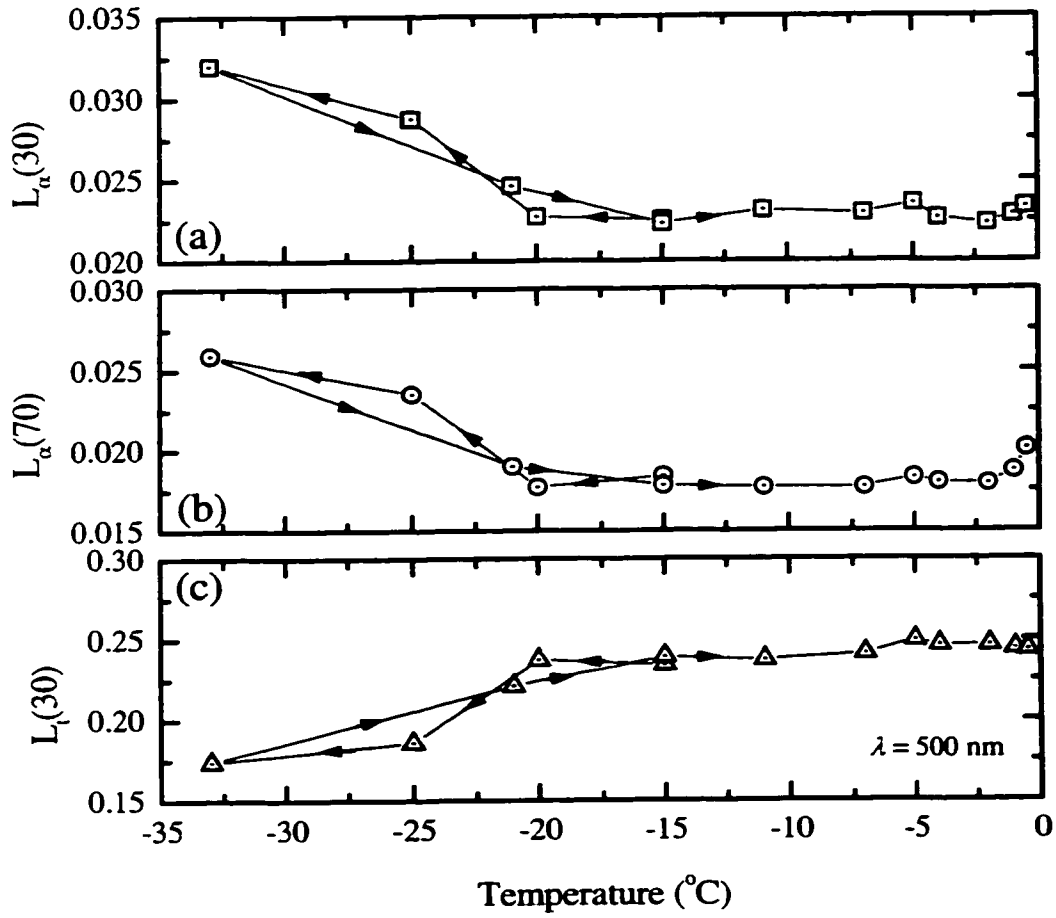

Figure 6.8. Observed values of (a) $L_\alpha(30°)$, (b) $L_\alpha(70°)$, and (c) $L_t(30°)$ at 500 nm as a function of sample temperature. As indicated by the arrows, each temperature sequence begins at –15 °C and cools to –33 °C before warming.

ice. It is possible, then, that the backscattered radiances could be affected by structural inhomogeneities within the upper portions of the sample. For the case of small s (large scattering), $L_t(30°)$ would seem to provide a much more reliable measure as radiation reaching this probe has been transmitted through the entire thickness of the domain.

At higher temperatures, the uncertainty of s associated with $L_t(30°)$ is large. This is due to the lack of sensitivity of $L_t(30°)$ to changes in scattering when $s > 0.07$. As in the data at –15 °C, inferences derived from the backscattered radiances appear to be more reliable as the scattering becomes smaller.

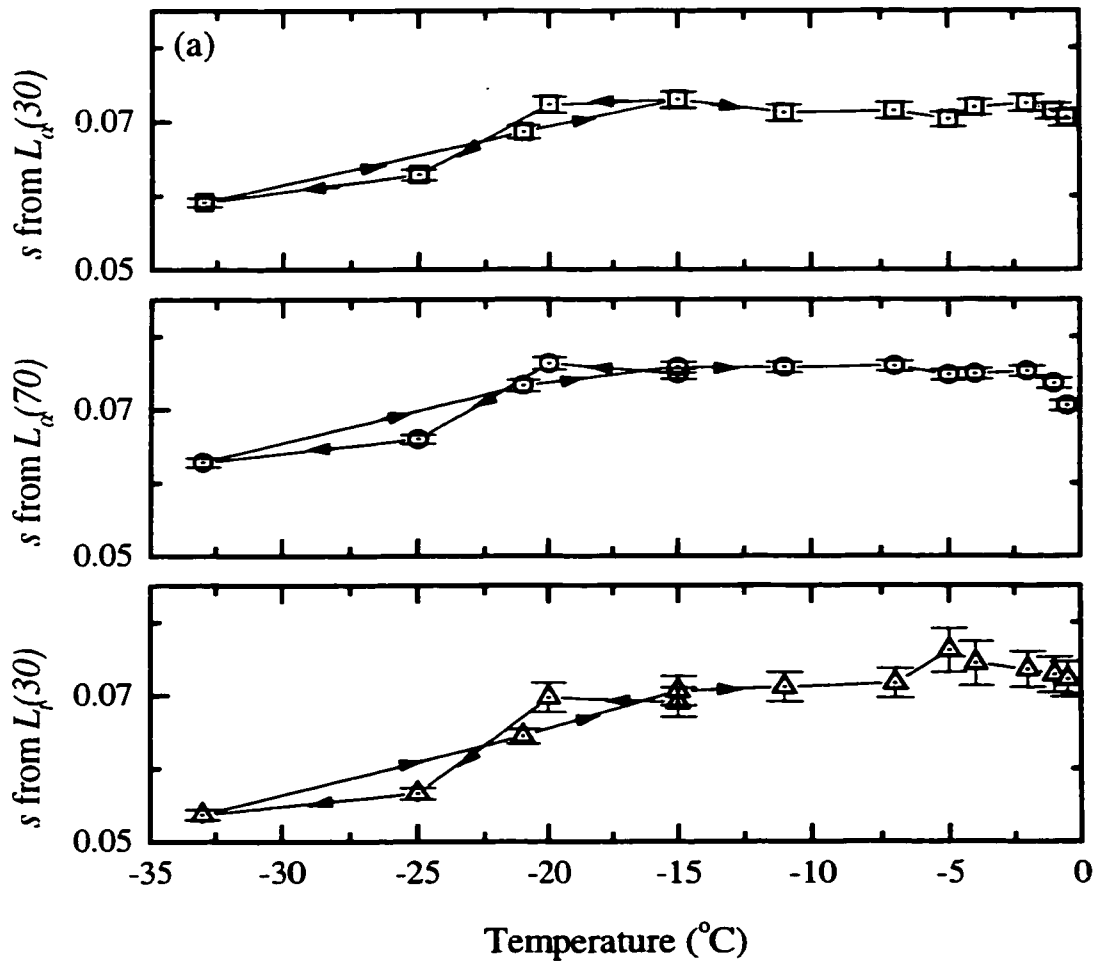

Figure 6.9. Inferred values of (a) s and (b) σ (mm^{-1}) as a function of temperature. Values are directly inferred from $L_\alpha(30°)$, $L_\alpha(70°)$, and $L_t(30°)$. The scattering coefficient is computed assuming $g = 0.97$. Estimated experimental errors are indicated for each measurement.

We used these arguments to estimate $\sigma(T)$. At the lowest temperatures measured, the two backscattered radiances may have been compromised by physical property inhomogeneities within the domain. At higher temperatures, the reduced sensitivity of the transmitted radiance to changes in scattering makes inferences based on $L_t(30°)$ less reliable. For these reasons, σ was calculated using s values inferred from $L_t(30°)$ at the three lowest temperatures (–25 , –33, and –21 °C) and from $L_\alpha(30°)$ and $L_\alpha(70°)$ at all other temperatures.

The resulting composite profiles of $s(T)$ and $\sigma(T)$ are shown in Fig. 6.10. $s(T)$ was inferred from $L_t(30°)$ at points c, d, and e, and from the average of $L_\alpha(30°)$ and $L_\alpha(70°)$

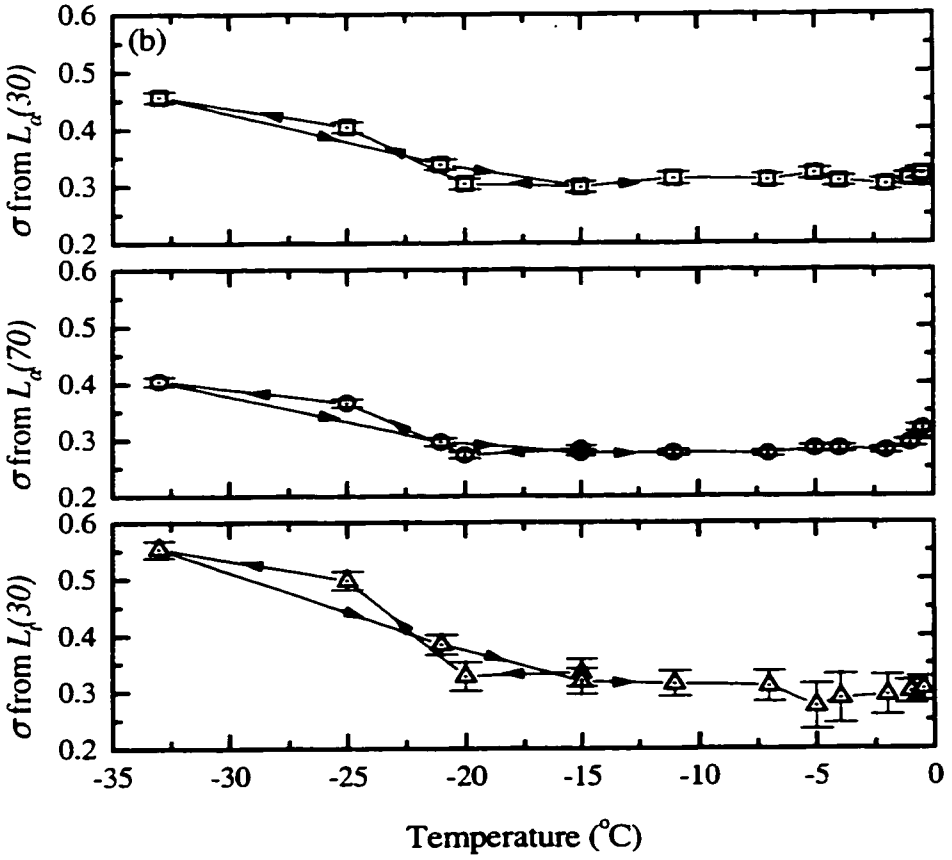

Figure 6.9 continued

at all other temperatures. $\sigma(T)$ was computed assuming $g = 0.97$, as was done in Fig. 6.9 (b). As the ice cooled from –15 to –20 °C (points *a* and *b*), *s* remained approximately constant. But as the ice cooled to –25 and –33 °C (points *c* and *d*), *s* decreased rapidly, indicating a strong increase in scattering due to the precipitation of hydrohalite. Some hysteresis seems to occur as the ice was warmed to –21 °C (point *e*), since the IOPs differ significantly from those recorded at –20 °C (point *b*) during cooling. This may be due to fractionation that occurs as hydrohalite is sequestered within the ice on freezing. When the temperature increases, the hydrohalite is apparently not immediately available to dissolve, retarding the dissolution and melting process. By the time the temperature again passed through –15 °C (point *f*), the scattering was approximately back to its initial value, suggesting that all the hydrohalite

had finally gone back into solution. The magnitude of s then decreased slightly as the ice warmed to –11 °C (point g), and held steady until –7 °C (point h).

At temperatures larger than –15 °C there are several simultaneous processes taking place that affect changes in total scattering. These effects compete in that some of them increase the total scattering, while others decrease it. In warming from –15 to –7 °C, increased brine pocket size and increased refractive index contrast between the mirabilite and the brine tend to increase scattering. On the other hand, dissolution of mirabilite, merging of brine inclusions, and the diminished refractive index contrast between brine and ice tend to decrease scattering. The observations suggest that these effects approximately balance in this temperature range.

As the ice warms to –5 °C (point i), the scattering increases slightly. Further increases in temperature show a slight decrease in scattering (points j and k) between –5 and –2 °C, then a gradual increase between –2 and –0.5 °C. Given the extreme changes in the size and number distributions of the brine and vapor inclusions, the changes in optical properties are surprisingly small. This suggests that there are additional factors which tend to compensate changes in scattering at very high temperatures.

6.5 Discussion

The decrease in s indicated by $L_\alpha(\theta)$ at high temperatures is also supported by the $L_s(90°)$ data. Measurements of $L_s(90°)$ were excluded from the minimization routine, as these radiances were systematically smaller than values predicted by the model. This may be due to the difficulty in preparing a sample with perfectly smooth side walls. The Monte Carlo model treats the side walls as perfectly smooth with Fresnel reflection and refraction occurring relative to the local tangent plane. Imperfect side walls would require the treatment of additional scattering localized at the wall, or a modification on the Fresnel reflection and refraction. At high temperatures, however, the surfaces of the sample became wet with brine from enlarging inclusions. It is likely that this smoothed out some small-scale roughness so that the sidewelling radiance interacted with smoother, more ideal side walls. For this reason, we place some confidence in the side

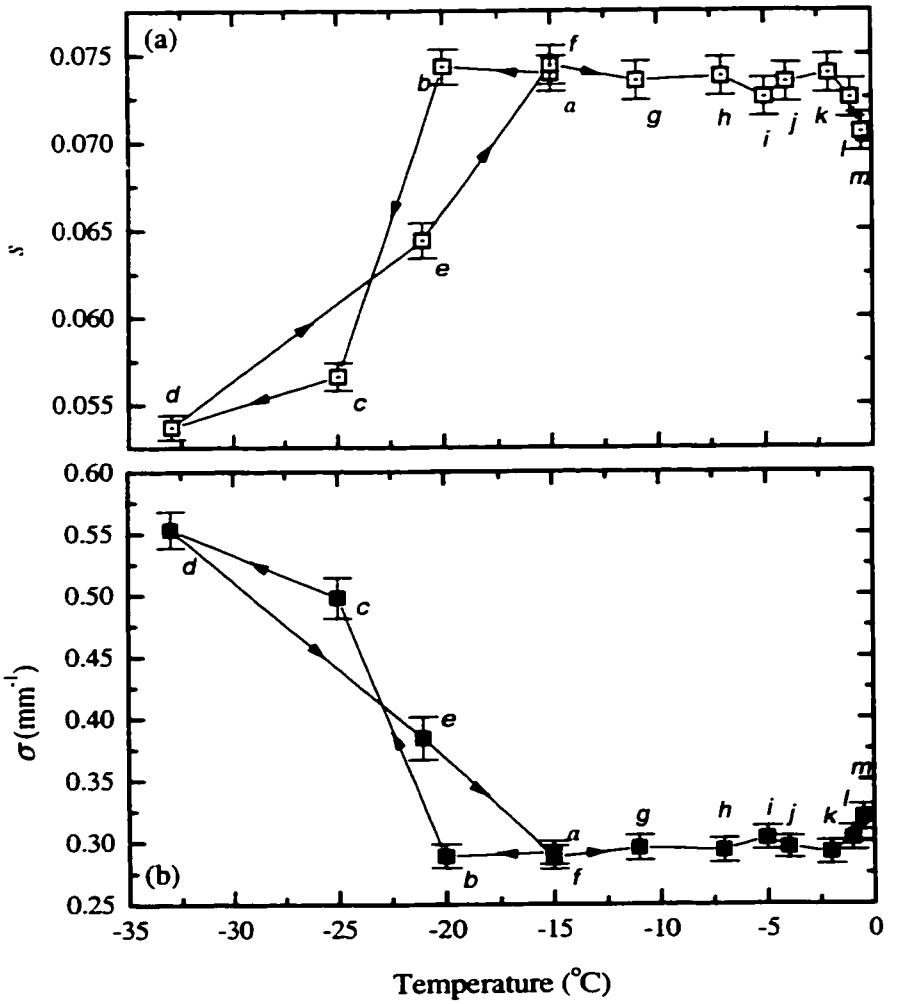

Figure 6.10. Temperature-dependent inherent optical properties for the laboratory sample. The composite $s(T)$ is shown in (a) and the composite $\sigma(T)$ is shown in (b). Individual points are labeled $a - m$ beginning at –15 °C. As in Fig. 6.9 (b) σ is computed assuming $g = 0.97$. Lines connecting points indicate temporal sequence and do not imply continuous measurements.

wall radiance data at high temperatures and note that it corroborates the trend of s decreasing above –5 °C shown in Fig. 6.10 (a).

Because of the close spectral agreement between observed and modeled radiances, it is unlikely the sample contained significant quantities of absorbing impurities. The absorption coefficients for pure ice and water are strongly wavelength dependent, and have well defined minima at approximately 470 nm. This means that an absorber present in the ice would cause scattered light from the sample to have a grayer spectral response than was observed.

While we have attempted to estimate experimental errors and the corresponding uncertainty associated with the inferred IOPs, there are additional uncertainties that could affect the accuracy of these inferences. Tests of the effects of off-axis incident illumination indicated that observed values still fit the modeled spectral quantities quite well, but that this produced a larger spread in inferred s values. This sensitivity is due to the presence of the side walls. The difficulty in establishing and maintaining incident beam alignment could have contributed to the observed spread in s values. The effects of off-axis illumination are, however, difficult to quantify because the present Monte Carlo model has not yet been generalized to treat the case of a non-normal incident beam.

It is also possible that use of a single layer model to represent our sample is an over simplification. Interior first-year sea ice has fewer visible structural gradients than ice from near the surface or bottom of the pack. However, it is still possible that structural inhomogeneities occurring near the surfaces of this sample affect its apparent optical properties. As the temperature approached the melting point, inclusions near the sample surfaces likely drained and could have had significantly different optical properties. Clearly this would dictate the use of multiple horizontal layers in the model to accurately describe the IOPs. Despite small changes that occur in the ice structure, it is clear that our data and the inferred IOPs describe the changes that occur within the bulk of the sample.

To estimate $s(T)$, we relied on the validity of the similarity parameter. The model grid was initially constructed by computing $L(\theta)$ as a function of s with $g = 0.90$. This seemed to be a reasonable approximation (see Fig. 5.10), even though the true value of g was expected to be closer to 0.95. As expected, the s approximation appears to hold for backscattered radiances but was found to break down for near-nadir transmitted radiances. This breakdown occurs because the scattering is highly forward peaked (g approaches 1). As a result, measured $L_t(30°)$ values were larger than those predicted by the model for any s when $g = 0.90$. Model computations for $L_t(30°)$ were then repeated using progressively larger values of g. It was not until g was increased to 0.97 that the modeled s values were large enough to explain the observations . We

conclude then that the minimum g required to describe the ice sample is 0.97. For this reason, $g = 0.97$ was used to compute σ from the inferred values of s (see Figs. 6.9 – 6.10).

This optical data set details the changes that occur in the inherent optical properties of first-year interior sea ice as a function of ice temperature. These inherent optical properties respond to changes in the microstructure of the ice. Microstructural changes include changes in the size and number of brine inclusions and vapor bubbles, changes in the size and number of precipitated salt crystals, and changes in the refractive index contrast between salt crystals, brine, and ice. Many of these changes have been documented in the observations described in Chapter 4. The next chapter will focus on connecting the effects of these structural changes to the optical properties of the ice.

CHAPTER SEVEN
STRUCTURAL-OPTICAL MODEL

The results presented in Chapter 6 describe temperature-dependent changes in the inherent optical properties (IOPs) observed in a sample of naturally-grown, first-year congelation ice. The imagery presented in Chapter 4 provides a quantitative description of the ice microstructure. In this chapter, we will compute IOPs directly from the microstructure observations, and compare these values with the IOPs inferred from the optical measurements. From this structural-optical data set, we will build and test a structural-optical model for first-year sea ice.

All radiative transfer models require basic information about the IOPs of the domain being modeled. A structural-optical model provides this information from the physical properties of the domain. In Chapter 2, the basic equations that relate the fractional volumes and the number and size distributions of scatterers to absorption and scattering coefficients were outlined. This structural-optical model is based on those equations.

7.1 Absorption Coefficient

In Eqn. 2.1, the bulk spectral absorption coefficient was specified as

$$\kappa(\lambda) = \kappa_i(\lambda)\, v_i + \kappa_b(\lambda)\, v_b + \kappa_g(\lambda)\, v_g + \kappa_s(\lambda)\, v_s + \kappa_p(\lambda)\, v_p,$$

where $\kappa(\lambda)$ values give spectral absorption for ice (subscript i), brine (subscript b), gas (subscript g), precipitated salt (subscript s), and particulates (subscript p). The values of v give the fractional volumes of each constituent. For the first-year sea ice used in this study, we take

$$\kappa(\lambda) \sim \kappa_i(\lambda).$$

This approximation can be made when v_p is negligible. Also, we believe the absorption due to precipitated salts is small because v_s is small and we suspect that κ_s is also small and does not exhibit strong spectral variation. Likewise, $\kappa_g << \kappa_i$, so the absorption due to the vapor can be neglected. Finally, $\kappa_b(\lambda)$ is very similar to $\kappa_i(\lambda)$, and v_b rarely exceeds 0.20, so we do not distinguish between the absorption due to the ice and that due to the brine. Since $\kappa_b(\lambda)$ does differ from $\kappa_i(\lambda)$ at some visible wavelengths, the

spectral value of κ could be affected slightly when the brine volume is large at temperatures near 0 °C.

7.2 Scattering Coefficient

To compute the scattering coefficient (σ) from inclusion number and size distributions, it is assumed that individual inclusions scatter independently, such that Eqn. 2.3 is applicable. Because this equation considers scattering by brine inclusions, vapor bubbles, precipitated salts, and particulates, while scattering from the ice lattice itself is considered negligible, it is written as

$$\sigma = \sigma_b + \sigma_g + \sigma_s + \sigma_p.$$

Each term is taken to be independent of wavelength, an assumption good for inclusions much larger than the wavelength. For samples with little particulate mass, σ_p is small and can be neglected.

The individual σ_j are evaluated using Eqn 2.4, which pertains to a size distribution of like scatterers with number density $N(r)$:

$$\sigma_j = \int_{r_{min}}^{r_{max}} Q_{sca}(r)\pi r^2 N(r)dr.$$

Because $N(r)$ was estimated using discrete size bins in Chapter 4, σ_j is computed as the sum of σ_k values for each size bin, where

$$\sigma_k = Q_{sca}(r)\pi r_k^2 N_k. \qquad (7.1)$$

For spherical inclusions, r_k is the average inclusion radius and N_k is the average inclusion number density for each size bin. However, this equation can be difficult to evaluate for inclusions that have a variety of shapes, even when the shapes are idealized as ellipsoids and cylindrical tubes. For this reason, various inclusion shapes are modeled using equivalent volume-to-surface-area ratio spheres. The population of equivalent spheres has approximately the same optical properties as the original inclusions (see Grenfell and Warren, 1999). We will now describe how r_k, N_k, and σ_k are evaluated for each type of inclusion observed in our samples.

7.2.1 Brine Inclusions

Brine inclusions were observed to have a variety of different shapes, including spherical, ellipsoidal, and tubular. We express the total scattering coefficient for all brine inclusions as the sum of scattering coefficients by brine pockets (σ_{bp}) and brine tubes (σ_{bt}).

Ellipsoids

Table 4.1 lists the observed maximum dimension, number density, and average aspect ratio of the brine pockets in the ice sample at –15 °C in each of seven size bins. In each case, the pockets were identified as having aspect ratios between 1 and 5, and were observed to be approximately ellipsoidal. Table 7.1 gives the dimensions of the representative ellipsoid for each bin. This ellipsoid has semi-major axis (c) equal to half of the average maximum dimension listed in Table 4.1. The average aspect ratio is used to compute the semi-minor axes. These inclusions are generally prolate ellipsoids, so their two semi-minor axes are equal.

The population of equivalent spheres is defined as the set of spheres with identical radius (r_{sp}) whose volume-to-surface-area ratio is identical to the volume-to-surface-area ratio of the representative inclusion. The number of equivalent spheres (N_{sp}) is not

Table 7.1. Average semi-major and semi-minor axes, observed number density (N_{bp}), equivalent sphere number density (N_{sp}), equivalent sphere radius (r_{sp}), and scattering coefficient (σ_{bp}) for the brine pockets reported in Table 4.1 at –15 °C.

Bin	Semi-major axis, c (mm)	Semi-minor axis, a (mm)	Average aspect ratio	N_{bp} (mm^{-3})	N_{sp} (mm^{-3})	r_{sp} (mm)	σ_{bp} (mm^{-1})
1	0.0075	0.0075	1	25.47	25.47	0.0075	0.009
2	0.0225	0.0150	1.5	2.21	2.40	0.0167	0.004
3	0.0375	0.0208	1.8	2.29	2.70	0.0240	0.010
4	0.0600	0.0291	2.3	1.52	2.06	0.0298	0.011
5	0.0950	0.0244	3.9	0.66	1.34	0.0302	0.008
6	0.1325	0.0379	3.5	0.55	1.03	0.0467	0.014
7	0.2000	0.0417	4.8	0.22	0.55	0.0521	0.009
					TOTAL		0.066

the same as the number of original inclusions, and is computed by dividing the total volume in the original population by the volume of an equivalent sphere, $\frac{4}{3}\pi r_{sp}^3$ (see Grenfell and Warren, 1999). For the first bin in Table 7.1, the average pocket has aspect ratio equal to 1, so $r_{sp} = a = c$, and N_{sp} is equal to the number of observed brine pockets in the bin. For bin 2, the average ellipsoid has $c = 0.0225$ mm, and aspect ratio 1.5. The volume of a prolate ellipsoid is $\frac{4}{3}\pi a^2 c$, and its surface area is given by $2\pi a(a + \frac{c}{e}\sin^{-1} e)$, where $e = \sqrt{1 - \frac{a^2}{c^2}}$ is the ellipticity (Beyer, 1987). In this case the volume of the representative ellipsoid is 2.12E-5 mm^3 and its surface area is 3.81E-3 mm^2. The sphere with the same ratio has $r_{sp} = 0.0167$ mm, and there are 1.09 equivalent spheres per elllipsoid. The corresponding N_{sp} is 2.40 per mm^3, a value larger than the observed N_{bp}. This will always be the case, as ellipsoids have larger volume-to-surface-area-ratio than spheres, and the additional equivalent spheres are needed to account for the total volume. Scattering coefficients for each bin (shown in Table 7.1) are computed using Eqn. 7.1. The total σ_{bp} for the brine pockets observed at –15 °C is 0.066 mm^{-1}.

Cylindrical Tubes

The brine tubes observed in the samples were also treated as collections of equivalent spheres after Grenfell and Warren (1999). The volume and surface area calculations were done for the 23 observed tubes explicitly, assuming the tubes to be cylindrical. The values of r_{sp} varied between 0.030 and 0.170 mm at –15 °C. The smallest r_{sp} for the brine tubes was larger than all r_{sp} values for the brine pockets, bins 6 and 7 excepted. There were calculated to be between 3 and 31 equivalent spheres per tube. The total σ_{bt} for the 23 tubes was 0.120 mm^{-1}, nearly twice as large the total scattering due to the observed brine pockets.

7.2.2 Vapor Bubbles

The treatment of vapor bubbles is simpler than that for ellipsoidal and tubular brine inclusions because bubbles are already approximately spherical. The values of N_g, r_{sp}, and σ_g for the three size bins of bubbles at –15 °C are shown in Table 7.2. Because all bubbles are assumed to be approximately spherical, $N_g = N_{sp}$. The total scattering coefficient at -15 °C for vapor bubbles is 0.0029 mm^{-1}, less than 2% of the scattering generated by the brine inclusions.

Table 7.2. Observed number density, N_g, equivalent sphere radius, r_{sp}, and total scattering coefficient, σ_g for each of the bins in the vapor bubble size distribution.

Bin	N_g (mm^{-3})	r_{sp} (mm)	σ_g (mm^{-1})
1	0.757	0.0075	0.0003
2	0.246	0.0225	0.0008
3	0.205	0.0375	0.0018
		Total	0.0029

7.2.3 Precipitated Salt Crystals

Lacking observational data on the number and size distributions of the precipitated salts, the temperature-dependent parameterizations developed by Light (1995) were initially used in the calculations. These parameterizations indicate that σ_s for mirabilite in a sample with salinity 4.7 $^{o}/_{oo}$ and effective crystal edge length 9 μm is 0.046 mm^{-1} at –15 °C. Hydrohalite does not begin to precipitate until the temperature of the ice is reduced to –22.9 °C. Light (1995) predicted σ_s for hydrohalite to be 0.439 mm^{-1} at –30 °C for an ice salinity of 4.7 $^{o}/_{oo}$ and effective crystal edge length 8.5 μm.

7.3 Initialization at –15 °C

The structural-optical model was initialized with computed values of $\kappa(\lambda)$ and σ derived from the observations of the ice microstructure at –15 °C. In the course of initialization, it was necessary to adjust the brine inclusion number density so that the entire predicted brine volume was accounted for. In Chapter 4 it was noted that the observed brine inclusions only accounted for about 52% of the predicted brine volume

in the sample. The predicted brine volume of 1.92% is based on an average measured salinity of 4.7 $^{o}/_{oo}$ and the equations of Cox and Weeks (1983). This discrepancy is most likely due to the spatial inhomogeneity in salt content found in congelation ice. Cottier et al. (1999) found small-scale salinity variations up to 5 psu cm^{-1} in samples with a mean salinity of 5.7 psu. Note there is an approximate 1:1 relationship between psu and part-per-thousand in seawater, but they are not exactly equal. It is likely that thin sections used for our structural measurements were biased towards areas where the brine volume was small. Thin sections with areas of large brine volume tended to fall apart easily and were avoided during sample preparation.

We suspect that the missing brine existed in additional brine tubes that were present in the optical sample, but were not observed in the thin section. To compensate for this underestimate, the number density of observed brine tubes was increased from 0.27 to 0.56 mm^{-3}, such that the computed brine volume became equal to the predicted brine volume. Because σ is directly proportional to N_{sp} (see Eqn 7.1), σ_{bt} also increased by a factor of 2.073, to 0.249 mm^{-1}. This revised σ_{bt} is about 3.8 times as large as σ_{bp}, yet, 12.7 times more brine volume is attributed to the tubes. The size distribution for brine tubes remained unchanged, and the population of ellipsoidal brine pockets was not altered.

Because approximately 30% of the observed brine tubes included vapor bubbles, increasing the number of brine tubes should also increase the estimated number density of vapor bubbles. In general, the bubbles observed in the tubes were in the largest of the three bubble size bins. To make this adjustment, the number density of vapor bubbles in this largest bin was increased by 30%, and σ_g was recomputed to be 0.004 mm^{-1}. A summary of the values used to initialize the model at –15 °C is given in Table 7.3.

These calculations only provide information about σ, however, and direct estimates of g are difficult to obtain from samples with multiple scattering. The approach, therefore, was to first calculate σ and $\kappa(\lambda)$ directly, then to infer a value for g based on comparisons with optical data.

Table 7.3. Summary of scattering coefficients used to initialize the structural-optical model at –15 °C.

Inclusion category	Range of r_{sp} (mm)	Total N_{sp} (mm^{-3})	σ (mm^{-1})
All brine pocket bins	7.5E-3 – 0.052	35.56	0.066
Brine tubes	0.03 – 0.17	5.88	0.224
Vapor bubbles	7.5E-3 – 0.038	1.30	0.004
Mirabilite	-	-	0.046

7.4 Temperature-Dependent Scattering

Changes in temperature cause changes in the relative volume of brine, vapor, and precipitated salts. It was initially assumed that brine and vapor inclusion number densities remain constant as the inclusions grow and shrink. For precipitated salts, the total mass of salt was computed at each temperature from the phase relation parameterizations of Cox and Weeks (1983), and the number density adjusted by assuming that the crystal size remained constant. At each temperature, the distributions were adjusted and the scattering coefficient recomputed.

Figure 7.1 shows model predictions of $\sigma_j(T)$ for brine pockets, brine tubes, vapor bubbles, mirabilite, hydrohalite, and total $\sigma(T)$. At temperatures higher than –25 °C, the largest contributor to the total scattering is the population of equivalent spheres associated with the brine tubes. Scattering from all brine inclusions shows a significant drop at temperatures below the initial temperature of hydrohalite precipitation (-22.9 °C), and rapid increases above –5 °C where bulk brine volume is large and increases rapidly with temperature. The scattering coefficient due to vapor bubbles is two orders of magnitude smaller than σ for all brine inclusions.

To compare this initial estimate of scattering with the $s(T)$ inferred from the optical observations, we need to assign a value to g. The comparison between the optical data and the radiative transfer model indicated that a minimum g of 0.97 was necessary (see section 6.5). However, no upper limit was assigned. Because of the large amount of forward scattering by brine inclusions, it is likely that the bulk g for the sample exceeds 0.97. In an effort to match the structural and optical results, the Monte Carlo model was run using the total $\sigma(T)$ inferred from the structural data (Fig. 7.1) and larger values of

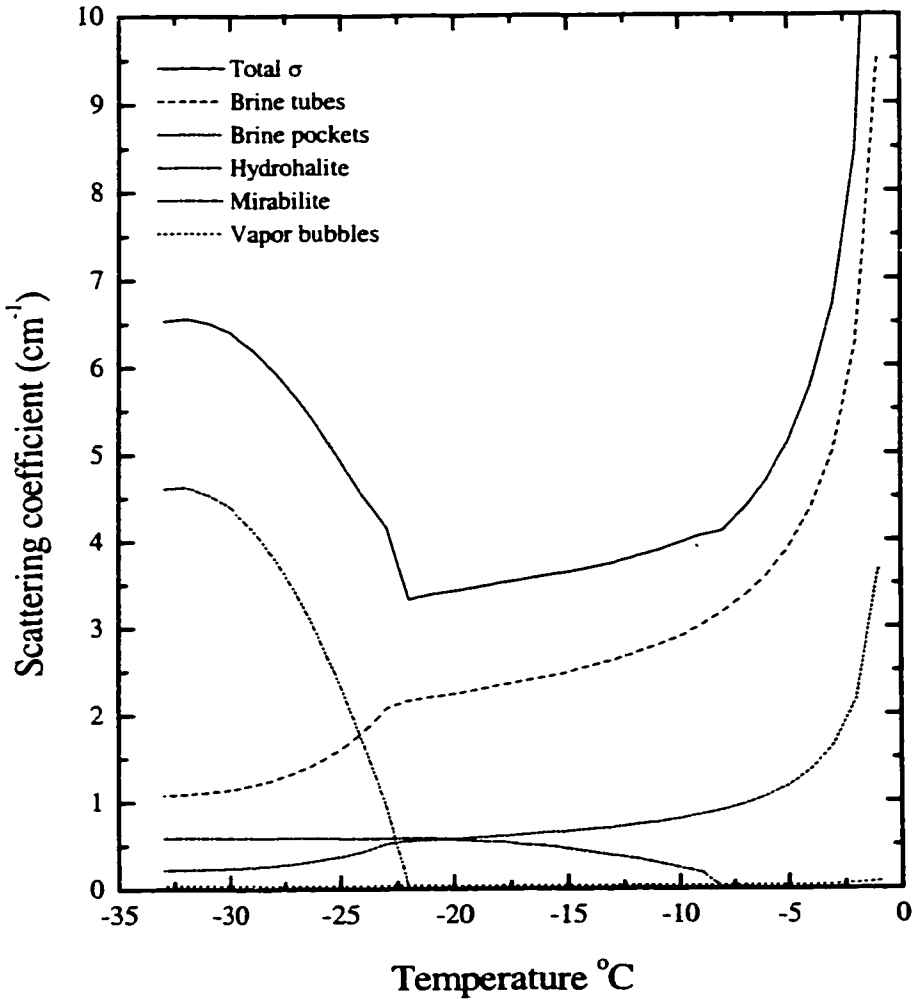

Figure 7.1 Initial temperature-dependent model of the scattering coefficients for brine pockets, brine tubes, vapor bubbles, mirabilite crystals, and hydrohalite crystals. The sum of all scattering coefficients is also shown.

g. The objective was to increase *g* until there was an approximate match between the predicted *s* and the *s* obtained from the optical data at –8 °C. This temperature was selected because it was high enough that appreciable precipitated salts would be absent, yet low enough that extreme changes in brine inclusion distributions had not yet begun to occur. The best match between the two data sets was obtained when *g* was increased to 0.978. An initial comparison between *s* inferred from the optical data and *s* computed from the structural data is shown in Fig. 7.2. More work is clearly needed to resolve the differences, but the agreement at –8 °C is good.

The temperature dependence of $\sigma(T)$ in Fig 7.1 suggests three distinct regimes. Changes in scattering for $T \leq$ -22.9 °C are dominated by changes in the number and possibly size of hydrohalite crystals. Large changes in structure correspond to large changes in the optical properties. In the mirabilite regime (-22.9 °C $< T \leq$ -8.2 °C), $\sigma(T)$ depends on compensating changes in scattering by brine inclusions and mirabilite crystals. As the ice warms through this regime, σ_b increases while σ_s due to mirabilite crystals decreases. Small changes in structure correspond to small changes in the optical properties. In the warm regime ($T >$ -8.2 °C), $\sigma(T)$ increases rapidly in response to large changes in the size of brine inclusions. These large changes suggest that commensurate changes should occur in the optical properties; however, only small changes are observed. In the following section, each of these regimes will be examined in more detail in an effort to refine this structural-optical model.

7.4.1 Refinement of Scattering for the Salt Regimes

Figure 7.2 shows that the scattering predicted by the structural-optical model in the precipitated salt regimes is smaller than the observed scattering. Estimates of $\sigma(T)$ and $s(T)$ predicted by the structural-optical model were improved by changing the way scattering is treated for hydrohalite and mirabilite crystals and by adjusting the effective crystal sizes. We consider the improvements in the two salt regimes individually.

Hydrohalite Regime

Light (1995) computed σ_s and g_s for hydrohalite crystals in brine using the Modified Kirchoff Approximation (MKA) (Muinonen, 1989). In this approximation, the phase function is calculated independently of diffraction so it was appropriate to assume the diffracted energy remains unscattered and to use $Q_{sca} = 1$ when calculating σ_s. The MKA calculations resulted in smaller g values than would have been predicted using Mie theory. However, our microstructural observations suggest that hydrohalite crystals tend to nucleate on ice and may become entrained in the ice as it cools. As a result, the scattering by hydrohalite should be treated for the crystals in ice rather than in brine. When we recomputed the asymmetry parameter for hydrohalite crystals using

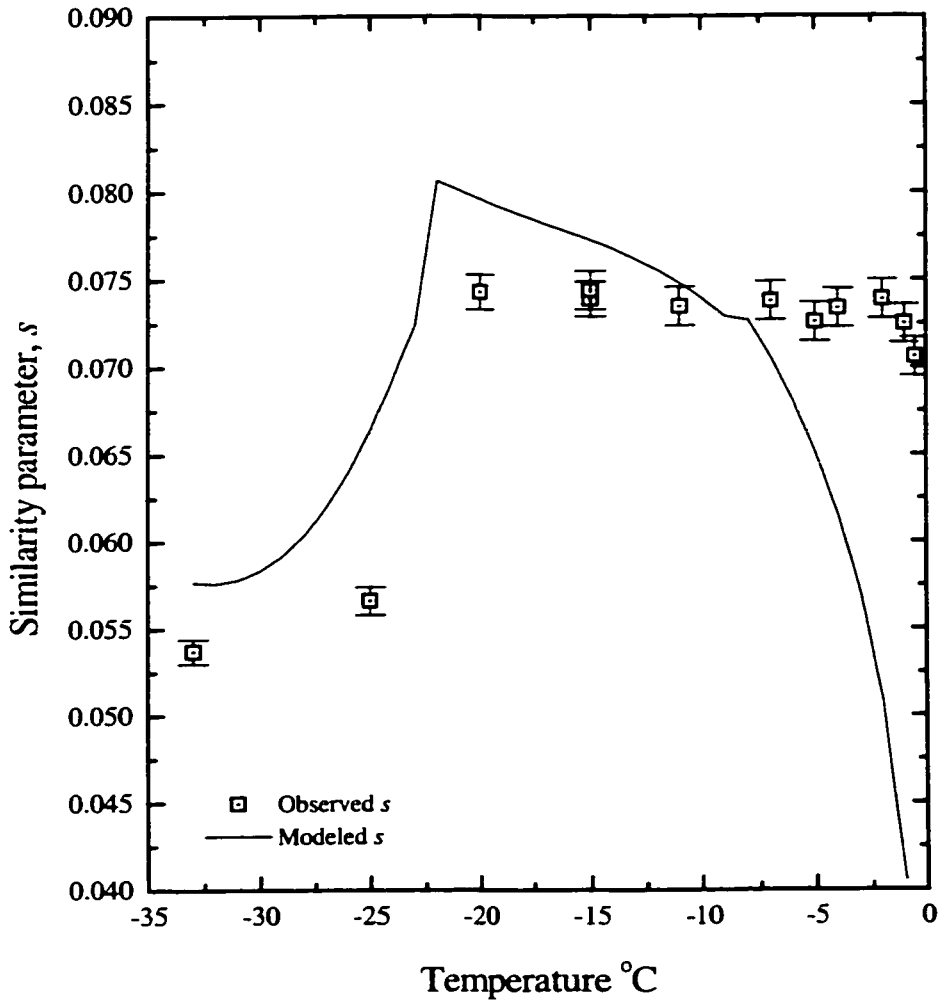

Figure 7.2 Initial comparison of modeled and observed similarity parameter as a function of temperature..

Mie theory, predicted g values were approximately 0.97, and $Q_{sca} = 2$. We then recomputed σ_s and increased the effective crystal edge length from 8.5 to 10 μm at all temperatures.

It was also noted that once the ice is cold enough to precipitate hydrohalite, mirabilite crystals become very inefficient scatterers. In the microstructural observations at temperatures below approximately –23 °C, the boundaries of mirabilite crystals were barely visible. This reduction in scattering is due to the increased refractive index of the brine (n_b) that results from the increasing brine concentration. At –23 °C, the relative refractive index of mirabilite in brine is less than 1.01. At

approximately –29 °C, n_b is equal to the refractive index of mirabilite, 1.396 (Maykut and Light, 1995). At this temperature, g for mirabilite crystals equals unity. We modeled this effect by setting σ_s for mirabilite to zero once the temperature drops below –23 °C. With these two refinements in the model a good fit was obtained at –25 °C (Fig. 7.3).

These changes, however, were still not sufficient to match the observed s at –33 °C, as the predicted scattering became too large at the coldest temperature measured. Several possibilities exist for explaining this overprediction of scattering. We have assumed that the effective crystal size remains constant. If the effective crystal size were permitted to grow as the ice cools, the scattering at the coldest temperatures would be reduced. An effective crystal size for hydrohalite of 14 μm gives good agreement with the data at –33 °C. While it is possible that crystal size could increase with increased precipitation, individual hydrohalite crystals were not visible in the imagery, suggesting crystal sizes generally did not grow larger than 10 μm. On the other hand, it is possible that not all of the hydrohalite precipitates. Clearly the optical observations show that much of it does, but we can not rule out the possibility that there is some supersaturation of hydrohalite within brine inclusions.

Mirabilite Regime

Between –9 and –22.9 °C, the initial treatment predicted less scattering than was observed (Fig. 7.2). Total scattering in this regime is determined by both brine inclusions and mirabilite crystals, and changes in either the scattering coefficient or phase function can be important. However, when a Mie treatment was used ($Q_{sca} = 2$) and the effective mirabilite crystal size increased slightly from 9 to 10 μm, the computed and inferred s values agreed quite well, as shown in Fig. 7.3.

7.4.2 Refinement of Scattering For Warm Regime

At temperatures greater than –8 °C, Fig.7.2 shows that the structural-optical model predicts considerably more scattering than was observed. Clearly some important

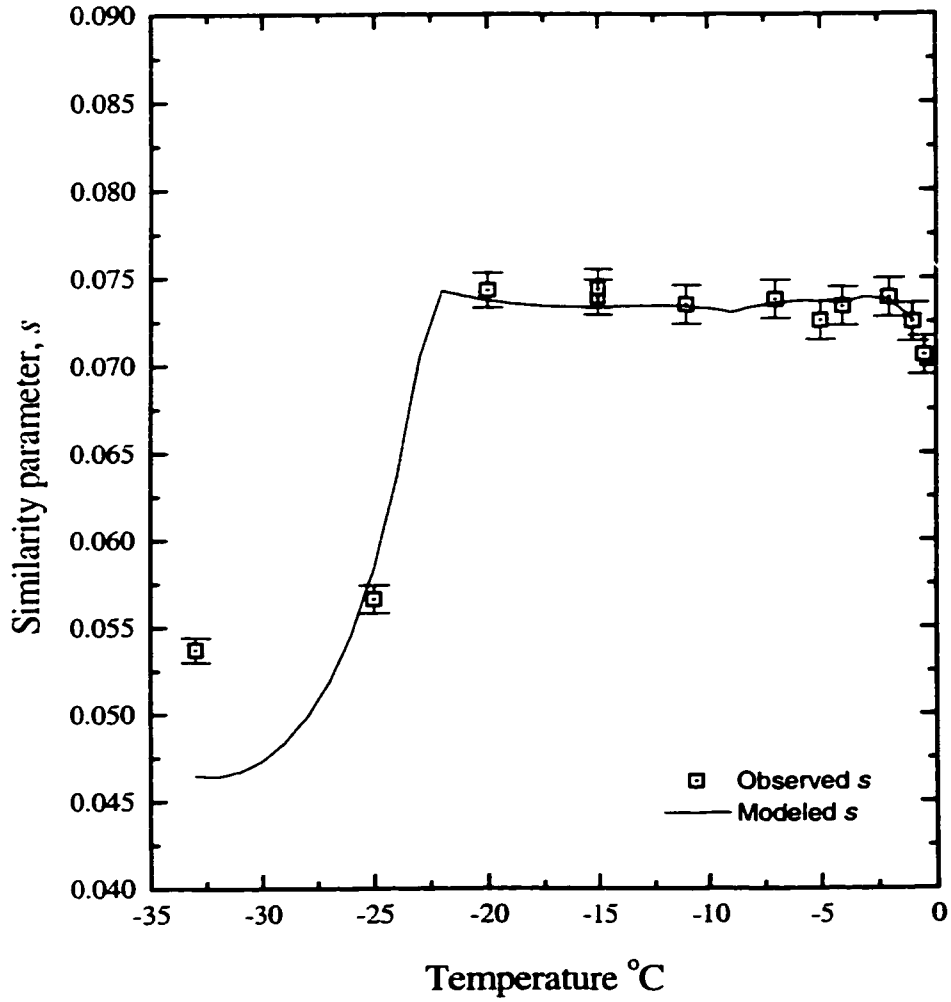

Figure 7.3 Comparison of modeled and observed similarity parameter. The modeled similarity parameter was computed using the refined structural-optical model.

physical processes controlling the optical properties of warm first year ice are missing from the model. Let us now consider three such processes.

Anisotropy of Congelation Ice

Our observations of the structure of first-year congelation sea ice showed that brine tubes and strings of brine pockets are generally aligned vertically. Scattering by straight-walled tubes with perfect vertical alignment should be limited to azimuthal redistribution of the light field when the cylinders are oriented in the same direction as the incident source (T. Grenfell, personal communication, 1999). If this is true, the

apparent optical properties of first-year congelation ice should depend on the orientation of the microstructure. When the microstructure is oriented in the direction of the incident light, the only source of scattering should be the cap-shaped ends of the tubes. This should be the minimum scattering case for tubes. When tubes are oriented perpendicular to the direction of the incident light, there should be considerably more scattering. When the tubes are randomly oriented, they are quite accurately modeled using the equivalent sphere treatment with volume-to-surface-area ratio conserved (Grenfell and Warren, 1999).

Because scattering from brine tubes is a large portion of the total scattering, an experiment was conducted to test the hypothesis that scattering by vertically oriented brine tubes is best modeled by representing only the two endcaps. A cube-shaped sample was constructed that could be oriented with the direction of its structure either parallel or perpendicular to the direction of the incident illumination. The sample was prepared from an adjacent location in the same core as the optical and physical property samples. It was cut and polished with edge length approximately 6 cm. The sample was placed in the optical housing built for the cylindrical sample, then $L_\alpha(30°)$ and $L_t(30°)$ were measured for four different sample orientations. For two of the orientations the brine tubes were oriented in the direction parallel to the incident light (as the ice would appear in situ and upside down). The average backscattered and transmitted relative radiances for this case are denoted by $L_\alpha^{\uparrow}(30°)$ and $L_t^{\uparrow}(30°)$. For the other two orientations the brine tubes were oriented perpendicular to the incident light, and the average radiances denoted by $L_\alpha^{\rightarrow}(30°)$ and $L_t^{\rightarrow}(30°)$. Although the Monte Carlo model cannot be applied to a cube-shaped domain, it was still possible to quantify relative changes in the optical properties as a function of sample orientation.

If the vertically oriented brine tubes are optically identical to a set of randomly oriented tubes, the apparent optical properties should be independent of sample orientation. If the apparent optical properties vary with sample orientation, however, this would suggest that some discount from the full equivalent sphere treatment should be applied when describing ice with aligned structure.

The observations were quantified by computing two indices related to the anisotropy of the apparent optical properties. The index derived from the backscattered radiances was defined as

$$\gamma_\alpha = \frac{L_\alpha^{\uparrow}(30°) - L_\alpha^{\rightarrow}(30°)}{L_\alpha^{\uparrow}(30°) + L_\alpha^{\rightarrow}(30°)}.$$

Similarly, the index derived from the transmitted radiances was defined as

$$\gamma_t = \frac{L_t^{\uparrow}(30°) - L_t^{\rightarrow}(30°)}{L_t^{\uparrow}(30°) + L_t^{\rightarrow}(30°)}.$$

At –15 °C, γ_α was 0.03 and its value increased to 0.05 at –5 °C. γ_t was approximately 0.01 at –15 and –5 °C.

Although we lack a radiative transfer model that can treat anisotropic media, we can use the Monte Carlo model to determine what change in σ would produce the observed γ_α in a cylindrical sample. At –15 °C, the inferred value of s from the observations was 0.0739, with a corresponding value of 0.0211 for $L_\alpha^{\uparrow}(30°)$. The anisotropy ratio γ_α = 0.03 requires that $L_\alpha^{\rightarrow}(30°) = 0.02233$ and s becomes 0.0706. The corresponding scattering coefficient values are $\sigma^{\uparrow} = 0.291$ and $\sigma^{\rightarrow} = 0.319$ mm^{-1}. This 10% change in σ suggests that the effective scattering coefficient for a sample of ice with structure oriented vertically will be 10% less than the effective scattering coefficient for a sample of ice with randomly oriented structure. The corresponding modeled γ_t value was very small in accord with the observations.

A similar analysis carried out at –5 °C with $\gamma_\alpha = 0.05$ indicated a 13% discount in σ from the equivalent sphere treatment. This is in accord with the observations that ice structure becomes more anisotropic at warmer temperatures (as in Fig. 4.9). At cold temperatures, the brine tubes are not perfectly straight and do not have perfect vertical alignment. As the temperature increases, however, small brine pockets merge with and become part of larger brine tubes at the same time that the tube side walls become smoother and generate less scattering. To include these effects in the structural-optical model, we used a σ discount of 10% when $T \leq$ -8 °C, and then increased the discount by 1% per degree above –8 °C.

Temperature-Dependent Asymmetry Parameter

Because theoretical estimation of g for sea ice is difficult at temperatures where precipitated salt crystals are enclosed within brine inclusions, it seemed reasonable to simply use a constant bulk g obtained from the comparison between structural and optical observations. However, in the warm regime, some aspects of the problem of estimating g are simplified. In addition to the shape and size of the scatterer, g is sensitive to the refractive index contrast between the scatterer and its environment. As the ice warms, the ratio of n_b to n_i is dramatically reduced, causing brine inclusion phase functions to become increasingly forward-peaked.

Mie theory predicts that g_b for a 50 μm sphere of brine in ice should be approximately 0.992 at –8 °C and 0.996 at –2 °C. While this appears to be only a small increase, it pushes g very close to 1, and the impact on total scattering is significant. Because $n_b(T)$ is known (Maykut and Light, 1995), $g_b(T)$ can be computed. Values of $g_b(T \geq -8\ °C)$ are considerably larger than the bulk $g = 0.978$ inferred earlier, however. At –8 °C scattering by brine inclusions dominates the total scattering, so we assume that $g \sim g_b$. There is, however, a discrepancy between the inferred bulk g of 0.978 and the Mie theory estimate of approximately 0.992 for g_b. If this discrepancy is accounted for by including scattering from an additional component in the ice, the bulk asymmetry parameter at –8 °C can be written as

$$g(T) = \frac{[g_b(T)\sigma_b + g_R\sigma_R]}{\sigma_b + \sigma_R}, \tag{7.2}$$

where g_R is the asymmetry parameter for the additional scattering component, and σ_R is its scattering coefficient. We assign the subscript R to the additional scattering because it turns out to be simplest to model it as a Rayleigh scatterer, for which $g_R = 0$. This additional scattering could be due to a number of things, including small particulates or microcracks within the ice, or the presence of drained pores along the core boundaries. The plausibility of the existence of this additional scattering component will be discussed in the next chapter.

At –8 °C, the structural-optical model predicts the total scattering coefficient for all brine inclusions to be $\sigma_b = 0.37$ mm^{-1} based on the initialization values given in Table 7.3 and the increased scattering due to inclusion enlargement between –15 and –8 °C. Solving for σ_R when $g = 0.978$, σ_R is estimated to be 0.0055 mm^{-1}. We took $\sigma_R = 0.0055$ mm^{-1} at all temperatures and computed $g_b(T)$ from Mie theory assuming representative brine inclusion sizes and $n_b(T)$. Using Eqn. 7.2 and $g_b(T)$, $g(T)$ was computed for $T \geq$ -8 °C, and the resulting $g(T)$ values are shown in Table 7.4. Asymmetry parameters that increase with temperature show decreased scattering, and thus increased s with warming. While this greatly reduces the total scattering predicted by the structural-optical model at warm temperatures, the effects of changes in the number density of the brine inclusions due to inclusion merging still need to be considered.

Table 7.4. Temperature-dependent bulk asymmetry parameter for warm ice.

Temperature, °C	g
-1	0.990
-2	0.986
-3	0.984
-4	0.983
-5	0.981
-6	0.980
-7	0.978
-8	0.978

Merging Brine Pockets

The observations in Chapter 4 showed that considerable merging of brine pockets occurred as the ice temperature became warm. Because of large differences in inclusion number density, the fraction of pockets that actually merged varied dramatically between scenes. Estimates of the average temperature-dependent merging rate (Section 4.4.3) were used in the structural-optical model and these estimates were subsequently adjusted based on the comparison with observed s values. The resulting estimate of the merging factors expressed as a percentage of N_{bp} at -15 °C is shown in Table 7.5. Brine

pocket and vapor bubble merging was modeled by reducing the number density and appropriately increasing the size of the inclusions. There is no mechanism in the model for treatment of merging brine tubes, or for merged brine pockets to become brine tubes, although both these processes were observed to occur.

Table 7.5. The merging factors expressed as the percentage of brine pockets at –15 °C that remain at each temperature.

Temperature °C	% of brine pockets remaining
-5	100
-4	90
-3	50
-2	20
-1	1

Figure 7.3 shows the final comparison of observed and predicted $s(T)$ computed with new formulations for precipitated salt crystals and the cumulative effects of four physical processes occurring in warm ice: (i) brine inclusion enlarging, (ii) anisotropic structure, (iii) reduced refractive index contrast between brine and ice, and (iv) brine pocket merging. Good agreement is evident at all temperatures above –25 °C.

7.5 Discussion

Microstructure observations in Chapter 4 suggest that precipitating hydrohalite crystals usually become enclosed in the ice, rather than suspended in the brine. Because earlier experiments (Maykut and Light, 1995) have shown that hydrohalite tends to nucleate on ice, it appears likely that hydrohalite crystals nucleate along the walls of the brine inclusions. As the temperature is reduced, ice grows around the salt crystals, leaving them encased in ice. Because the salt crystals are encased in ice, it is no longer appropriate to consider how hydrohalite scatters as a single crystal suspended in liquid brine, and we abandoned the representation used by Light (1995). Since the refractive index contrast between hydrohalite and ice is considerably larger than the contrast between hydrohalite and brine, crystals imbedded in the ice are more effective scatterers. We observed that, as the ice cooled, the contrast apparent on the walls of the

inclusions increased progressively. This is at least partly due to the concentrating brine, but may also be due to the precipitation of salts along the inclusion walls.

The sequestering of hydrohalite within the ice also explains another optical observation in the hydrohalite regime. When hydrohalite is removed from the liquid in the inclusion, the seawater-ice system becomes fractionated. At temperatures below –23 °C two separate environments with separate freezing equilibria exist. Brine inclusions retain all of the salts from the original sea water, but become depleted in Na^+ and Cl^- as these ions precipitate. At the location of the sequestered hydrohalite, the binary NaCl-H_2O system occurs. In this binary system, only hydrohalite and ice exist below the eutectic at –21.2 °C, with no liquid. This fractionation can cause hysteresis. The hydrohalite will not precipitate in the brine inclusion until the brine is cooled to –22.9 °C, but upon warming it will not dissolve until the hydrohalite crystals trapped in the ice reach –21.2 °C, at which temperature they should dissolve entirely.

The optical observation at –21 °C was taken as the ice was warmed from –33 °C. Care was taken to ensure that enough time had elapsed between changes in temperature that the precipitated salts had come to equilibrium (in this case, 72 hours). Since the temperature cycle on the laboratory thermostat had ± 1 °C amplitude, the sample was frequently cooled to temperatures as cold as –22 °C during the period. Optical data taken at –21°C (Fig. 6.10) indicate that hydrohalite was still present. However, the structural-optical model assumes that all temperature-dependent changes are fully reversible, and at –21 °C predicts that all the hydrohalite has dissolved. For these reasons, the observation of s at –21 °C is not shown figures comparing observed optical properties with those computed by the model.

Throughout the mirabilite regime, it was observed that the total scattering remained nearly constant. Two factors contribute to an increase in scattering as the temperature increases through this regime and two other factors contribute to a corresponding decrease in scattering. As brine inclusions enlarge, σ_b increases. Also, as the brine warms and becomes more dilute, its refractive index decreases, promoting greater index contrast between mirabilite crystals and their brine environment. This means that as the ice warms, individual mirabilite crystals produce more backscattering. The same

physical change in brine refractive index causes brine inclusions to become more forward scattering. In addition, as the temperature warms, mirabilite crystals begin to dissolve, reducing σ_s. The optical observations suggest that the net result of these four processes is a nearly temperature-independent s in the mirabilite regime. The structural-optical model was used to quantify the compensating effects in σ_b and σ_s, but unfortunately, we were not able to predict g for brine inclusions containing precipitated salt crystals, so it is difficult to assess the net effects of changes in g_b and g_s.

It is also of interest to quantify the relative importance of the four processes which appear to govern scattering at warm temperatures. While enlarging brine inclusions cause scattering to increase as the temperature increases, brine pocket merging, increasing structural anisotropy, and increasing g_b cause the total scattering to decrease as the temperature increases. The relative effects of these four processes on $s(T)$ are shown in Fig.7.4, both individually and collectively. The curves describing the effects of structural anisotropy and brine pocket merging depart little from the curve describing the effect of inclusion enlarging. Thus, anisotropy and merging have relatively small effects on scattering at warm temperatures. In contrast, the effect of increasing g_b shows a substantial departure from the enlarging curve and clearly has the largest effect on scattering.

The inferred g is equal to 0.978 at temperatures below –8 °C, and increases to 0.990 as temperature approaches the melting point. At all temperatures, the inferred g is larger than the minimum g specified by the comparison of observed and modeled apparent optical properties. The inferred value of g is also considerably smaller than g values predicted when results of Mie theory are used to estimate a σ-weighted bulk value of g. There are several reasons why the bulk g should be less than that predicted by Mie theory. While Mie theory applies to spherical inclusions, very few of the inclusions in sea ice are spherical, especially precipitated salt crystals. Inclusions with sharp edges, parallel faces, and irregular shapes can have considerably lower g values than their corresponding equivalent spheres (Muinonen et al., 1989). Additionally, inclusions in sea ice tend to be compound, particularly at cold temperatures where salt

crystals precipitate within brine inclusions. Assigning an effective g to the single scattering associated with such a compound inclusion is a difficult task.

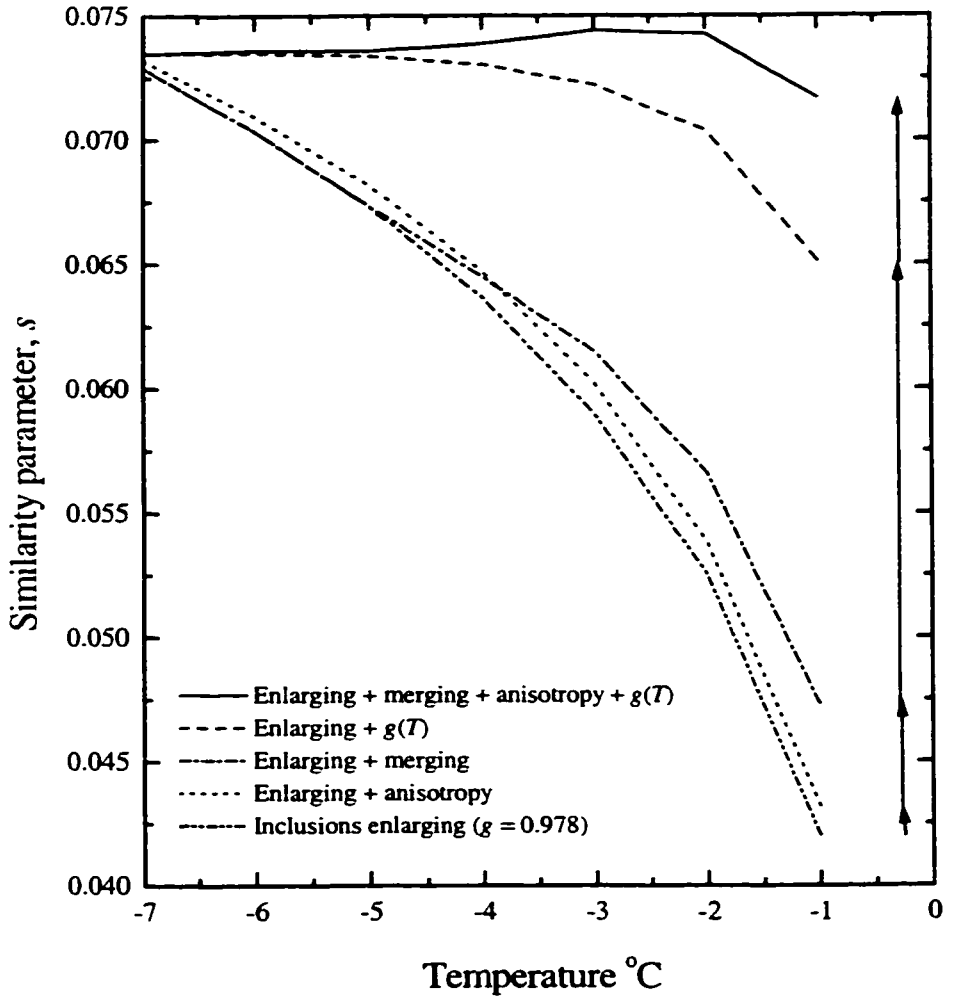

Figure 7.4 Comparison of similarity parameters for the four processes identified to affect total scattering in warm sea ice. Arrows in margin show direction and magnitude of incremental improvement as anisotropy, merging, and g(T) are added to the model.

CHAPTER EIGHT
SENSITIVITY STUDIES AND CONCLUSIONS

The previous chapters have described the acquisition and analysis of data needed for the development and testing of a structural-optical model for first-year ice. In this chapter, we examine the sensitivities of this model and its applicability to other types of sea ice.

8.1 First-Year Interior Ice

The model was developed from observations of the structural and optical properties of first-year interior ice with 4.7 $^{o}/_{oo}$ salinity. The inherent optical properties predicted by the model for this ice are summarized in Table 8.1. Scattering coefficients for brine pockets (σ_{bp}), brine tubes (σ_{bt}), precipitated salts (σ_s), gas bubbles (σ_g), and an additional Rayleigh scatterer (σ_R) are given, along with the asymmetry and similarity parameters for ice temperatures between –33 and –1 °C. This set of IOPs will be referred to as the "standard case". The processes used to determine IOPs at temperatures below –8 °C are considered reversible, whereas, the processes used to determine IOPs at temperatures above –8 °C are based on observations of the ice as it warmed, and are not generally applicable to ice as it cools.

At temperatures above –22.9 °C, brine tubes were responsible for more scattering than any other constituent. Scattering coefficients for brine pockets and mirabilite crystals were smaller, but critical to predicting the temperature-dependent changes in the optical properties. The scattering coefficient for vapor bubbles was found to be very small at all temperatures but, because g for bubbles is 0.86, the total scattering by vapor bubbles cannot be ignored for temperatures above –22.9 ° C. As expected, scattering at temperatures below –22.9 °C was dominated by hydrohalite crystals. These results are based on specific distributions of brine, vapor, and salts observed in a particular sample of ice. In this section, we examine how changes in these distributions would be likely to affect the optical properties of first-year ice.

Table 8.1. Temperature-dependent inherent optical properties of first-year interior sea ice with 4.7 $^{o}/_{oo}$ salinity.

Temperature (°C)	σ_{bt} (mm^{-1})	σ_{bp} (mm^{-1})	σ_s (mm^{-1})	σ_g (mm^{-1})	σ_R (mm^{-1})	σ_{total} (mm^{-1})	g	s
-1	0.789	0.079	0	0.0016	0.0055	0.874	0.990	0.0726
-2	0.525	1.026	0	0.0031	0.0055	0.659	0.987	0.0737
-3	0.427	1.030	0	0.0035	0.0055	0.566	0.985	0.0739
-4	0.374	1.031	0	0.0040	0.0055	0.514	0.983	0.0736
-5	0.340	1.018	0	0.0039	0.0055	0.467	0.981	0.0737
-6	0.316	1.006	0	0.0038	0.0055	0.431	0.980	0.0737
-7	0.299	0.097	0	0.0037	0.0055	0.405	0.978	0.0736
-8	0.285	0.090	0	0.0036	0.0055	0.385	0.977	0.0734
-9	0.272	0.085	0.041	0.0036	0.0055	0.407	0.978	0.0730
-10	0.260	0.080	0.054	0.0036	0.0055	0.404	0.978	0.0733
-11	0.251	0.076	0.066	0.0036	0.0055	0.403	0.978	0.0734
-12	0.243	0.073	0.077	0.0036	0.0055	0.402	0.978	0.0734
-13	0.236	0.070	0.088	0.0036	0.0055	0.402	0.978	0.0734
-14	0.229	0.068	0.097	0.0036	0.0055	0.403	0.978	0.0734
-15	0.224	0.066	0.105	0.0036	0.0055	0.403	0.978	0.0734
-16	0.218	0.064	0.112	0.0036	0.0055	0.403	0.978	0.0733
-17	0.214	0.062	0.118	0.0037	0.0055	0.403	0.978	0.0734
-18	0.210	0.060	0.123	0.0037	0.0055	0.402	0.978	0.0734
-19	0.206	0.059	0.127	0.0037	0.0055	0.401	0.978	0.0735
-20	0.202	0.057	0.131	0.0037	0.0055	0.399	0.978	0.0737
-21	0.198	0.056	0.133	0.0038	0.0055	0.397	0.978	0.0740
-22	0.195	0.055	0.134	0.0038	0.0055	0.393	0.978	0.0743
-23	0.187	0.052	0.188	0.0038	0.0055	0.437	0.978	0.0705
-24	0.162	0.043	0.322	0.0037	0.0055	0.537	0.978	0.0636
-25	0.144	0.037	0.446	0.0037	0.0055	0.637	0.978	0.0584
-26	0.131	0.033	0.556	0.0037	0.0055	0.729	0.978	0.0546
-27	0.121	0.029	0.650	0.0037	0.0055	0.809	0.978	0.0518
-28	0.113	0.027	0.728	0.0037	0.0055	0.877	0.978	0.0498
-29	0.107	0.025	0.790	0.0038	0.0055	0.932	0.978	0.0483
-30	0.103	0.024	0.836	0.0038	0.0055	0.972	0.978	0.0473
-31	0.100	0.023	0.867	0.0038	0.0055	0.998	0.978	0.0467
-32	0.098	0.022	0.881	0.0039	0.0055	1.010	0.978	0.0464
-33	0.097	0.022	0.880	0.0039	0.0055	1.008	0.978	0.0465

8.1.1 Brine Inclusions

Total brine volume in the model was divided between tubes and pockets in accord with the structural observations, 7% being assigned to pockets, and 93% to tubes. Tests were conducted to determine the sensitivity of the model to the brine distribution within

the ice. In the first test, the ice salinity was held constant at 4.7 $^{o}/_{oo}$ and the entire brine volume was allocated to brine tubes. The brine tube size distribution was held constant and the number density increased from 0.56 to 0.61 per mm^3 to account for brine that was in the brine pockets. For this structure, σ_b was reduced from 0.290 mm^{-1} to 0.241 mm^{-1} at –15 °C, a decrease of about 17%. To match the observed optical properties of the standard case, g would have to be reduced from 0.978 to 0.975. This lower g value accounts for scattering lost when the brine pockets are removed.

If, instead, the entire brine volume were allocated only to brine pockets, the number density would have to be increased to 450 per mm^3 to match the standard case, assuming the brine pocket size distribution of the standard case. This would cause the scattering coefficient for the brine to increase from 0.290 mm^{-1} to 0.901 mm^{-1} at –15 °C. To compensate for this increased scattering, g would have to be increased from 0.978 to 0.992. As might be expected, this many brine pockets generate a $\sigma(T)$ that varies more strongly with temperature than is supported by the optical observations. While 450 pockets per mm^3 with the observed size distribution appears to be an unrealistic brine pocket number density, it should be noted that higher resolution microimagery has revealed the presence of an additional 100 – 200 small brine inclusions per mm^3 beyond what were seen in our laboratory observations (H. Eicken, personal communication, 2000). This preliminary estimate was made in first-year sea ice samples also extracted near Point Barrow, Alaska. Because these inclusions have dimensions less than 10 μm, their scattering cross-section is small. We estimate that a population with r_{sp} = 3 μm and N_{sp} = 150 per mm^3 would increase σ_b by approximately 0.008 mm^{-1}, less than 3% of σ for all other brine inclusions. Furthermore, despite their small size, g for these inclusions is still quite large due to the small refractive index contrast between the brine and the ice. Because the effect of this additional scattering is small, it is not presently included in the model.

8.1.2 Precipitated Salt Crystals

Because the structural data contained little information about the size distributions of precipitated salt crystals, effective crystal sizes were inferred from comparisons with

the optical data. To parameterize scattering by salt crystals, the model was used to compute the total mass and number as a function of temperature and salinity assuming that crystal size remained constant with temperature. We would, however, like to know how changes in the assumed crystal size affect the optical properties of the ice. Figure 8.1 shows calculated albedo and transmissivity for a 5-cm-thick slab of 4.7 $^{o}/_{oo}$ ice as a function of temperature and salt crystal size. The albedo and transmissivity at 500 nm were computed using a 4-stream plane-parallel radiative transfer model (Grenfell, 1991). Smaller crystals increase the number density and therefore the total scattering, increasing the albedo and decreasing the transmissivity. Larger crystals have the opposite effect. In the mirabilite regime, the larger value of σ_s predicted with small crystals produces a $\sigma(T)$ that increases with decreasing temperature. When crystals as small as these are used, $\sigma(T)$ is determined primarily by $\sigma_s(T)$ and the rate which total scattering changes as a function of temperature appears contrary to the optical observations, where scattering was observed to be approximately constant with temperature. Likewise, large crystals do not produce enough scattering to offset the temperature-dependent changes in σ_b, and $\sigma_b(T)$ dominates $\sigma(T)$. The choice of effective mirabilite crystal size of 10 μm in the model predicts not only the observed magnitude of scattering, but also the observed temperature dependence of scattering.

8.1.3 Additional Scatterers

In Chapter 7 it was found that the presence of an additional scatterer was needed to explain the difference between g inferred from the comparison with data and g predicted from Mie theory. It was assumed that this additional scatterer had $g_R = 0.0$, and $\sigma_R = 0.0055$ mm^{-1} at all temperatures. No additional scatterers were observed in the ice microstructure, consistent with the notion that the features responsible for the additional scattering were small (< 10 μm). It is possible that the presence of additional small brine inclusions or small particulates (e.g., detrital, lithogenic, or biogenic material) in the ice contribute to this scattering. It is also possible that roughened side walls on the optical sample could lead to overestimates of the inferred σ values. This could be particularly problematic if inclusions near the boundaries of the cylindrical

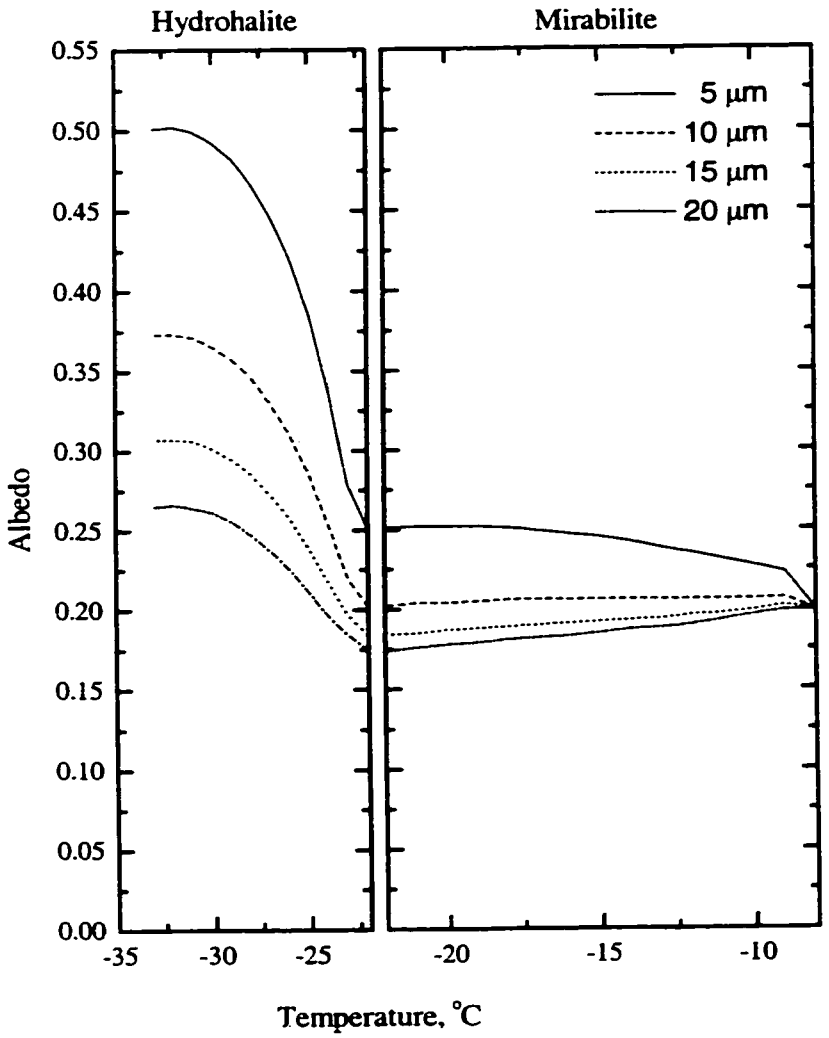

Figure 8.1 Calculated (a) albedo and (b) transmissivity at 500 nm for a 5-cm-thick, 4.7°/$_{oo}$ slab as a function of temperature and precipitated salt crystal size. The mirabilite crystal size was set to the size of the hydrohalite for temperatures below –22 °C.

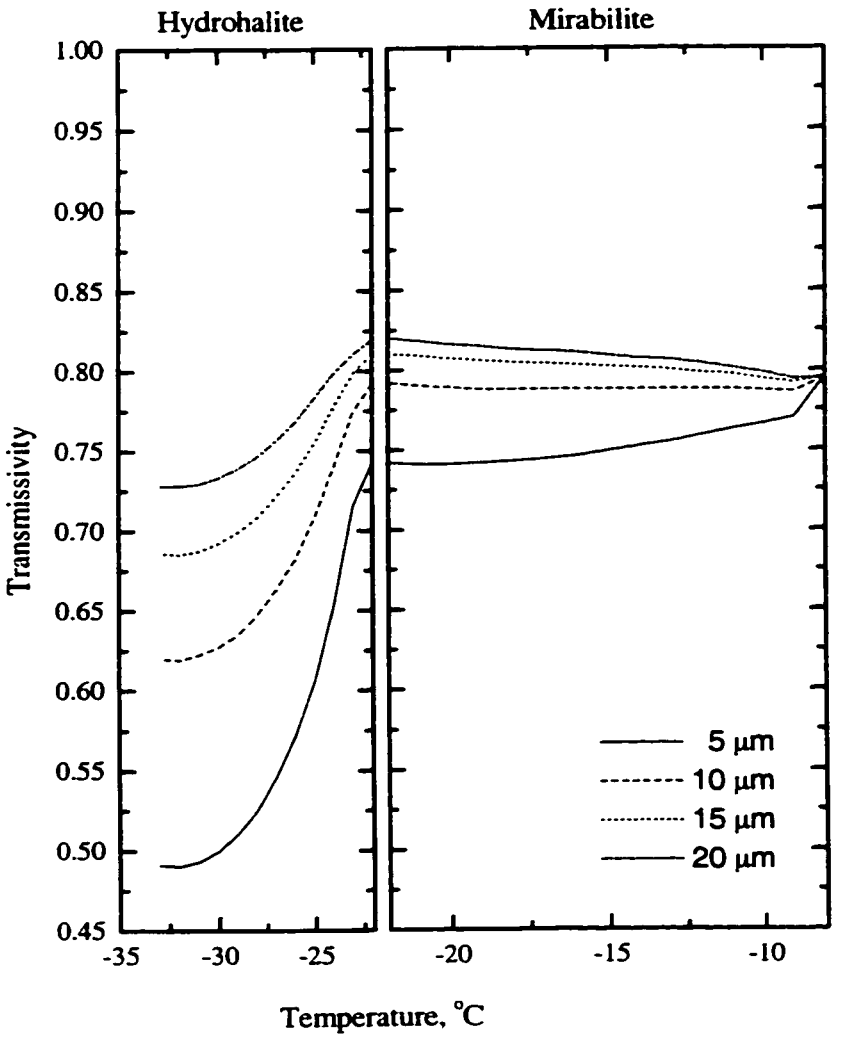

Figure 8.1 continued

cores drained when the samples were extracted. Such drained inclusions could cause enhanced scattering when brine pockets convert to gas bubbles. Structural aberrations such as these would have been difficult to quantify or even detect in the thin section observations. To investigate the effect of a roughened sample side wall, an experiment was performed on an optical sample where the side walls were roughened with coarse sandpaper. For this case, the inferred optical properties showed enhanced volume scattering. Because the Monte Carlo model was only able to simulate a sample with horizontally homogeneous structure and perfectly smooth side walls, this complication remains difficult to correct.

It is, however, quite likely that at least some of the additional scattering observed in our laboratory samples was generated by extensive microcracking within the ice. Such cracks would form as the ice cooled and would serve as reservoirs of brine, supplying brine pockets with liquid. While such cracks can be expected to form naturally in sea ice, subjecting the samples to dry ice temperatures for shipment to the laboratory may have enhanced the degree of microcracking. The microstructural observations did not have sufficient resolution to reveal whether such microcracks existed, but it is likely that any sample of ice that has been cooled sufficiently will develop such cracks. As the sample cools, large pressures build up within shrinking brine inclusions and the internal brine pressure can lead to nucleation of cracks emanating from the brine pocket walls (Picu et al., 1994). The presence of such cracks may also explain the conspicuous absence of vapor bubble formation within enlarging brine pockets. If brine inclusions are interconnected by small cracks, then we would not necessarily expect vapor bubbles to form inside brine inclusions as the ice warmed. Once a crack fills with brine, it is unlikely the crack will heal when cooled. If these microcracks are present, they should scatter light, and we suggest treating them as Rayleigh scatterers as their effective size may be on the order of optical wavelengths.

8.1.4 Asymmetry Parameter

To explain the observed optical properties of the laboratory sample, it was necessary that $g \geq 0.97$. Furthermore, good agreement with observations was obtained when

$T < -8$ °C assuming $g = 0.978$, constant with temperature. However, when $T >$ −8 °C, g must increase significantly in response to decreases in n_b. This increase in g offsets the large increases that occur in σ_b as brine inclusions enlarge. Because brine contained within sea ice is always near freezing equilibrium, the brine salinity and refractive index are strictly determined by the ice temperature. In light of this, $g_b(T)$ is independent of ice microstructure, bulk salinity, age, or history provided the brine inclusions are not small enough to become Rayleigh scatterers.

The influence of $n_b(T)$ on g extends throughout the precipitated salt regimes, as well. In fact, n_b matches n for mirabilite at approximately −29 °C, meaning that g_s approaches 1 at this temperature. Nevertheless, for simplicity, a constant g was still used in the model at temperatures below −8 °C. Had we included the effects of $n_b(T)$ on g at lower temperatures, it would have been necessary to develop an explicit parameterization for g for compound inclusions.

8.2 High Salinity Ice

Results from the natural ice sample were next compared to optical data from laboratory-grown, high salinity ice obtained during a previous experiment (Light, 1995). Optical measurements were made using techniques similar to those described in Chapter 6, except that the cylindrical sample was wrapped in reflective Mylar and the results were interpreted using a plane-parallel radiative transfer model, rather than the Monte Carlo model. The $s(T)$ resulting from the analysis of these data is shown in Fig. 8.2 along with modeled and observed $s(T)$ for the standard case. Because the sample had average salinity of 15 $^{o}/_{oo}$, total scattering should be significantly larger (and s smaller) than the standard case at all temperatures and, indeed, these data show such an increase.

Lacking microstructural observations of the high salinity ice, we can only speculate how the brine was distributed between pockets and tubes. Ice with higher salinity generally results from faster growth which should produce larger (and possibly more numerous) inclusions. To simulate this case, the number density of brine pockets was assumed to be the same as the standard case, but the brine pocket sizes were enhanced

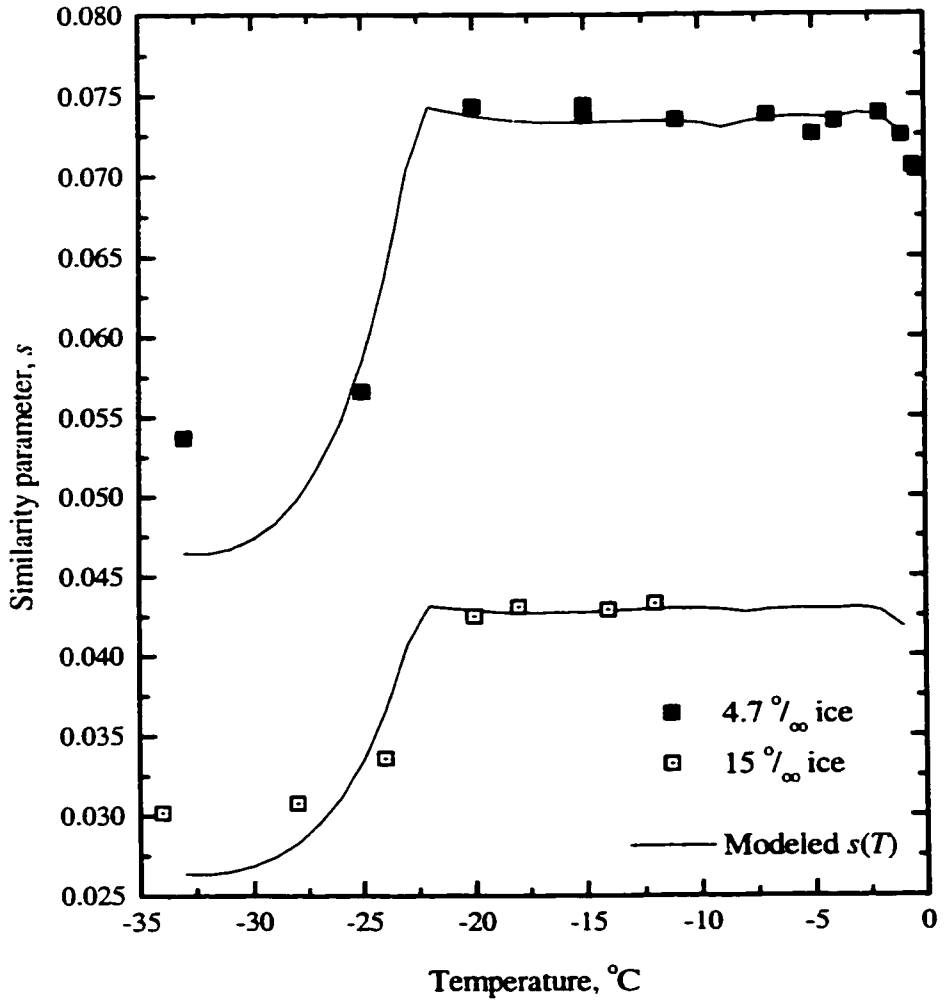

Figure 8.2 Comparison of observed and modeled inherent optical properties for the 4.7 °/∞ sample and a 15 °/∞ laboratory-grown sea ice.

by a factor of 1.5. The remainder of the brine volume was accounted for with 1.7 brine tubes per mm^3. The same g (0.978) as in the standard case was used at all temperatures. There is no reason to expect the salt crystals to be any larger or smaller, just more numerous, so effective crystal sizes were assumed to remain at 10 μm. As in the standard case, scattering by an additional scatterer was needed to explain the discrepancy between the observations and Mie theory, so Eqn. 7.2 was evaluated at T = -8 °C, and the necessary value of σ_R was found to be 0.017 mm^{-1}. σ_R was ~1% of the total value of σ at T = -15 °C, as it was in the standard case. As shown in Fig. 8.2,

good agreement was obtained between the modeled and observed values of $s(T)$ for this high salinity case.

In the hydrohalite regime, the comparison between observed and modeled IOPs is similar to that of the standard case. The model predicts the observed scattering at $T \sim$ -25 °C, but at lower temperatures, the predicted scattering is larger than that observed. Because both cases show a similar overestimate, this suggests that the discrepancy between observed scattering in the hydrohalite regime and our parameterization may be fundamental to the precipitation pattern of hydrohalite crystals. Given that approximately the same discrepancy occurs in both cases, it is not likely to depend on details of the ice structure or the total mass of precipitated salt. In Chapter 7 it was hypothesized that this discrepancy might be due to an increasing effective crystal size.

In the mirabilite regime, the observed and predicted apparent optical properties are approximately constant with temperature, as in the standard case. To match the observed optical properties of the high salinity sample, it was not necessary to adjust the size of the mirabilite crystals. This suggests that the compensating effects of the changes in scattering by brine inclusions and mirabilite crystals are inherent and independent of ice salinity, despite the fact that the magnitude of the scattering is strictly tied to the ice salinity.

Temperature-dependent scattering coefficients predicted with the structural-optical model are shown in Fig. 8.3 for ice samples with salinities of 4.7 and 15 ‰. Both σ curves have been normalized to unity at –33 °C. By normalizing these curves at –33 °C, the differences that depend on ice salinity are removed and the differences that depend on ice structure are retained. At –33 °C, the two values of σ are related by their respective salinities since hydrohalite crystal size was chosen to be constant. Once the difference in magnitude due to the ~3-fold increase in salinity is removed, it can be seen that the temperature-dependence for the two curves is remarkably similar. The small discrepancies are due to differences in how brine is distributed between pockets and tubes for the two cases. As the ice is cooled through the hydrohalite regime, σ increases as the total number of salt crystals increases. This increase in the crystal number

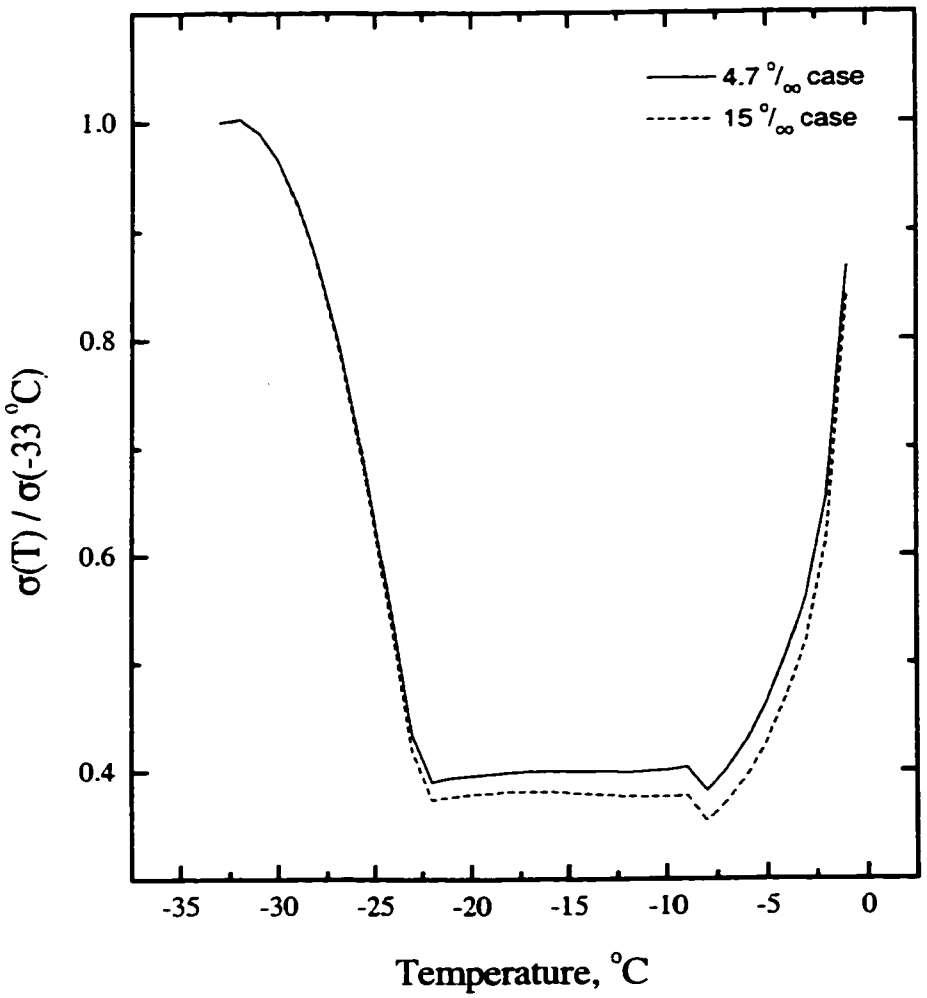

Figure 8.3 Temperature-dependent scattering coefficient for sea ice samples with salinities of 4.7 °/∞ and 15 °/∞. The curves have been normalized to unity at –33 °C.

dominates other physical changes in the ice, such as shrinking brine inclusions and vapor bubbles. In the mirabilite regime, changes in total σ are very small despite large changes taking place in the brine inclusions and mirabilite crystals. The constancy of $\sigma(T)$ suggests that they are approximately equal and opposite, compensating one another, independent of salinity. In the warm ice regime, substantial structural changes are reflected in the large and rapid increase in σ as temperatures increase above –5 °C.

These estimates of $\sigma(T)$ are quantitative representations of observed and inferred changes in microstructure. The magnitude of $\sigma(T)$ is determined by the ice salinity, while the temperature response is determined by changes in the distributions of brine, vapor, and precipitated salt. Changes in n_b may strongly affect the optical properties of

sea ice, but have no bearing on $\sigma(T)$. Because of this, it is possible for changes in the structure of the ice to be large even though changes in the apparent optical properties of the ice remain small. We believe we have captured the main features of temperature-dependent scattering in first-year sea ice, and that this model should be applicable to most types of sea ice. We speculate that ice with large fractional gas volume may actually exhibit different temperature-dependent optical properties as scattering by bubbles becomes important. Bubbles that increase in size with ice temperature will produce a σ_g that depends strongly on temperature, whereas g for bubbles will remain approximately constant, unlike g_b.

8.3 Field Data

Several other investigators carried out in situ optical measurements at the location where our samples were extracted (see Perovich et al., 1998a). Measurements of the spectral extinction of downwelling irradiance (K_λ) within a bore-hole in the ice interior indicate that $K_{500\,nm}$ values ranged between 0.1 and 0.7 m^{-1} for depths between 0.5 and 1.0 m (Perovich et al., 1998a). Earlier field measurements suggested that typical $K_{500\,nm}$ values for first-year interior ice range from 0.9 to 1.2 m^{-1} (Grenfell and Maykut, 1977). In order to compare these observations with our standard case IOPs at –5 °C ($\sigma = 0.467$ mm^{-1}, $g = 0.981$), we used a 4-stream plane-parallel radiative transfer model (Grenfell, 1991) to compute irradiances at several levels within a 1.5-m-thick uniform slab. For five 0.1-m-thick layers between 0.5 and 1.0 m depth, our computations gave $K_{500\,nm}$ values that ranged from 1.3 to 1.6 m^{-1}. These calculated extinction coefficients are somewhat larger than those observed in the two field studies mentioned. For comparison, the corresponding $K_{500\,nm}$ value for the high salinity case IOPs is considerably higher, at 2.0 m^{-1}. This larger $K_{500\,nm}$ value corresponds to what Grenfell and Maykut (1977) classified as transition zone ice, and seems appropriate if the high salinity sample is representative of newly formed lead ice.

IOPs from the standard case were also compared with estimates inferred from horizontally propagating beamspread data taken during the same field campaign near Point Barrow. Mobley et al. (1998) inferred $\sigma = 0.20$ mm^{-1} and $g = 0.98$ for the interior

of the ice. These values correspond to $s = 0.109$, also considerably less scattering than observed in the laboratory samples. However, no information was provided on the sensitivity of inferred optical properties to variations in the actual beamspread observations, so it is difficult to discern how precisely these IOPs were estimated.

It is possible that the values reported by Perovich et al. (1998a) are low since measurements made within bore-holes are prone to light leakage, and resulting K values can be underestimated. Additionally, the measurements reported by Grenfell and Maykut (1977) were estimated for an internal layer within natural ice (12 - 50 cm depth), although a surface scattering layer (~ 10 cm thick) was present above this layer. To some extent, the estimated K values for an internal layer are influenced by the properties of the surface ice. On the other hand, it is possible that additonal scattering may have been induced in the laboratory samples through extensive microcracking.

8.4 Conclusions

This work has helped to clarify the relationship between the physical and optical properties of sea ice. In particular, the effect of temperature on the fundamental optical properties of first-year ice has been observed and modeled. We have demonstrated the utility of being able to simultaneously observe the structural and optical properties of sea ice, as well as the feasibility of obtaining such data on natural sea ice samples in a laboratory setting. Of particular value was the ability to observe structural and optical responses to controlled temperature changes. The Monte Carlo radiative transfer model facilitated the direct comparison of structural and optical data which has lead to new conceptual views of sea ice microstructure.

Structural observations showed that precipitated hydrohalite was rarely visible in brine inclusions at temperatures below –23 °C, yet the optical data indicated a strong response to the onset of hydrohalite precipitation. It appears that the usual picture of a brine pocket with hydrohalite distributed uniformly throughout the inclusion is not realistic. Rather, the new model prescribes that precipitating hydrohalite becomes incorporated into the ice. Contrary to expectations, the structural data showed a conspicuous absence of new vapor bubbles as the ice warmed. Brine inclusions

increased greatly in size, yet no vapor bubbles were observed to form. Through this observation and comparison with the optical data, we conclude that the ice contained extensive microcracks.

Our analysis indicates that the temperature-dependent, total scattering coefficient provides a quantitative description of the overall ice microstructure. $\sigma(T)$ is a useful indicator of changes in microstructure since it is sensitive to changes in number and size distribution for brine inclusions, vapor bubbles, and precipitated salts, and is also sensitive to the vertical alignment of the microstructure. As expected, the apparent optical properties of the ice underwent dramatic changes in response to changes in temperature for $T < -23$ °C, but remained surprisingly constant at higher temperatures. This new model includes large net changes in microstructure at both low ($T < -23$ °C) and high ($T > -5$ °C) temperatures, but little net change in-between.

In the hydrohalite regime, precipitated salts govern the scattering and the optical properties are more strongly tied to the ice salinity than to the details of its microstructure. Data from the mirabilite regime show that changes in scattering due to brine inclusions and mirabilite crystals are approximately equal and opposite, and furthermore suggest that this balance may be inherent in sea ice. The warm regime is characterized by dramatic changes in microstructure and small changes in optical properties. Model calculations indicate that the anisotropy of the ice structure, the merging of brine pockets, and enhanced forward-scattering by brine inclusions combine to offset the structural changes. Understanding the interplay between these effects is critical to explaining the apparent lack of temperature dependence in the observed optical properties. While contributions to this offset by the structural anisotropy and brine pocket merging are dependent upon the microstructure, they are predicted to be small. The dominant contributor to this offset is the enhanced forward scattering driven by $n_b(T)$. The effect of $n_b(T)$ on $s(T)$ is to compensate for increases in $\sigma(T)$, regardless of brine distribution or ice type. As the ice warms, its optical properties make a transition from having a strong dependence on the physical properties of the ice and its microstructure towards being dependent on the electrical properties of the brine.

Identifying and understanding such processes is key to modeling structural-optical relationships which determine how radiative transfer and thermodynamics are coupled in sea ice. The results to this point suggest that it will be possible to develop relatively simple parameterizations of radiative transfer in sea ice that will be appropriate for incorporation into large-scale climate models and GCMs. There are, however, other more complex relationships that require additional study.

It is also worth noting that there appear to be differences between optical properties measured in the laboratory and in the field which need to be resolved. We plan to address this issue by using the structural-optical model in the analysis of optical data collected during the SHEBA Project and during upcoming optical experiments in first-year ice near Point Barrow, Alaska.

LIST OF REFERENCES

Adams, C. A., and G. W. Kattawar, Radiative transfer in spherical shell atmospheres 1. Rayleigh scattering, *Icarus 35*, 139-151, 1978.

Alcouffe, R. E., R. S. Baker, F. W. Brinkley, D. R. Marr, R. D. O'Dell, and W. F. Walters, DANTSYS: A diffusion accelerated neutral particle transport code system, *Rep. LA-12969-M*, Los Alamos National Laboratory, Univ. of Calif., Rev. 1997.

Anderson, D. R., D. J. Sweeney, and T. A. Williams, *Introduction to Statistics: An Applications Approach*, 602 pp., West Publishing Company, St. Paul, Minn., 1981.

Arrigo, K. R., C. W. Sullivan, and J. N. Kremer, A bio-optical model of Antarctic sea ice, *J. Geophys. Res., 96*, 10,581-10,592, 1991.

Assur, A., Composition of sea ice and its tensile strength, in *Arctic Sea Ice,* Nat. Acad. Sci., Nat. Res. Council Pub 598, Washington, D. C., 106-118, 1958.

Barkstrom, B. R., and C. W. Querfeld, Concerning the effect of anisotropic scattering and finite depth on the distribution of solar radiation in snow, *J. Glaciol., 14*, 107-124, 1975.

Beyer, W. H., *CRC Standard Mathematical Tables*, 28th ed., CRC Press, Boca Raton, FL, 1987.

Bulgarelli, B., V. B. Kisselev, L. Roberti, Radiative transfer in the atmosphere-ocean system: the finite element method, *Appl. Opt., 38,* 1530-1542, 1999

Case, K. M., Transfer problems and the reciprocity principle, *Rev. Mod. Phys., 29*, 651-663, 1957.

Case, K. M., and P. F. Zweifel, *Linear Transport Theory*, Addison Wesley, Reading, Mass., 1967.

Cashwell, E. D., and C. J. Everett, *A Practical Manual on the Monte Carlo Model for Random Walk Problems*, 153 pp., Pergamon Press, New York, 1959.

Chernigovskiy, N. T., Radiational properties of the central arctic ice coat, 1963, (translated by J. O. Fletcher, B. Keller, and S. M. Olenicoff, eds., Soviet data on the Arctic heat budget and its climatic influence, *RM-5003-PR*, pp. 151-173, The Rand Corporation, Santa Monica, Ca., 1966).

Cole, D. M., and L. H. Shapiro, Observations of brine drainage networks and microstructure of first-year sea ice, *J. Geophys. Res., 103*, 21,739-21,750, 1998.

Collins, D. G., W. G. Blattner, M. B. Wells, and H. G. Horak, Backward Monte Carlo calculations of the polarization characteristics of the radiation emerging from spherical-shell atmospheres, *Appl. Opt., 11*, 2684-2696, 1972.

Cottier, F., H. Eicken, and P. Wadhams, Linkages between salinity and brine channel distribution in young sea ice, *J. Geophys. Res., 104*, 15859-15871, 1999.

Cox, G. F. N., and W. F. Weeks, Equations for determining the gas and brine volumes in sea-ice samples, *J. Glaciol., 29*, 306-316, 1983.

Ebert, E. E., and J. A. Curry, An intermediate one-dimensional thermodynamic sea ice model for investigating ice-atmosphere interactions, *J. Geophys. Res., 98*, 10,085-10,109, 1993.

Eicken, H., Automated image analysis of ice thin sections- instrumentation, methods and extraction of stereological and textural parameters, *J. Glaciol., 39*, 341-352, 1993.

Gavrilo, V. P., and B. Y. Gaitskhoki, The statistics of air inclusions in ice, in *The Physics of Ice*, V. V. Bogorodskii Ed., translated from Russian by the Israel Program for Scientific Translations, pp. 125-128, Jerusalem, 1970.

Golden, K. M., S. F. Ackley, and V. I. Lytle, The percolation phase transition in sea ice, *Science, 282*, 2238-2241, 1998.

Gordon, H. R., Ship perturbation of irradiance measurements at sea. 1: Monte Carlo simulations, *Appl. Opt., 24*, 4172 - 4182, 1985.

Gordon, H. R., and O. Brown, Irradiance reflectivity of a flat ocean as a function of its optical properties, *Appl. Opt., 12*, 1549-1551, 1973.

Grenfell, T. C., A theoretical model of the optical properties of sea ice in the visible and near infrared, *J. Geophys. Res., 88*, 9723-9735, 1983.

Grenfell, T. C., A Radiative transfer model for sea ice with vertical structure variations, *J. Geophys. Res., 96*, 16991-17001, 1991.

Grenfell, T. C., and G. A. Maykut, The optical properties of ice and snow in the Arctic Basin, *J. Glaciol., 18*, 445-463, 1977.

Grenfell, T. C., and D. K. Perovich, Radiation absoption coefficients of polycrystalline ice from 400-1400 nm, *J. Geophys. Res., 86*, 7447-7450, 1981.

Grenfell,T. C., and D. K. Perovich, Spectral albedos of sea ice and incident solar irradiance in the southern Beaufort Sea, *J. Geophys. Res., 89*, 3573-3580, 1984.

Grenfell, T. C., and S. G. Warren, Representation of a nonspherical ice particle by a collection of independent spheres for scattering and absorption of radiation, *J. Geophys. Res., 104*, 31697-31709, 1999.

Hecht, E., *Optics*, 2nd ed., 676 pp., Addison-Wesley Publishing Co., Reading, Ma., 1987.

Henyey, L. G., and J. L. Greenstein, Diffuse radiation in the galaxy, *Astrophys. J., 93*, 70-83, 1941.

Holland, M. M., J. L. Schramm, and J. A. Curry, Thermodynamic feedback processes in a single-column sea-ice-ocean model, *Ann. Glaciol., 25*, 327-332, 1997.

Ingram, W. J., C. A. Wilson, and J. F. B. Mitchell, Modeling climate change: An assessment of sea ice and surface albedo feedbacks, *J. Geophys. Res., 94*, 8609-8622, 1989.

Irvine, W. M., and J. B. Pollack, Infrared optical properties of water and ice spheres, *Icarus, 8*, 324-360, 1968.

Jin, Z., K. Stamnes, W. F. Weeks, and S. C. Tsay, The effect of sea ice on the solar energy budget in the atmosphere-sea ice-ocean system: A model study, *J. Geophys. Res., 99*, 25281-25294, 1994.

King, M. D., L. F. Radke, and P. V. Hobbs, Determination of the spectral absorption of solar radiation by marine stratocumulus clouds from airborne measurements within clouds, *J. Atms. Sci., 47*, 894-907, 1990.

Lake, R. A., and E. L. Lewis, Salt rejection by sea ice during growth, *J. Geophys. Res., 75*, 583-597, 1970.

Langleben, M. P., Albedo and degree of puddling of a melting cover of sea ice, *J. Glaciol., 8*, 407-412, 1969.

Langleben, M. P., Albedo of melting sea ice in the southern Beaufort Sea, *J. Glaciol., 10*, 101-104, 1971.

Light, B., A structural-optical model of cold sea ice, M. S. thesis, Univ. Wash., Seattle, 1995.

Light, B., H. Eicken, G. A. Maykut, and T. C. Grenfell, The effect of included particulates on the spectral albedo of sea ice, *J. Geophys. Res., 103*, 27739-27752, 1998.

Lofgren, G. and W. F. Weeks, Effect of growth parameters on substructure spacing in NaCl ice crystals, *J. Glaciol. 8*, 153-164, 1969.

Lohanick, A. W., and T. C. Grenfell, Variations in brightness temperature over cold first-year sea ice near Tuktoyaktuk, Northwest Territories, *J. Geophys. Res., 91*, 5133-5144, 1986.

Manabe, S., R. J. Stoffer, M. J. Spelman, and K. Bryan, Transient response of a coupled ocean-atmosphere model to gradual changes in atmospheric CO2. Part I: Annual mean response, *J. Climate, 4*, 785-818, 1991.

Maykut, G. A., and T. C. Grenfell, The spectral distribution of light beneath first-year sea ice in the Arctic Ocean, *Limnol. Oceanogr., 20*, 554-563, 1975.

Maykut, G. A., and B. Light, Refractive-index measurements in freezing sea-ice and sodium chloride brines, *Appl. Opt. 34*, 950-961, 1995.

Maykut, G. A., and N. Untersteiner, Some results from a time-dependent, thermodynamic model of sea ice, *J. Geophys. Res., 76*, 1550-1575, 1971.

McCormick, N. J., and G. E. Rinaldi, Seawater optical property estimation from *in situ* irradiance measurements, *Appl. Opt., 28*, 2605-2613, 1989.

Mobley, C. D., A numerical model for the computation of radiance distributions in natural waters with wind-roughened surfaces, *Limnol. Oceanogr., 34*, 1473-1483, 1989.

Mobley, C. D., *Light and Water: Radiative Transfer in Natural Waters*, 592 pp., Academic Press, San Diego, 1994.

Mobley, C. D., Monte Carlo simulation of a point light source in an infinite medium, *Tech. Rep. SRI Project 7311*, SRI Int., Menlo Park, Ca., 1996.

Mobley, C. D., G. F. Cota, T. C. Grenfell, R. A. Maffione, W. S. Pegau, and D. K. Perovich, Modeling light propagation in sea ice, *IEEE Trans. Geosci. and Rem. Sens., 36*, 1743-1749, 1998.

Morel, A. and B. Gentili, Diffuse reflectance of oceanic waters: its dependence on sun angle as influenced by the molecular scattering contribution, *Appl. Opt., 30*, 4427-4438, 1991.

Moritz, R. E., and D. K. Perovich, *SHEBA: Science Plan*, 60 pp., ARCSS OAII Management Office, Polar Science Center, Univ. Wash., Seattle, 1996.

Muinonen, K., Scattering of light by crystals: A modified Kirchhoff approximation, *Appl. Opt., 28,* 3044-3050, 1989.

Muinonen, K., K. Lumme, J. Peltoniemi, and W. M. Irvine, Light scattering by randomly oriented crystals, *Appl. Opt. 28,* 3051-3060, 1989.

Nakawo, M., and N. K. Sinha, A note on the brine layer spacing of first-year ice, *Atmos. Ocean, 22,* 193-206, 1984.

Nakaya, U., Properties of single crystals of ice, revealed by internal melting, *SIPRE Research Paper 13,* 80 pp., U.S. Army Snow, Ice, and Permafrost Res. Est., Wilmette, Illinois, 1956.

Nelson, K. H., and T. G. Thompson, Deposition of salts from sea water by frigid concentration, *J. Mar. Res., 13,* 166-182, 1954.

Perovich, D. K., The optical properties of young sea ice, M. S. thesis, Univ. Wash., Seattle, 1979.

Perovich, D. K., Theoretical estimates of light reflection and transmission by spatially complex and temporally varying sea ice covers. *J. Geophys. Res., 95,* 9557-9567, 1990.

Perovich, D. K., A theoretical model of ultraviolet light transmission through Antarctic sea ice, *J. Geophys. Res., 98,* 22579-22587, 1993.

Perovich, D. K., Light reflection from sea ice during the onset of melt, *J. Geophys. Res., 99,* 3351-3359, 1994.

Perovich, D. K., and A. J. Gow, A statistal description of the microstructure of young sea ice, *J. Geophys. Res., 96,* 16943-16953, 1991.

Perovich, D. K., and A. J. Gow, A quantitative description of sea ice inclusions, *J. Geophys. Res., 101,* 18327-18243, 1996.

Perovich, D. K., and T. C. Grenfell, A theoretical model of radiative transfer in young sea ice, *J. Glaciol., 28,* 341-346, 1982.

Perovich, D. K., J. Longacre, D. G. Barber, R. A. Maffione, G. F. Cota, C. D. Mobley, A. J. Gow, R. G. Onstott, T. C. Grenfell, W. S. Pegau, M. Landry, and C. S. Roesler, Field observations of the electromagnetic properties of first-year sea ice, *IEEE Trans. Geosci. and Rem. Sens., 36,* 1705-1715, 1998a.

Perovich, D. K., C. S. Roesler, and W. S. Pegau, Variability in Arctic sea ice optical properties, *J. Geophys. Res., 103,* 1193-1208, 1998b.

Picu, R. C., V. Gupta, and H. J. Frost, Crack nucleation mechanism in saline ice, *J. Geophys. Res., 99*, 11,775-11,786, 1994.

Plass, G., and G. Kattawar, Monte-Carlo calculations of radiative transfer in the earth's atmosphere ocean system: I. Flux in the atmosphere and ocean, *J. Phys. Oceanogr., 2*, 139-145, 1972.

Pope, R. M., and E. S. Fry, Absorption spectrum (380 – 700 nm) of pure water. II. Integrating cavity measurements, *Appl. Opt., 36*, 8710-8723, 1997.

Richardson, C., Phase relationships in sea ice as a function of temperature, *J. Glaciol., 17*, 507-519, 1976.

Rind, D., R. Healy, C. Parkinson, and D. Martinson, The role of sea ice in a 2 x CO2 climate model sensitivity. Part I: The total influence of sea ice thickness and extent, *J. Climate, 8*, 449-463, 1995.

Smith, R. C., Optical properties of the Arctic upper water, *Arctic, 26*, 303-313, 1973.

Smith, R. C., and K. S. Baker, Absorption coefficients of the clearest natural waters, *Appl. Opt., 20*, 177-184, 1981.

Sobouti, Y., Chandrasekhar's X-, Y-, and related functions, *Astrophys. Journal, Suppl. 72, VII*, 411-560, 1963.

Trodahl, H. J., R. G. Buckly, and S. Brown, Diffusive transport of light in sea ice, *Appl. Opt., 26*, 3005-3011, 1987.

Trodahl, H. J., R. G. Buckley, and M. Vignaux, Anisotropic light radiance in and under sea ice, *Cold Regions Sci and Tech., 16*, 305-308, 1989.

Untersteiner, N., On the mass and heat budget of arctic sea ice, , *Arch. Meteorol. Geophys. Bioklimatol., A, 12*, 151-182, 1961.

van de Hulst, H. C., *Multiple Light Scattering Tables, Formulas, and Applications,* Vols. 1 and 2, 739 pp., Academic, New York, 1980.

Wakatsuchi, M., and T. Saito, On brine drainage channels of young sea ice, *Ann. Glaciol., 6*, 200-202, 1985.

Weeks, W. F., and S. F. Ackley, The growth, structure and properties of sea ice, *CRREL Monograph 82-1*, Cold Reg. Res. and Eng. Lab., Hanover, N.H., 1982.

Weeks, W. F., and A. Assur, The mechanical properties of sea ice, *CRREL Monograph II-B3*, Cold Reg. Res. and Eng. Lab., Hanover, N.H., 1967.

Weeks, W. F., and W. L. Hamilton, The salinity distribution in young sea ice, *Arctic, 15*, 92-108, 1962.

Wiscombe, W. J., Mie scattering calculations: Advances in technique and fast, vector speed computer codes, *NCAR Tech. Note TN-140 + STR*, Nat. Center Atmos. Res., Boulder, Colo., 1979.

Wyatt, C. L., *Radiometric Calibrations: Theory and Methods*, 200 pp., Academic Press, New York, 1978.

VITA

Bonnie Light was born February 18, 1965 in Los Angeles, California. She became interested in pursuing a career in science while a student at North Hollywood High School in North Hollywood, California. She received a Bachelor of Science from Cornell University in 1986 in the Department of Electrical Engineering. While employed with the United States Naval Research Laboratory in Washington D.C. as an Electronics Engineer she received a Thomas Edison Feilowship and completed her Master of Science in Electrical Engineering at the University of Maryland in 1990. During the autumn of 1990, she joined the Department of Atmospheric Sciences at the University of Washington, and received a Master of Science in 1995. While a doctoral candidate, she spent 4 consecutive months participating in studies of the heat and mass balance of sea ice at Ice Station SHEBA in the Beaufort Sea. Her chief scientific interests include the optical properties of sea ice, radiative transfer in the atmosphere and ocean, and the physics of ice covered seas.